

AD _____

Award Number: DAMD17-00-1-0217

TITLE: Breast Cancer Diagnosis Using Ultrasound and Diffusive
Light

PRINCIPAL INVESTIGATOR: Quing Zhu, Ph.D.

CONTRACTING ORGANIZATION: University of Connecticut
Storrs, Connecticut 06269-1113

REPORT DATE: September 2002

TYPE OF REPORT: Annual

PREPARED FOR: U.S. Army Medical Research and Materiel Command
Fort Detrick, Maryland 21702-5012

DISTRIBUTION STATEMENT: Approved for Public Release;
Distribution Unlimited

The views, opinions and/or findings contained in this report are those of the author(s) and should not be construed as an official Department of the Army position, policy or decision unless so designated by other documentation.

20030319 050

REPORT DOCUMENTATION PAGEForm Approved
OMB No. 074-0188

Public reporting burden for this collection of information is estimated to average 1 hour per response, including the time for reviewing instructions, searching existing data sources, gathering and maintaining the data needed, and completing and reviewing this collection of information. Send comments regarding this burden estimate or any other aspect of this collection of information, including suggestions for reducing this burden to Washington Headquarters Services, Directorate for Information Operations and Reports, 1215 Jefferson Davis Highway, Suite 1204, Arlington, VA 22202-4302, and to the Office of Management and Budget, Paperwork Reduction Project (0704-0188), Washington, DC 20503

1. AGENCY USE ONLY (Leave blank)

2. REPORT DATE

September 2002

3. REPORT TYPE AND DATES COVERED

Annual (15 Aug 01 - 14 Aug 02)

4. TITLE AND SUBTITLE

Breast Cancer Diagnosis Using Ultrasound and
Diffusive Light

5. FUNDING NUMBERS

DAMD17-00-1-0217

6. AUTHOR(S)

Quing Zhu, Ph.D.

7. PERFORMING ORGANIZATION NAME(S) AND ADDRESS(ES)

University of Connecticut
Storrs, Connecticut 06269-1113

E*Mail: qing.zhu@UCONN.EDU

8. PERFORMING ORGANIZATION
REPORT NUMBER

9. SPONSORING / MONITORING AGENCY NAME(S) AND ADDRESS(ES)

U.S. Army Medical Research and Materiel Command
Fort Detrick, Maryland 21702-501210. SPONSORING / MONITORING
AGENCY REPORT NUMBER

11. SUPPLEMENTARY NOTES

Original contains color plates. All DTIC reproductions will be in
black and white.

12a. DISTRIBUTION / AVAILABILITY STATEMENT

Approved for Public Release; Distribution Unlimited

12b. DISTRIBUTION CODE

13. ABSTRACT (Maximum 200 Words)

none provided

14. SUBJECT TERMS

breast cancer, ultrasound, diagnosis

15. NUMBER OF PAGES

98

16. PRICE CODE

17. SECURITY CLASSIFICATION
OF REPORT

Unclassified

18. SECURITY CLASSIFICATION
OF THIS PAGE

Unclassified

19. SECURITY CLASSIFICATION
OF ABSTRACT

Unclassified

20. LIMITATION OF ABSTRACT

Unlimited

Table of Contents

Cover.....	1
SF 298.....	2
Table of Contents.....	3
Introduction.....	4
Body.....	5
Reportable Outcomes.....	8
Key Research Accomplishments.....	9
Conclusions.....	9
References.....	9
Appendices.....	10

Introduction:

Tumor blood volume and micro-vascular density are parameters anatomically and functionally associated with tumor angiogenesis. During the last decade, rigorous modeling of the light propagation in the near infrared region, combined with the advancements of light source and detectors, has improved the diffused light measurements and made possible the application of tomographic techniques for characterizing and imaging tumor angiogenesis [1-6]. If a single wavelength is used, optical absorption related to angiogenesis and other normal blood vessels can be measured. If two or more optical wavelengths are used, both oxy-hemoglobin and deoxy-hemoglobin concentrations can be measured simultaneously. In addition, optical scattering is related to cell activations because scattering is sensitive to any particles that are of the size of the optical wavelength. However, the NIR technique has not been widely used in clinics and the fundamental problem remains the intense light scattering. As a result, diffused light probes a wide region instead of propagating along a straight line. Localization or imaging based on tomographic inverse scattering approaches suffers from low spatial resolution and the inversion problem is, in general, underdetermined and ill-posed.

Currently, ultrasound is routinely used in conjunction with mammography to differentiate simple cysts from solid lesions. When the criteria for a simple cyst are strictly adhered to, the accuracy of ultrasound is 96%-100%. However, the ultrasound appearance of benign and malignant lesions has considerable overlapping features [7-8], which has prompted many radiologists to recommend biopsies on most solid nodules. This results in a large number of biopsies yielding normal or benign breast tissue (currently 70% to 80% of biopsies are normal [9]). In addition, the diagnostic accuracy of ultrasound depends largely on the experience of physicians. The best results reported in the literature on distinguishing benign from malignant solid breast lesions were given by Stavros et al [10]. In this reference, a total of 750 palpable solid breast lesions were studied. Despite the known overlap features in some lesions, ultrasound was able to correctly classify 123 of 125 malignant lesions as intermediate or malignant.

We have introduced the use of optical imaging as an adjunct to ultrasound in differentiating benign from malignant lesions [11]. We have demonstrated that optical contrast between benign and malignant lesions can provide more diagnostic information to further classify the acoustic intermediate group, thereby improving ultrasound specificity and reducing unnecessary biopsies.

We have introduced a novel combined imaging using lesion structure images provided by co-registered ultrasound to improve NIR functional imaging capability in determining optical properties [12]. With the a priori knowledge of lesion location and shape, NIR imaging reconstruction can be localized within specified spatial and temporal regions. As a result, the reconstruction is over-determined because the total number of unknown optical properties is reduced significantly. In addition, the reconstruction is less sensitive to noise because the convergence can be achieved within a small number of iterations. We have conducted a series of experiments to assess the improvement on reconstructed optical absorption coefficients with the a priori target depth [13] and spatial location information [14].

In this DOD ARMY sponsored study, we proposed to achieve the following objectives

- 1) to refine our existing NIR optical imaging system hardware toward high signal-to-noise ratio and fast data acquisition (task 1);
- 2) to implement to imaging software for clinical studies (task 1)
- 3) to optimize the combined probe design through simulation and phantom experiments (task 1);

- 4) to validate the combined imaging in cancer detection and diagnosis through clinical studies (task 2).

We have successfully completed task 1 proposed in the application during the first year [13-14] and have partially completed task 2 by recruiting a total of 24 patients and correlating the NIR optical imaging results with ultrasound findings [15]. The preliminary results are summarized in the body of the report. More patients are being recruited and statistics will be reported shortly.

Body

Under the supports of DOD ARMY, we have completed the combined probe and prototype NIR imager. This imager consists of 12 dual wavelength sources and 8 optical detectors [14], and the sources and detectors are coupled through optical fibers to a hand-held probe shown in Figure 1(a) and the probe dimensions are shown in Figure 1(b). A commercial ultrasound probe (7 MHz linear array) is simultaneously deployed in the middle of the combined probe. Currently, this probe is used at the Cancer Center of University of Connecticut Health Center for the proposed clinical studies. With this combined probe, we have demonstrated the advantage of dual-modality diagnosis [15].

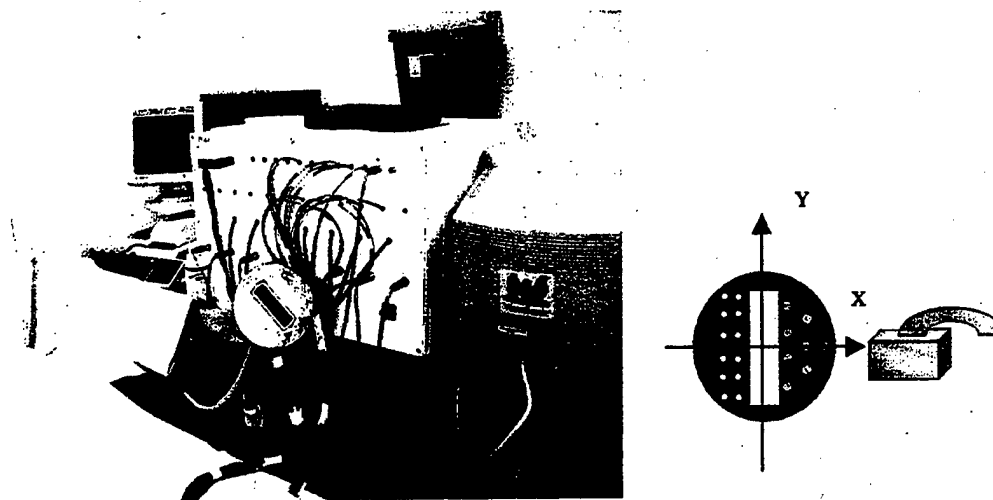


Fig.1. (a) Picture of a hand-held combined probe and a frequency domain NIR imager. (b) Sensor distribution of the combined probe. The diameter of the combined probe is 10 cm. Smaller circles are optical source fibers and big circles are detector fibers. A commercial ultrasound probe is located at the center and its dimensions are 5.6 cm by 1 cm.

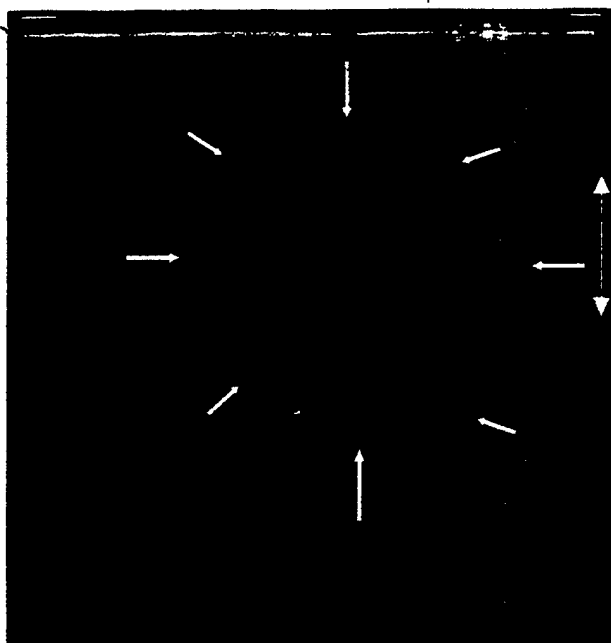
Before the clinical studies, we have fully tested our imaging algorithms with phantom targets which emulate tumor acoustic and optical properties. A new method, moment method, has been invented [16] and tested with phantom targets. However, when we acquired first patient data from several volunteers in November 2001 and used existing algorithms as well as our moment method for optical imaging, we had difficulties in obtaining consistent results for all the cases. We further investigated the imaging algorithms and have successfully invented a two-step imaging reconstruction algorithm reported in Ref. [15]. This algorithm provides consistent

wavelength-dependent optical absorption and hemoglobin concentration of a large breast carcinoma with necrotic core. To the best of our knowledge, such detailed distributions have not been achieved by NIR only imaging reported in the literature.

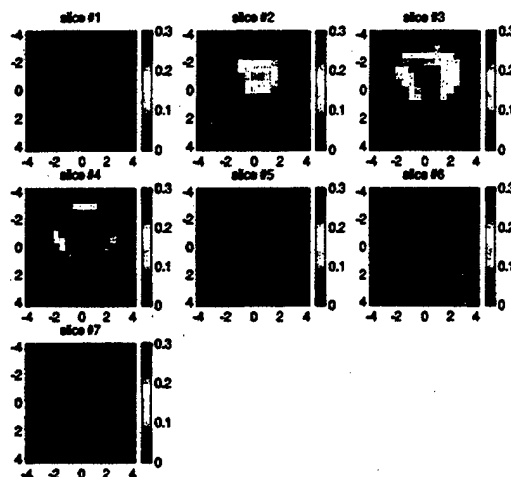
An example from Ref. 15 is given here. Figure 2 (a) shows a gray scale ultrasound image of a palpable lump of a 44-year-old woman. The lesion was located at 6 to 8 o'clock position of the left breast at approximately 1.5 cm depth. Ultrasound showed an irregular poorly defined hypoechoic mass and the lesion was considered as highly suspicious for malignancy. An ultrasound guided core needle biopsy was recommended. Biopsy results revealed that the lesion was a high grade in-situ ductal carcinoma with necrosis.

Multiple optical measurements at two orthogonal positions were simultaneously made with ultrasound images at the lesion location as well as at approximately the same location of the contralateral normal breast. The image reconstruction was performed using the NIR data simultaneously acquired with the ultrasound image shown in Fig.2 (a). The optical image reconstruction revealed optimal lesion centers at approximately (-1.1 cm, 0.3 cm, 1.7 cm) for 780 nm and (-0.9 cm, -0.7 cm, 1.7 cm) for 830 nm, respectively, and optimal diameters of 4.28 cm x 5.18 cm x 1.96 cm. The detailed absorption maps with high absorption non-uniformly distributed around the lesion boundaries at both wavelengths are shown in Fig. 2 (b) and (c). By assuming that the major chromophores are oxygenated (oxyHb) and deoxygenated (deoxyHb) hemoglobin molecules in the wavelength range studied, we can estimate the distribution of total hemoglobin concentration as shown in Fig.2 (d). The extinction coefficients used for calculating oxyHb and deoxyHb concentrations were $\epsilon_{\text{Hb}}^{780} = 2.544$, $\epsilon_{\text{HbO}_2}^{780} = 1.695$, $\epsilon_{\text{Hb}}^{830} = 1.797$, $\epsilon_{\text{HbO}_2}^{830} = 2.419$ in a natural logarithm scale with units of inverse millimoles times inverse centimeters. The measured average cancer and background total hemoglobin concentrations were 116.9 μmoles and 47.6 μmoles , respectively. These values agree with 3-D average measurements reported in the literature.

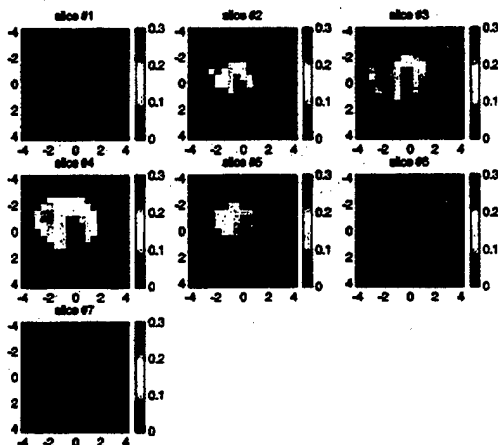
It is interesting to note that the absorption distributions at both wavelengths as well as total hemoglobin concentration were distributed heterogeneously at the cancer periphery. To the best of our knowledge, such fine distributions have not been reported by using NIR only reconstruction techniques. However, this finding agrees with the published literature showing that breast cancers have higher blood volumes than non-malignant tissue due to angiogenesis, especially at the cancer periphery [17]. In addition, the carcinoma reported here had a necrotic core which could lead to low absorptions observed at both wavelengths in the center region. Ideally, pathologic report with blood vessel density count could be used to correlate the NIR findings reported here. Future plans are to obtain microvessel counts in the region of the tumor as well as surrounding, non-malignant breast tissue.



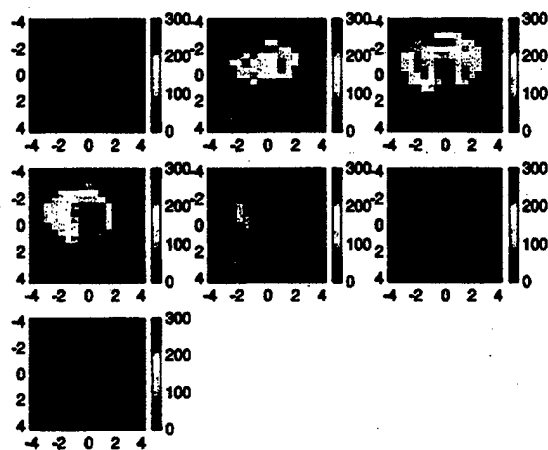
(a)



(b)



(c)



(d)

Fig. 2. (a) A gray scale ultrasound image of a palpable lump of a 44-year-old woman. Ultrasound showed an irregular poorly defined hypoechoic mass and the lesion was considered as highly suspicious for malignancy. Reconstructed optical absorption maps at 780 nm (b) and 830 nm (c). Vertical color bars are absorption coefficient in the unit of cm^{-1} . (d) is the total hemoglobin concentration map. The vertical color bars are μmoles . The NIR data were simultaneously acquired with ultrasound image shown in Fig.2 (a). Each image consists of 7 slices obtained in 0.5 cm spacing from 0.5 cm to 3.5 cm in depth. The vertical and horizontal axes correspond to x and y dimensions of 9 cm by 9 cm.

In summary, we have reported a two-step image reconstruction scheme and we have demonstrated that aided with co-registered ultrasound, detailed optical absorption and total hemoglobin distributions of the breast carcinoma can be obtained. These distributions reveal tumor angiogenesis and provide valuable information for breast cancer diagnosis and treatment.

We have studied a total of 24 patients for the past year and are still recruiting more patients to our study. Patient recruiting is more difficult than we have anticipated. First, we have to study patients who have suspicious lesions seen by mammograms and/or ultrasound. Second, some of the good candidates may not want to participate, particularly cancer patients. We have received one-year extension on this contract and we hope to recruit as many patients as possible in the coming year and to establish statistical significance of our combined imaging method.

Reportable outcomes

Two important issues directly related to combined breast imaging are probe geometry and optical data acquisition system.

Both reflection and transmission geometries have been used by researchers for optical tomography and transmission geometry is more popular than reflection due to dynamic range considerations. In reflection geometry, patients are placed in supine position and the imaging probe consisting of multiple source fibers and detector fibers is placed on top of the breast. Reflected light detected from multiple detector locations is used for image reconstruction. However, the dynamic range of detected signals is very large because lesions could be closer to the skin or deeply seated. We have chosen reflection geometry in our current hand-held probe configuration because conventional ultrasound probes are used in reflection mode. Therefore, our combined probe design compromises both ultrasound tomography and optical tomography. In transmission geometry, patients are in prone position and the examined breast is inserted in a liquid reservoir. Optical source and detector fibers can be distributed around the liquid reservoir. Due to gravity, the breast is much longer in the direction perpendicular to the source-detector plane. As a consequence, the depth of the lesion relative to the source and detector fibers does not change dramatically and the dynamic range of the detected signals is reduced. However, ultrasound probes are not commonly used in transmission geometry due to extra distortion of acoustic wave between the liquid and the breast. We have devoted part of our efforts to optical transmission geometry study in an attempt to find out the best compromise design.

Our results are obtained with 2-dimensional transmission geometry set-up and have showed that similar performance can be expected as long as *a priori* information of lesion locations is used in optical image reconstruction [18].

Regarding optical data acquisition system, frequency domain and DC systems are frequently used by many research groups. The advantage of using frequency domain system is that both amplitude and phase information can be obtained and, therefore, simultaneous reconstruction of absorption and scattering coefficients is feasible. The disadvantage is the complexity in constructing high frequency transmission and reception circuitries, particularly when many parallel channels are needed for fast data acquisition. In addition, the system cost is high. DC systems have advantages of simplicity in circuit construction and low cost. The drawbacks are that the phase information is not available and the cross-talk between the reconstructed absorption

and scattering coefficients may be unavoidable. However, when reconstruction of lesion absorption maps is concerned, frequency domain and DC systems may demonstrate similar performance. We have compared the performance of both systems, in constructing absorption maps under the conditions of NIR reconstruction only and ultrasound guided NIR reconstruction and the results as we expected are reported in [18].

Key Research Accomplishments:

- invented a new optical imaging algorithm which can be used successfully for *in vivo* data
- acquired data from 24 patients with suspicious lesions
- studied combined imaging using transmission geometry in an attempt to find out the best compromise in the imaging probe design.

Conclusions:

We have simultaneously acquired ultrasound and NIR optical data from 24 patients and have showed encouraging results for imaging breast lesion angiogenesis using the combined approach. In addition, we have studied transmission geometry for combined imaging in an attempt to find out the best geometry for using the combined approach.

References:

- [1] B. Tromberg, N. Shah, R. Lanning, A. Cerussi, J. Espinoza, T. Pham, L. Svaasand and J. Butler, "Non-Invasive *in vivo* characterization of breast tumors using photon migration spectroscopy," *Neoplasia* vol.2, No 1:2, pp26-40, 2000.
- [2] Yodh A and Chance B, "Spectroscopy and imaging with diffusing light," *Physics Today*, March 1995.
- [3] S. Fantini, S. Walker, M. Franceschini, M. Kaschke, P. Schlag, and K. Moesta, "Assessment of the size, position, and optical properties of breast tumors *in vivo* by noninvasive optical methods," *App. Optics*, 37: 1982:1989, (1998).
- [4] S. Zhou, Y. Chen, Q. Nioka, X. Li, L. Pfaff, C.M. Cowan, and B. Chance, "A portable dual wavelength amplitude cancellation image system for the determination of human breast tumor," *SPIE Proceedings of Optical Tomography and Spectroscopy of Tissue III*, 3597, 571-579, (1999).
- [5] B. Pogue, S. P. Poplack, T. O. McBride T. O., W. A. Wells, K. S. Osterman, U. Osterberg, and K. D. Paulsen, "Quantitative hemoglobin tomography with diffuse near-infrared spectroscopy: pilot results in the breast," *Radiology*, 218: 261-266 (2001).
- [6] V. Ntzalachristos, A.G.Yodh, M. Schnall and B. Chance, "Concurrent MRI and diffuse optical tomography of breast after indocyanine green enhancement, *PNAS* vol. 97 (6), 2267-2772, 2000
- [7] G. Rahbar, A. C. Sie, G.C. Hansen, J. S. Prince, M. L. Melany, H. Reynolds, V. P. Jackson, J. W. Sayre and L. W. Bassett, "Benign versus malignant solid breast masses: US differentiation," *Radiology* 213, 889-894 (1999).

- [8] V. P. Jackson, "The current role of ultrasonography in breast imaging," *Radiol Clin North Am* **33**, 1161-1170 (1995).
- [9] F.M. Hall, J.M. Storella, D.Z. Silverstone, et al., "Non-palpable breast lesions: recommendations for biopsy based on suspicious carcinoma of mammography," *Radiology* **167**, pp.353-358 (1988).
- [10] Stavros TA, Thickman D, Rapp C, "Solid breast nodules: Use of sonography to distinguish between benign and malignant lesions," *Radiology* 1995; **196**: 123-134.
- [11] Zhu, Q., Conant E. and Chance B., "Optical imaging as an adjunct to sonograph in differentiating benign from malignant breast lesions," *Journal of Biomedical Optics*, Vol.5, No2., 229-236, April 2000.
- [12] Zhu, Q., Durduran, T., Holboke, M., Ntziachristos, V. and Yodh, A., "A imager that combines near infrared diffusive light and ultrasound," *Optics letters*, (24) No.15, Aug. 1, 1999.
- [13] Zhu, Q, Chen, NG, Piao DQ, Guo, P and Ding, XH, "Design of near infrared imaging probe with the assistance of ultrasound localization," July 1, *Applied Optics*.
- [14] Chen, NG, Guo, PY, Yan, SK, Piao DQ, and **Zhu, Q.**, "Simultaneous near infrared diffusive light and ultrasound imaging," Accepted by *Applied Optics* (June 2001).
- [15] Zhu, Q, Chen, NG and Kurtzman, S, "Imaging tumor angiogenesis using combined near infrared diffusive light and ultrasound," *Optics Letters*, Accepted.
- [16] Chen, NG and Zhu, Q., "Characterization of small absorbers inside turbid media" *Optics Letters*, (27) No.4., 252-254, Feb., 2002.
- [17] Vaupel P, Kallinowski F, Okunieff P., "Blood flow, oxygen and nutrient supply, and metabolic microenvironment of human tumors: a review," *Cancer Research* **49**, 6449-6465, 1989
- [18] Huang, MM, Xie, TQ, Chen, NG and Zhu, Q, "NIR imaging reconstruction with ultrasound localization: feasibility study using transmission geometry," submitted to *Applied Optics* (July 2002).

Appendices:

Publications (from august 2000 to Sept 2002)

- [1] Huang, MM, Xie, TQ, Chen, NG and Zhu, Q, "NIR imaging reconstruction with ultrasound localization: feasibility study using transmission geometry," submitted to *Applied Optics* (July 2002).
- [2] Zhu, Q., Chen, NG and Kurtzman, S., "Imaging tumor angiogenesis using combined near infrared diffusive light and ultrasound" *Optics Letters*, Accepted.
- [3] Chen, NG and Zhu, Q., "Characterization of small absorbers inside turbid media" *Optics Letters*, (27) No.4., 252-254, Feb., 2002.
- [4] Zhu, Q., Chen, NG, Guo, PY, Yan, SK and Piao, DQ, "Near Infrared Diffusive Light Imaging with Ultrasound Localization" *OSA Optics and Photonics News*, Optics in 2001, 12:31, Dec. 2001.
- [5] Chen, NG, Guo, PY, Yan, SK, Piao, DQ, and Zhu, Q., "Simultaneous near infrared diffusive light and ultrasound imaging" *Applied Optics*, Vol.40, No.34, 6367-6380, Dec., 2001.

[6] Zhu, Q, Chen, NG, Ding, XH, Piao DQ, and Guo, PY, "Design of near infrared imaging probe with the assistance of ultrasound localization," *Applied Optics*, July, Vol. 40, No. 19, 3288-3303, 2001.

List of conference proceedings related to this project (from august 2000 to august 2002)

Conference Proceedings

Huang MM, Xie TQ, Chen NG, Piao DQ and Zhu Q., "2-D NIR imaging reconstruction with ultrasound guidance", *IEEE International Symposium on Biomedical Imaging*, WP-P2.17, 1031-1034, Washington D.C. , July 7-10, 2002

Zhu Q., Chen NG, Kurtzman, S, "Breast lesion diagnosis using combined near infrared diffusive light and ultrasound: initial clinical results", *Optical Society of America, Biomedical Topical Meetings, Technical Digest*, PD 18 1-3, Miami Beach, Florida, April 7-10, 2002

Huang MM, Xie TQ, Chen NG, Zhu Q., "NIR imaging reconstruction with ultrasound guidance", *Optical Society of America, Biomedical Topical Meetings, Technical Digest* SUD12-1 84-87, Miami Beach, Florida, April 7-10, 2002

Chen NG and Zhu Q, "Nonlinear correction method for characterizing small absorbers in turbid media", *Optical Society of America, Biomedical Topical Meetings, Technical Digest* WC8-1 689-691, Miami Beach, Florida, April 7-10, 2002.

Guo, PY, Yan, SK and Zhu Q., "Elevation Beamforming Performance of a 1.75D array", *Proceeding of Ultrasonics Symposium*, 1113-1115, Oct 2001.

Zhu, Q. Chen, NG, Guo, PY, Yan, SK, Piao, DQ "Near infrared imaging probe design with ultrasound guidance," *SPIE Proc.*, Vol. 4256, pp 221-232 (2001).

Chen, NG, Guo, PY, Yan, SK, Piao, DQ and Zhu, Q., "Ultrasound assisted NIR imaging for breast cancer detection," *Proceedings of Optical Tomography and Spectroscopy of Tissue*, SPIE Vol. 4250, pp 546-557 (2001).

Zhu, Q. Chen, NG, Guo, PY, Yan, SK, "Medical Ultrasound with Simultaneous Dual-band Near-Infrared Diffusive Light Imaging and Co-registration," *Proceedings of 4th Annual Conference on Information Fusion*, WeC319:24 (2001).

Chen, NG. and Zhu, Q, "Optical tomography with early arriving photons: sensitivity and resolution analysis," *Proceedings of Optical Tomography and Spectroscopy of Tissue*, SPIE Vol. 4250, pp37-44, (2001).

Guo, PY, Yan, SK and Zhu, Q., "The design of a 1.75-D 1280-channel ultrasound imaging system," *Proceedings of the IEEE27th Northeast Bioengineering Conference*, pp 49-52, 2001.

Yan, SK, Guo, PY and Zhu, Q., "Beamforming scheme and parameter tradeoff in a 1.75D ultrasound array design, Proceedings of the IEEE 27th Northeast Bioengineering Conference, pp 61-62, 2001.

N. G. Chen, and Q. Zhu, "Novel Image Reconstruction Algorithm for NIR Diffusive Tomography," Proceedings of the IEEE 27th Annual Northeast Bioengineering Conference, pp 43-44 (2001)

M. Huang, P. Guo, N. G. Chen, and Qing Zhu, "Preliminary experiment results of 1.75D ultrasound array," Proceedings of the IEEE 27th Annual Northeast Bioengineering Conference, pp 51-52 (2001).

NIR imaging reconstruction with ultrasound localization: feasibility study using transmission geometry

Minming Huang, Tuqiang Xie, Nan Guang Chen and Quing Zhu*

Electrical and Computer Engineering Department

University of Connecticut, Storrs, CT 06269

Abstract

In this paper we report experimental results of NIR imaging reconstruction with ultrasound localization. NIR data were obtained from frequency domain and DC systems with source and detector fibers configured in transmission geometry. Both high and low contrast targets located closer to the boundary and closer to the center of the turbid medium were reconstructed using NIR data only and NIR data with ultrasound localization. Results have shown that the improvements of reconstructed mean absorption coefficients of high-contrast targets range from 20-26% to 67-87% with ultrasound localization. The measured FWHMs have been improved from 210-250% to 110-120% of the true target size with ultrasound localization. For low contrast target cases, the targets were hardly recognizable for both on center and off-center cases with NIR data obtained from both systems. With ultrasound localization, the reconstructed mean absorption coefficients were within 67% of the true value and the target can be visualized. When the change of target scattering coefficient was small from the background medium, the performance of the DC system was comparable to that of the frequency domain system.

* Correspondence: Quing Zhu, Electrical and Computer Engineering Department, University of Connecticut, 260 Glenbrook Road, CT 06269.
Phone: 860-486-1815; Fax: 860-486-2447; E-mail: zhu@engr.uconn.edu; <http://www.engr.uconn.edu/ece/faculty/zhu.html>.

OCIS codes: 170.0170, 170.3010, 170.5270, 170.7170, 170.3830

Introduction

Functional imaging with near infrared (NIR) light has found potential applications in many areas.¹⁻⁹ However, one fundamental problem that we have to overcome is the intense scattering of light. As a result, diffusive light probes a widespread region instead of providing information along a straight line. Multiple measurements are always correlated as a result of the overlapping of probed regions. Therefore, increasing the total number of measurements does not necessarily provide more independent information for image reconstruction. In general, the inverse image reconstruction is underdetermined and ill-posed. The behavior of reconstruction algorithms is affected by many factors, such as system signal to noise ratio, probe configuration, and the regulation schemes used in image reconstructions.

Current approaches of image reconstruction algorithms are 1) simple back projection methods,³⁻⁴ 2) perturbation methods,¹⁰⁻¹² and 3) finite element methods (FEM).¹³⁻¹⁵ The back projection method provides real time estimation of coarse optical properties of lesions. However, the reconstructed image resolution was low and the lesions that appeared in images were often displaced from true locations. Perturbation methods are, in general, based on linear approximations to the heterogeneous functions. Born and Rytov approximations are examples. Measurements made between the background and the heterogeneous medium were used to relate optical signals at the measurement surface to absorption and scattering variations in each volume element within the sample. The least square method was, in general, used to formulate the inverse problem. Iterative search methods, such as conjugate gradient techniques, were employed to iteratively solve the inverse problem. However, accurate estimation of the target optical properties depends on the accurate estimation of the background optical properties, which

are, in general, not easy to obtain in breast tissues. In addition, when the absorption or the scattering coefficients of the lesions are significantly higher than the background, the linear perturbation methods will not give accurate optical properties. Reconstructions based on finite element methods provide higher order estimations to heterogeneous functions. However, as the scattering and absorption coefficients are expanded over local basis functions, the number of unknowns is increased considerably. Nonetheless, the independent information from diffuse light is limited, and it will essentially stop to increase when the source-detector pairs reach a certain number. In this case, the inverse problem will become more ill-posed, and the behavior of the reconstruction algorithm may be unpredictable.

Reconstructions with the aid of *a priori* target geometry information provided by co-registered ultrasound have shown promising results in improving the accuracy of reconstructed optical properties and the localization of targets.¹⁶⁻¹⁹ In this method, an ultrasound probe and NIR source and detector fibers have been deployed on a hand-held probe and configured in the reflection geometry. The *a priori* tissue type and lesion location as well as shape provided by co-registered ultrasound can guide the NIR image reconstruction to localized target regions. Therefore, the total number of voxels with unknown optical properties can be reduced significantly and the inversion becomes overdetermined. In general, the solution is unique and the iterative algorithms converge very fast.

In this paper we explore experimentally the utility of the combined imaging with NIR sources and detectors configured in transmission geometry. The standard pulse-echo technique is used to obtain co-registered ultrasound images. Compared with NIR reflection geometry,

transmission geometry may have the advantage of reduced target dynamic range and higher sensitivity. In the reported experiments, the FEM forward solver is used to generate a Jacobian weight matrix for the NIR image reconstruction, and the inversion is performed by using NIR data only and NIR data with *a priori* target geometry provided by co-registered ultrasound.

Frequency domain and DC systems are frequently used by many research groups. The advantage of using frequency domain system is that both amplitude and phase information can be obtained and, therefore, simultaneous reconstruction of absorption and scattering coefficients is feasible. The disadvantage is the complexity in constructing high frequency transmission and reception circuitries, particularly when many parallel channels are needed for fast data acquisition. This situation is more pronounced when nearly 100 source and detector positions are needed for 3-D imaging in transmission geometry. In addition, the system cost is high. DC systems have advantages of simplicity in circuit construction and low cost. The drawbacks are that the phase information is not available and the cross-talk between the reconstructed absorption and scattering coefficients may be unavoidable. However, where reconstruction of lesion absorption maps is concerned, frequency domain and DC systems may demonstrate similar performance. In this paper, we have compared the performance of both systems in constructing absorption maps under the conditions of NIR reconstruction only and ultrasound guided NIR reconstruction.

2. Forward model

We have adopted a commercial CFD package FLUENT, which allows users to change the governing equation through user defined source functions. The steady-state governing equation for transport of a scalar quantity ϕ in FLUENT is

$$-\frac{\partial}{\partial x_i}(\Gamma_R \frac{\partial \phi_k}{\partial x_i}) = S_{\phi_k}, \quad k = 1, \dots, N \quad (1)$$

where Γ_R is the diffusion coefficient of ϕ , S_{ϕ_k} is the source of ϕ per unit volume, and k is the index of image voxel number. We have replaced the source S_{ϕ_k} in Eq. (1) by the user defined

source $\hat{S}_{\phi_k} = S_{\phi_k} - \mu_a \phi_k$ and obtained a new governing equation as

$$-\frac{\partial}{\partial x_i}(D \frac{\partial \phi_k}{\partial x_i}) + \mu_a \phi_k = \hat{S}_{\phi_k}. \quad (2)$$

This is the photon diffusion equation, where μ_a is the absorption coefficient and Γ_R is replaced

by the photon diffusion coefficient $D = \frac{1}{3(\mu_s + \mu_a)}$. μ_s is the reduced scattering coefficient.

To obtain the frequency domain forward model, we have used the transient governing equation

$$\frac{\partial \phi_k}{\partial t} - \frac{\partial}{\partial x_i}(D \frac{\partial \phi_k}{\partial x_i}) + \mu_a \phi_k = \hat{S}_{\phi_k} \quad (3)$$

to obtain time domain waveforms and then calculate the DC component, amplitude and phase of each waveform. The step used in the time domain waveform calculation is 1/3 of the period T , where $T = 1/f$ and $f = 140\text{MHz}$, which is the modulation frequency of our experimental system.

Assume that the change of D is small and the scattering wave is primarily generated by the absorption inhomogeneity. The Jacobian matrix $W_{ij} = \frac{\Delta\phi_{ij}}{\Delta\mu_{aj}}$, that relates the scattering wave at boundary cell i and imaging voxel j with absorption coefficient change $\Delta\mu_{aj}$, is given as

$$[W_{ij}] = \begin{bmatrix} \frac{\Delta\phi_{11}}{\Delta\mu_{a1}} & \dots & \frac{\Delta\phi_{1L}}{\Delta\mu_{aL}} \\ \frac{\Delta\phi_{21}}{\Delta\mu_{a1}} & \dots & \frac{\Delta\phi_{2L}}{\Delta\mu_{aL}} \\ \vdots & \ddots & \vdots \\ \frac{\Delta\phi_{M1}}{\Delta\mu_{a1}} & \dots & \frac{\Delta\phi_{ML}}{\Delta\mu_{aL}} \end{bmatrix}, \quad (4)$$

where M is the total number of boundary cells and L is the total number of imaging voxels.

3. Computation procedures

We have used a two-dimensional mesh with 4106 triangle elements and 2130 nodes (see Fig 1).

The radius of physical boundary is chosen as 45.72 cm and the extrapolation distance

($l_r = \frac{1}{\mu_s + \mu_a}$) is calculated as 0.167 cm, where $\mu_s + \mu_a$ is the background value and is chosen as 6 cm^{-1} .

In Jacobian matrix calculation, we have evaluated the linearity of $\frac{\Delta\phi_{ij}}{\Delta\mu_{aj}}$ verse $\Delta\mu_{aj}$ with

μ_{aj} changing from 0.02 cm^{-1} to 0.22 cm^{-1} at many cell locations. The linearity is related to the

distance between the cell and the source, and the linearity is better when the distance is larger. The worst case is that the cell j is next to the source cell. For the DC component, this dependence is not significant, and the error due to the linearity approximation is always less than 0.5%. For frequency domain calculations, the real and imaginary part of ϕ_{ij} of several cells are one or two orders smaller, and they are very sensitive to small perturbations. However, even for the worst case, the error due to the use of linear approximation is also less than 0.7% for 306 out of 308 cells at source-detector layer (See Fig 1). Therefore, we have simplified the Jacobian matrix calculation by computing $\frac{\Delta\phi_{ij}}{\Delta\mu_{aj}}$ at two points $\mu_{aL} = 0.02 \text{ cm}^{-1}$ and $\mu_{aH} = 0.22 \text{ cm}^{-1}$. Figure 2 shows ϕ_{ij} verse μ_{aj} with μ_{aj} varies from 0.02 cm^{-1} to $\mu_{aj} = 0.22 \text{ cm}^{-1}$, where cell j is located at the center. Figure 2(a) is the real part of ϕ_{ij} verse μ_{aj} , and Fig. 2 (b) is the imaginary part of ϕ_{ij} verse μ_{aj} . Figure 2(c) is the DC component of ϕ_{ij} verse μ_{aj} .

The experimental data have included many unknown systematic factors (unknown source and detector gains, etc.). To remove those unknown factors, we have used the normalized difference method (NDM) given in Ref 20 as

$$\left[\frac{\phi_{m(i)} - \phi_{mr(i)}}{\phi_{mr(i)}} \cdot \phi_{cr(i)} \right] = [W_{ij}] \cdot [\Delta\mu_{a(ij)}] \quad (5)$$

where $\phi_{m(i)}$ is the measured heterogeneous data associated with the source-detector pair i with the target in the homogeneous medium, $\phi_{mr(i)}$ is the measured homogeneous data, $\phi_{cr(i)}$ is the calculated forward homogeneous data used for weight matrix calculation. ϕ is a complex value in frequency domain case. The unknown system factors present in both sets of measured

heterogeneous and homogeneous data are cancelled by taking the ratio of the perturbation (heterogeneous – homogeneous) and the reference (homogeneous) measurements.

The conjugate gradient method is used for the inversion. Since the error function

$$\|W \cdot \Delta\mu_a - \frac{\phi_{m(i)} - \phi_{mr(i)}}{\phi_{mr(i)}} \cdot \phi_{cr(i)}\|^2$$
 reduces consistently and becomes flat after certain iterations (around

30 for reconstruction with NIR data only, and 3 for NIR with ultrasound guidance), the stopping criteria are chosen to be 100 and 3 iterations for NIR only and NIR with ultrasound localization, respectively. The corresponding computation time is around 3 minutes for NIR data only and 30 seconds for NIR with ultrasound information.

In experiments, data are obtained from the 3D model (finite cylindrical medium and finite length target). However, the Jacobian matrix computation is based on the 2D model (infinite cylindrical medium and infinite length target). According to Refs 21 and 22, the 2D/3D difference between intensity is reasonably independent of source-detection separation, and it is reasonable to correct it by simply multiplying or dividing a constant. Therefore, NDM not only cancels the unknown source detector gains but also partially eliminates the 2D/3D model mismatch by taking the ratio of the perturbation and the reference measurements.

According to Refs 21 and 22, the 2D/3D model mismatch can cause some artifacts near the boundary. We have used constraints based on the assumption that there are no perturbations outside the detector and source layer to partially eliminate the artifacts.

4. Experimental systems

To compare the performance of frequency domain and DC systems without and with ultrasound localization, we have constructed both systems. The details of our multi-source and multi-detector frequency domain system can be found in Ref. 18. Briefly, it consists of 12 pairs of dual wavelength sources (780 nm and 830 nm) and 8 parallel detectors. The light sources are laser diodes amplitude modulated at 140 MHz, and the detectors are photon multiplier tubes (PMT's). These sources and detectors are coupled to the medium through optical fibers.

Our new DC system consists of 6 pairs of dual-wavelength laser diodes (780 nm and 830 nm) amplitude modulated at 20 KHz to avoid DC fluctuations (see Fig. 3). 12 detector fibers are sequentially coupled to a PMT through a mechanical multiplexer, which uses a stepper motor to accurately collimate a coupling light guide on a rotation plate to one of detection fibers. Each light source has two output levels of 30 dB difference to avoid PMT saturation and improve the system dynamic range. A National Instrumentation data acquisition (DAQ) card is used to generate sinusoidal waveforms on top of a constant current to drive one laser diode at a time. The photon density wave detected by the PMT is amplified and then digitized by the same DAQ card. The corresponding amplitude is retrieved from the acquired waveform on a PC. The digital ports of the DAQ card are used to switch laser diodes sequentially, control the output level, and input a feedback signal for close-loop stepper motor control. The total data acquisition time for a complete data set is around 1 minute.

Since our DC system is modulated at 20 kHz, the measured amplitude is an AC signal instead of the DC component we used for forward Jacobian matrix calculation. We have estimated the

difference using a spherical wave of light energy density ($e^{(jk\rho)} / D\rho$) of two wave numbers $k_1 = \sqrt{-\mu_a / D}$ and $k_2 = \sqrt{(-\mu_a + j \times \omega / c) / D}$, where $\omega = 2\pi \cdot 2 \times 10^4$ Hz, c and D are the speed of light and the reduced diffusion coefficient, respectively. The normalized difference $\frac{e^{(jk_1\rho)} - e^{(jk_2\rho)}}{e^{(jk_1\rho)}}$ can be approximated as $-\frac{j\rho\omega}{2c} \sqrt{1/(D \cdot \mu_a)}$, and it is larger when the wave propagates deeper into the tissue and the background absorption is smaller. For the worst case of $\mu_a = 0.01 \text{ cm}^{-1}$ and $\rho = 10\text{cm}$, the difference is less than $3.295\text{E-}5$. Therefore, we directly use the Jacobian matrix calculated from the DC component to relate the measured amplitude data for the inversion.

During experiments, source and detector fibers were placed on a circular plane (see Fig 4). A commercial ultrasound probe of 3.5 MHz central frequency was placed on the top of a water tank filled with Intralipid. This one-dimensional commercial probe provides cross-section image in y-z imaging plane (called B-scan), where y is the lateral direction and z is the propagation direction. By translating the probe mechanically in x direction, we acquired the 3-D volumetric image data. Windowing the 3D data in z direction at a particular depth provides the 2D target spatial images at x-y plane (called C-scan). C-scans are co-registered with NIR images. 0.6% Intralipid solution was used as a homogeneous background. The fitted μ_a and μ_s of the Intralipid at 780 nm were 0.02cm^{-1} and 6cm^{-1} , respectively.

Since we have a limited number of source and detector positions, we have placed 8 source fibers at a quarter circle and 8 detector fibers at the opposite quarter for frequency domain measurements (see Fig.5 (a)). For DC measurements, we placed 6 source fibers at a quarter circle

and 12 detector fibers at the opposite quarter (see Fig.5 (b)). After obtaining one set of heterogeneous NIR data with a target in the Intralipid (8 x 8 measurements for the frequency system, 6 x 12 measurements for the DC system), we simply rotated the target by 90° for frequency domain system and 77.14° for the DC system to get another set of data, respectively. Figure5 (c) shows the rotation scheme used during frequency domain experiments. Three rotations were performed to obtain one complete data set for reconstruction, which covered 360° . For DC measurements, a similar rotation scheme was used and four rotations were performed to obtain one complete data set. 3-D ultrasound data were obtained simultaneously with NIR data acquisition.

5. Results

For NIR reconstruction using transmission geometry, the target dynamic range is related to the location of the target and the contrast of the target. It is much harder to reconstruct a low contrast target located at the middle of the 2D mesh. In our experiments, a nearly circular target (high/ low contrast) with 1.0cm diameter was placed at two typical locations (at the center, closer to the boundary). The target was made of an acrylamide gel¹⁶ with calibrated μ_a . For the high contrast case, the absorption coefficient of the target was 0.20 cm^{-1} , which was 0.18 cm^{-1} above the background. For the low contrast case, the calibrated absorption coefficient of the target was 0.10 cm^{-1} , which was 0.08 cm^{-1} above the background.

A. Reconstruction using frequency domain system

Figure 6 shows experimental results of a 1.0 cm-diameter cylindrical target of $\mu_a = 0.2 \text{ cm}^{-1}$ located closer to the boundary. The reduced scattering coefficient μ_s' was controlled the in the

same way as the background which was 6 cm^{-1} . Figure 6 (a) is the μ_a distribution reconstructed using NIR data only. We calculated the mean value for the pixels with absorption coefficients greater than the half maximum in the target mass region. The reconstructed mean absorption coefficient was only 24% of the true value, and the full width at half maximum (FWHM) was around 2.2cm, which was 220% of the true target size. Figure 6 (c) is a B-scan ultrasound image, and Figure 6 (d) is the C-scan ultrasound image obtained at the source-detector plane. The ultrasound image was segmented first and then a threshold was used to map out target and non-target regions. The inverse reconstruction was localized to the target region. Figure 6 (b) is the reconstructed μ_a distribution with co-registered ultrasound localization. With ultrasound localization, the accuracy of reconstructed mean μ_a was improved from 24% to 75% of the true value. The FWHM was improved to 1.16 cm, which was only 16% larger than the true value. Figure 6 (e) shows the comparison of the reconstructed μ_a distribution along the x-axis as indicated by vertical arrows in (a), and Fig. 6 (f) shows the comparison of reconstructed μ_a distribution along the y-axis as indicated by horizontal arrows in (a).

Figure 7(a) shows the reconstructed μ_a distribution of the same high contrast target located at the middle. As one can see, the spatial distribution is poor and the reconstructed mean μ_a was about 26% of the true value. Figure 7(b) is the co-registered C-scan image of ultrasound and Fig.7 (c) is the reconstructed NIR absorption map with ultrasound localization. The reconstructed mean μ_a value has improved to 26% and 67% of the true value.

For a lower contrast target ($\mu_a = 0.1 \text{ cm}^{-1}$) located at different locations, the reconstructed images were dominated by artifacts. Figure 8 shows the reconstructed absorption maps without (part (a)) and with (part (b)) ultrasound localization when the target was located closer to the boundary. Without ultrasound, the target cannot be recognized. With ultrasound, the mean reconstructed absorption coefficient was 78% of the true value.

Table I summarizes the experimental results of two cases when the target was located at different positions. In general, when the target was located at the middle, the results obtained with NIR data only were slightly poorer than those when the target was located closer to the boundary, and the improvements with ultrasound localization were similar to those when the target was located at the boundary.

B. Reconstruction using the DC system

Figure 9 shows experimental results of the 1.0 cm-diameter cylindrical target of $\mu_a = 0.2 \text{ cm}^{-1}$ located closer to the boundary. Figure 9 (a) is the μ_a distribution reconstructed using NIR data only. The reconstructed mean absorption coefficient was 22% of the true value, and the FWHM was around 2.5cm, which was 2.5 times that of the true target size. Figure 9 (b) is the co-registered C-scan ultrasound image obtained at the source-detector plane. Figure 9 (c) is the reconstructed μ_a distribution with ultrasound localization. The accuracy of reconstructed mean μ_a was improved to 77% of the true value. The measured FWHM with ultrasound localization was 1.18 cm, which was only 18% larger than the true value. Figure 9 (d) and (e) show the comparison of the reconstructed μ_a distributions along x-axis and y-axis, respectively.

The reconstructed absorption map is dominated by artifacts for the lower μ_a (0.1 cm^{-1}) case. Figure 10 shows a low contrast target located closer to the boundary. The target can only be visualized with ultrasound localization.

Table II summarizes experimental results of high and low contrast cases when the target was located at different positions. The reconstructed absorption coefficients and improvements with ultrasound localization are comparable to those obtained from the frequency domain system.

Comparing results obtained from frequency domain and DC systems, we find no significant difference with respect to accuracy and target spatial distributions. The reconstructed absorption values of using NIR data only obtained from both systems are very close. With ultrasound localization, the mean absorption coefficients obtained by the DC system are about 9-13 % higher than the frequency domain results for the low contrast target case. For the high contrast target case, the reconstruction results are similar.

6. Discussions

Based on our experimental results, the reconstructed values by using NIR only are certainly low and the target spatial distributions are poor. These problems can be partially improved by iteratively updating the Jacobian matrix to account for higher order terms of the weight matrix. However, this procedure is time-consuming and prohibits near real-time NIR image processing. With the guidance of spatial target distribution provided by ultrasound, the reported mean reconstruction results are within 67% to 87% of the true absorption coefficients when the first order linear approximation is used. Iterative updating of the localized Jacobian matrix could

further improve the accuracy of reconstructed absorption coefficients with reduced computation load. Currently, we are pursuing this research and results will be reported in the near future.

In the Jacobian matrix computation, we have calculated $\frac{\Delta\phi_{ij}}{\Delta\mu_{aj}}$ cell by cell by assuming that high order cross-talk terms between cells are negligible. This assumption is equivalent to using a linear approximation of $\Delta\phi$ as

$$\begin{aligned} & \phi(\mu_{ai} + \Delta\mu_{ai}, \mu_{aj} + \Delta\mu_{aj}, \dots, \mu_{al} + \Delta\mu_{al}) - \phi(\mu_{ai}, \mu_{aj}, \dots, \mu_{al}) \\ & \approx \frac{\Delta\phi}{\Delta\mu_{ai}} \Delta\mu_{ai} + \frac{\Delta\phi}{\Delta\mu_{aj}} \Delta\mu_{aj} + \dots + \frac{\Delta\phi}{\Delta\mu_{al}} \Delta\mu_{al} \end{aligned} \quad (6)$$

where index i, j, \dots, l are cell index numbers. To estimate the error due to the linear approximation, we calculated the difference between $\Delta\phi$ and its linear approximation at several locations (next to the source, 1cm away from the source, at the middle of the mesh). The error is less than 1.8% for four cells (0.3 cm target size), 7.9% for eight cells (0.6 cm target size), and 27% for 28 cells (1.0 cm target size).

In the reported phantom studies, we assume that the lesions are isolated and are imbedded in a homogeneous background. Therefore, we localize the image reconstruction by using target geometry obtained from ultrasound. In the clinical breast imaging cases, the background tissues also scatter and absorb the diffusive light, and constraints on the background perturbation will be used to account for the scattering and absorption contributions from the background.²³

In this paper, the combined imaging has been demonstrated using transmission geometry for imaging absorbers. In principle, the combined imaging is possible for imaging scattering targets

as well. Simultaneous reconstruction of absorbing and scattering contrasts are more difficult because of the crosstalk between them, particularly when the DC system is used. However, further investigation will be conducted along this direction.

Due to the fact that the 2D/3D data difference is not exactly linear dependent, some artifacts are visible in the boundary regions of reconstructed absorption maps when NIR data are used. For the lower contrast target case, this effect is dominant and the target can only be reconstructed by using a *priori* target information provided by ultrasound. Since photons travel in three dimensions, 3D meshes are more appropriate and we are currently working on 3-D model constructions and experimentations.

7. Summary

This paper reports experimental results of NIR imaging reconstruction with ultrasound localization. Transmission geometry was used for NIR imaging reconstruction and standard pulse-echo ultrasound was used for obtaining co-registered ultrasound images. The results have shown that reconstructed mean absorption coefficients of phantom targets have improved from 24% to 75% and 26% to 67% for a high-contrast target located closer to the boundary and closer to the center of the turbid medium, respectively, when a frequency domain system is used. Similarly, the reconstructed mean absorption coefficients have improved from 22% to 77% and 20% to 76% for the same high-contrast target located closer to the boundary and closer to the center of the turbid medium, respectively, when a DC system is used. The reconstructed absorption maps were poor in general when targets were located at the center of the turbid medium. Ultrasound localization improves the accuracy of reconstructed values and reduces

image artifacts. With ultrasound localization, the measured FWHMs have been improved from 210-250% to 110-120% of the true target size. For a low contrast target, the target was hardly recognizable for both closer to boundary and closer to center cases with NIR data obtained from both systems. With ultrasound localization, the reconstructed absorption coefficients were within 67% of the true value and the target can be visualized. With ultrasound localization, the reconstruction speed has improved by a factor of 10 and near real-time optical imaging becomes feasible. Under the condition that the change of scattering coefficient is small, the performance of the DC system is comparable to that of the frequency domain system.

Acknowledgments

Graduate students Shikui Yan and Daqing Piao are greatly acknowledged for their continuous help on the software development of the DC system and mechanical setup of the experimental system. The authors would like to thank the following for their funding support: the State of Connecticut (99CT21 Yankee), DOD ARMY Breast Cancer Program (DAMD17-00-1-0217, DAMD17-01-1-0216), and Donaghue Foundation. The authors greatly appreciate the donation of a prototype DC system by Multi-Dimensional Technology Inc. The DC system used was modified from the prototype.

References:

1. B. Tromberg, N. Shah, R. Lanning, A. Cerussi, J. Espinoza, T. Pham, L. Svaasand and J. Butler, "Non-Invasive in vivo characterization of breast tumors using photon migration spectroscopy," *Neoplasia*, 2, (1:2): 26-40 (2000).
2. J. B. Fishkin, O. Coquoz, E.R. Anderson, M. Brenner, and B.J. Tromberg, "Frequency-domain photon migration measurements of normal and malignant tissue optical properties in human subject," *Appl. Opt.*, 36: 10-20 (1997).
3. S. Fantini, S. Walker, M. Franceschini, M. Kaschke, P. Schlag, K. Moesta, "Assessment of the size, position, and optical properties of breast tumors in vivo by noninvasive optical methods," *Appl. Opt.*, 37(10): 1982-1989 (1998).
4. R.M. Danen, Yong Wang, X.D. Li, W.S. Thayer, and A.G. Yodh, "Regional Imager for Low Resolution Functional Imaging of the Brain with Diffusing Near-infrared Light," *Photochemistry and Photobiology* 67: 33-40 (1998).
5. B. Pogue, S. P. Poplack, T. O. McBride T. O., W. A. Wells, K. S. Osterman, U. Osterberg, and K. D. Paulsen, "Quantitative hemoglobin tomography with diffuse near-infrared spectroscopy: pilot results in the breast," *Radiology*, 218: 261-266 (2001).
6. B. Chance, J. Glickson, R. Weissleder, C. Tung, D. Blessington, L. Zhou, "High sensitivity and specificity in human breast cancer detection with near-infrared imaging," *OSA Biomedical Topical Meetings, Technical Digest*, 450-455 (2002).
7. E.M. Sevick. G. Lopez, J.S. Reynolds, T.L. Troy and C.L. Hutchinson, "Fluorescence and absorption contrast mechanism for biomedical optical imaging using frequency-domain techniques," *Photochemistry and Photobiology* 66: 55-64 (1997).

8. H. Liu, Y. Song, K. L. Worden, X. Jiang, A. Constantinescu and R.P. Mason, "Noninvasive investigation of blood oxygenation dynamics of tumors by near-infrared spectroscopy," *Appl. Opt.*, 39(28): 5231-5243 (2000).
9. D. A. Boas, D. H. Brooks, E. L. Miller, C. A. DiMarzio, M. Kilmer, R. J. Gaudette and Q. Zhang, "Imaging the body with diffuse optical tomography," *IEEE Signal Processing Magazine* 18(6): 57-75 (2001).
10. X. Li, T. Durduran and A. Yodh, B. Chance and D.N. Pattanayak, "Diffraction tomography for biomedical imaging with diffuse-photon density waves," *Opt. Lett.*, 22: 573-575 (1998).
11. Y. Yao, Y. Wang, Y. Pei, W. Zhu, and R.L. Barbour, "Frequency-domain optical imaging of absorption and scattering distributions by a Born iterative method," *J. Opt. Soc. Am. A* 14: 325-341 (1997).
12. M. A. O'Leary, "Imaging with diffuse photon density waves," Ph.D. dissertation (University of Pennsylvania, Philadelphia, Pa., 1996).
13. H. Jiang, "Frequency-domain fluorescent diffusion tomography: a finite-element-based algorithm and simulations," *Appl. Opt.*, 37 (22): 5337-5343 (1998).
14. K. Paulsen and H. Jiang, "Spatially varying optical property reconstruction using a finite element diffusion equation approximation," *Med. Phy.* 22(6): 691-701 (1995).
15. S. Arridge and M. Schweiger, "Photon-measurement density functions, Part II: Finite-element-method calculations," *Appl. Opt.*, 34(34): 8026-8037 (1995).
16. Q. Zhu, T. Dunrana, M. Holboke, V. Ntziachristos and A. Yodh, "Imager that combines near infrared diffusive light and ultrasound," *Opt. Lett.*, 24(15): 1050-1052 (1999).
17. Q. Zhu, E. Conant and B. Chance, "Optical imaging as an adjunct to sonograph in differentiating benign from malignant breast lesions," *Journal of Biomedical Optics* 5(2): 229-236 (2000).

18. NG. Chen, PY. Guo, SK. Yan, DQ. Piao DQ, and Q. Zhu, "Simultaneous near infrared diffusive light and ultrasound imaging," *Appl. Opt.*, 40 (34): 6367-6380 (2001)
19. NG. Chen, and Q. Zhu, Q, "Characterization of small absorbers inside the turbid medium," *Opt. Lett.*, 27 (4): 252-254 (2002).
20. Y. Pei, H. L. Graber, and R. L. Barbour, "Influence of systematic errors in reference states on image quality and on the stability of derived information for dc optical imaging," *Appl. Opt.*, 40(31): 5755-5769 (2001)
21. E. M. C. Hillman, J. C. Hebden, F. E. W. Schmidt, S. R. Arridge, M. Schweiger, H. Dehghani, and D. T. Delpy, "Calibration techniques and datatype extraction for time-resolved optical tomography," *Review of Scientific Instruments*, 71(9): 3415-3427 (2000).
22. M. Schweiger and S. R. Arridge, "Comparison of two-and three-dimensional reconstruction methods in optical tomography," *Appl. Opt.*, 37 (31): 7419-7428 (1998).
23. Q. Zhu, NG. Chen, S. Kurtzman, "Breast lesion diagnosis using combined near infrared diffusive light and ultrasound: initial clinical results," manuscript in preparation.

Figure Captions

Figure 1. Two dimensional mesh.

Figure 2. $\frac{\Delta\phi_{ij}}{\Delta\mu_{aj}}$ versus $\Delta\mu_{aj}$ with μ_{aj} changing from 0.02 cm^{-1} to 0.22 cm^{-1} for a cell located in the middle of the mesh. (a) Real part of ϕ_{ij} versus μ_{aj} . (b) Imaginary part of ϕ_{ij} versus μ_{aj} . (c) Calculation is made using amplitude of DC data.

Figure 3. Schematic of our new DC system.

AO: analog output; AI: analog input; DO: digital output; DI: digital input.

Figure 4. Experimental setup. A commercial ultrasound probe is located at the top of the water tank and the NIR source and detector fibers are deployed around the tank and configured in transmission geometry.

Figure 5. Configurations of NIR sources and detectors used in the reported experiments (a) Frequency domain experiments. (b) DC experiments. (c) Top view of target rotation scheme used in frequency domain measurements.

Figure 6. Comparison of reconstructed absorption coefficient maps of a high-contrast target located closer to the boundary. (a) Reconstructed μ_a distribution using NIR data only. (b) Reconstructed μ_a distribution with ultrasound localization. (c) B-scan ultrasound image. (d) Co-registered C-scan ultrasound image. (e) Comparison of μ_a distributions along x-axis, pointed

by two vertical arrows in part (a). (f) Comparison of μ_a distributions along y-axis, pointed by two horizontal arrows in part (a).

Figure 7. Comparison of reconstructed absorption maps of a high-contrast target located at the middle of the turbid medium.

(a) Reconstructed μ_a distribution using NIR data only. (b) Co-registered C-scan ultrasound image. (c) Reconstructed μ_a distribution with ultrasound localization.

Figure 8. Comparison of the reconstructed absorption maps of a low-contrast target located closer to the boundary. (a) Reconstructed μ_a distribution using NIR data only. (b) Reconstructed μ_a distribution with ultrasound localization.

Figure 9. Comparison of reconstructed absorption coefficient maps of a high-contrast target located closer to the boundary. DC system of configuration Fig.5 (b) was used for experiments. (a) Reconstructed μ_a distribution using NIR data only. (b) Co-registered C-scan ultrasound image. (c) Reconstructed μ_a distribution with ultrasound localization. (e) Comparison of μ_a distribution along x-axis as pointed by vertical arrows shown in (c). (f) Comparison of μ_a distribution along y-axis as pointed by horizontal arrows shown in (c).

Figure 10. Comparison of reconstructed absorption maps of a low-contrast target located closer to the boundary. DC system experiments. (a) Reconstructed μ_a distribution using NIR data only. (b) Reconstructed μ_a distribution with ultrasound localization.

Table I. Experimental results obtained from the frequency domain system

Target location	NIR only (Mean μ_a (cm ⁻¹))	NIR + US (Mean μ_a (cm ⁻¹))	True value (Mean μ_a (cm ⁻¹))
Closer to the boundary (high contrast)	0.048(24%)	0.149(75%)	0.2
(low contrast)	--	0.078(78%)	0.1
At the middle (high contrast)	0.052(26%)	0.134(67%)	0.2
(low contrast)	--	0.072(72%)	0.1

Table II. Experimental results obtained from the DC₂ system

Target location	NIR only (Mean μ_a (cm ⁻¹))	NIR + US (Mean μ_a (cm ⁻¹))	True value (Mean μ_a (cm ⁻¹))
Closer to the boundary (high contrast)	0.0447(22%)	0.153(77%)	0.2
(low contrast)	--	0.087(87%)	0.1
At the middle (high contrast)	0.040(20%)	0.151(76%)	0.2
(low contrast)	--	0.085(85%)	0.1

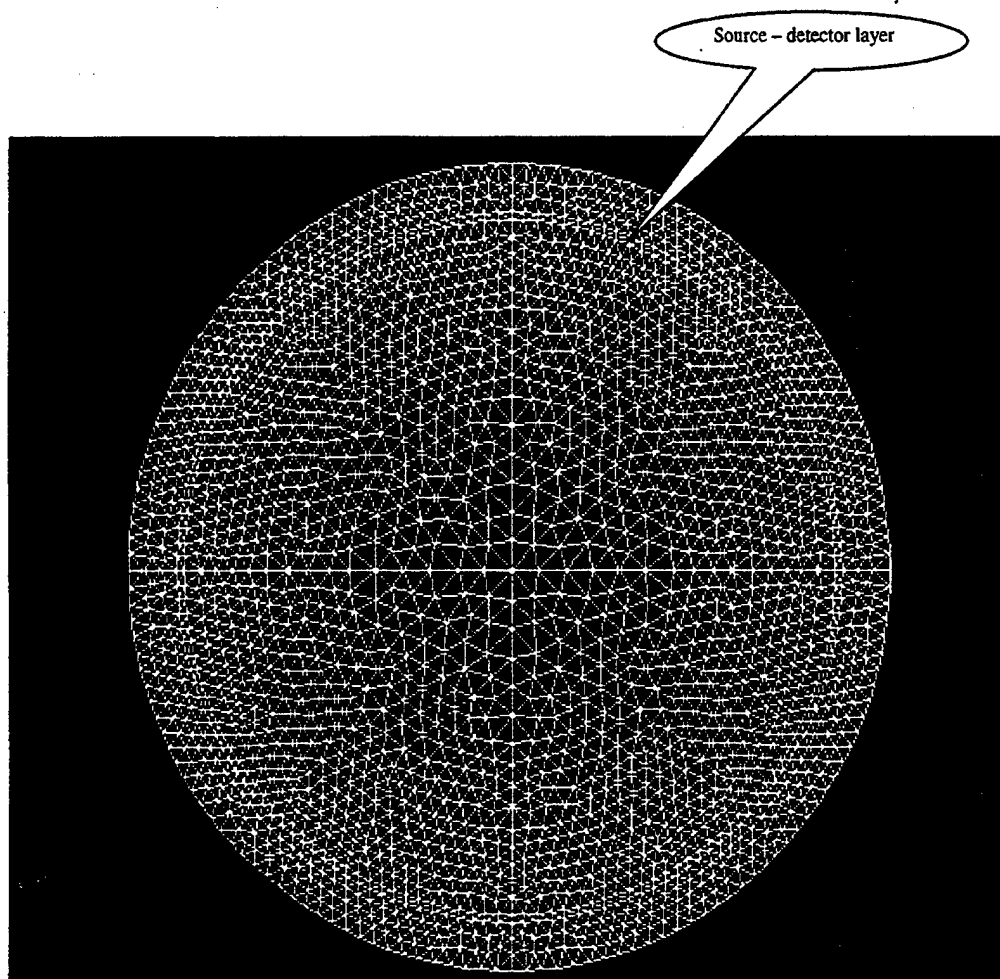
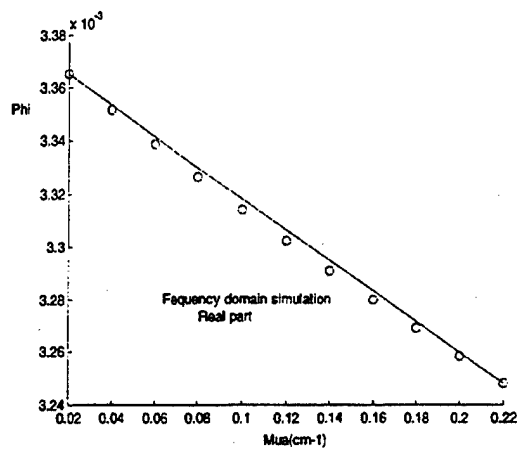
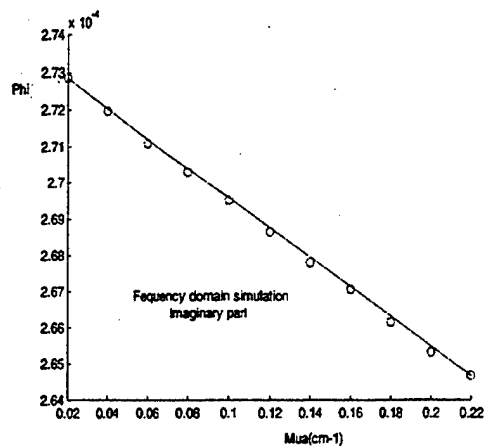


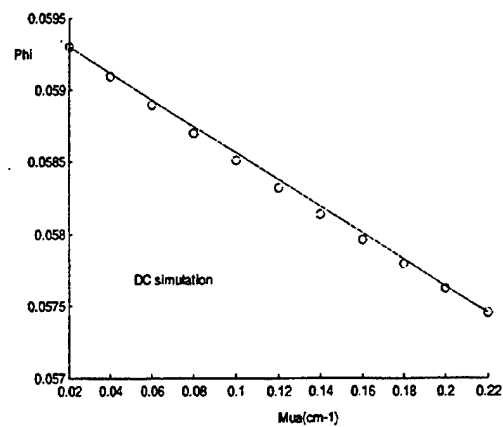
Figure 1.



(a)



(b)



(c)

Figure 2.

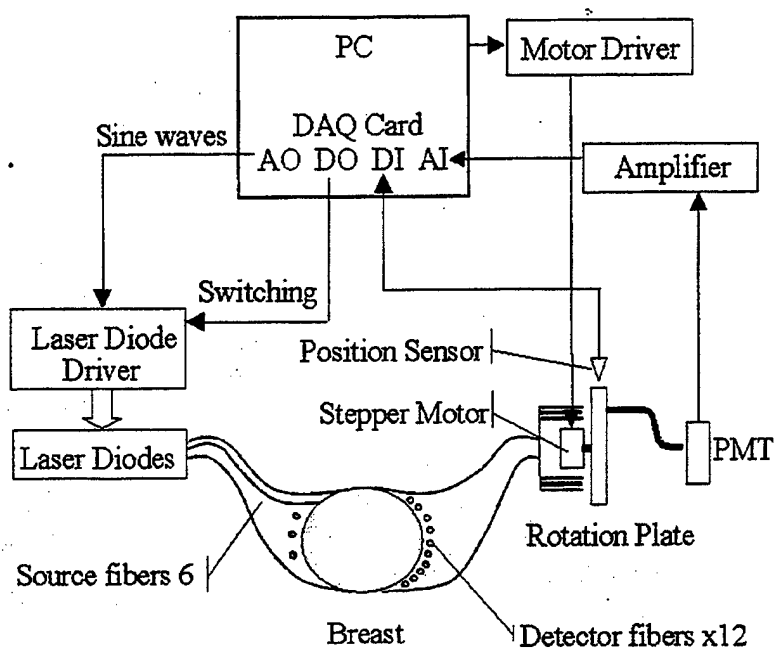


Figure 3.

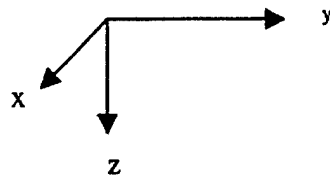
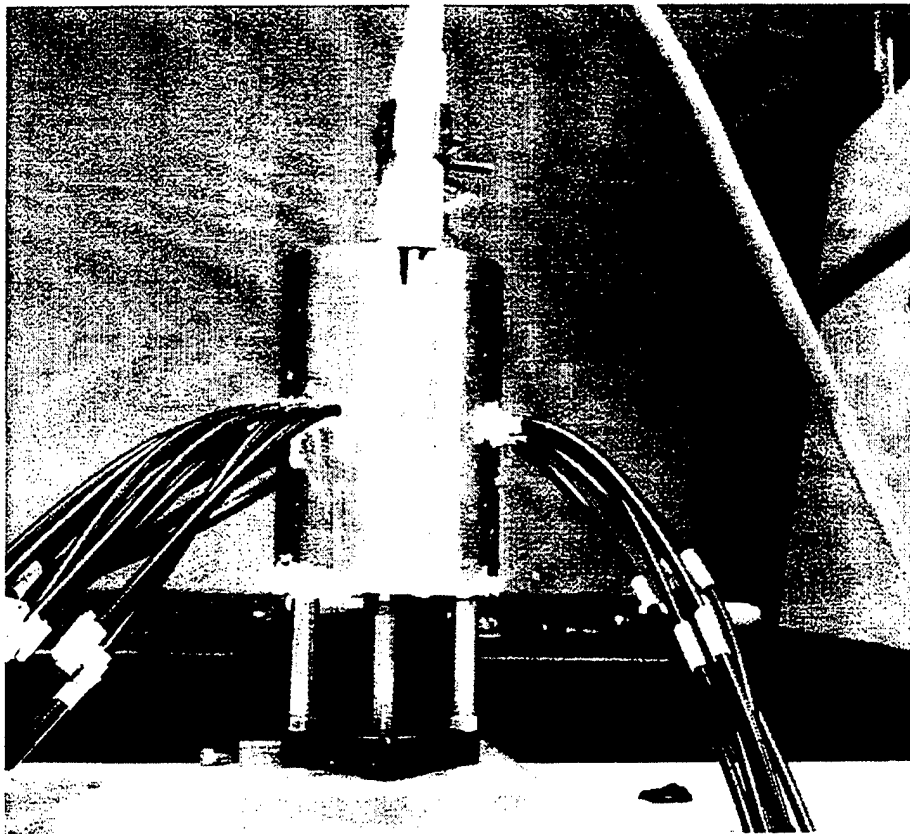
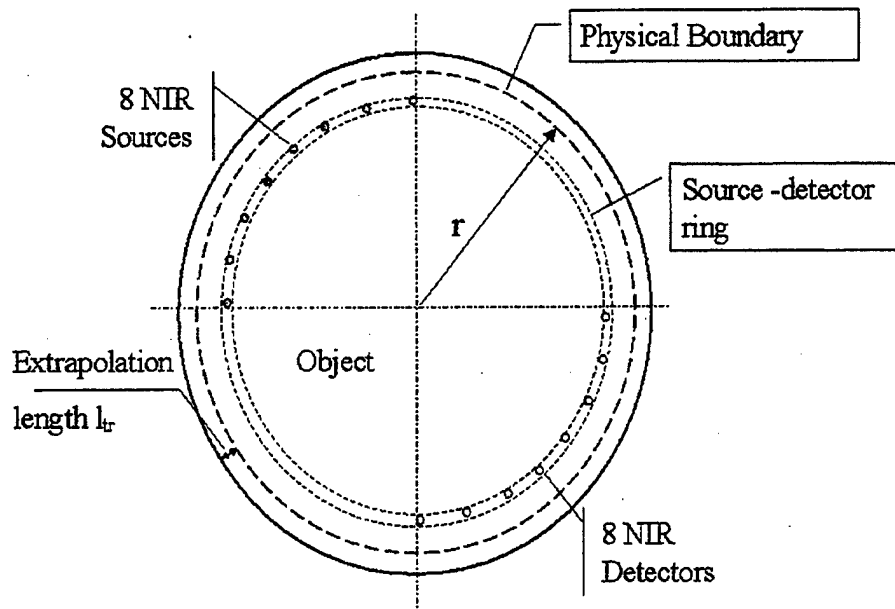
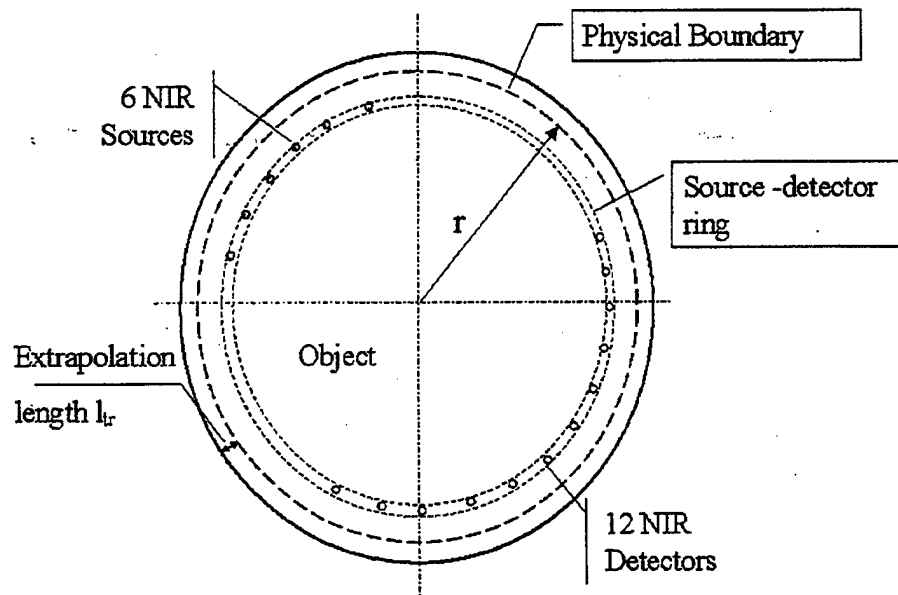


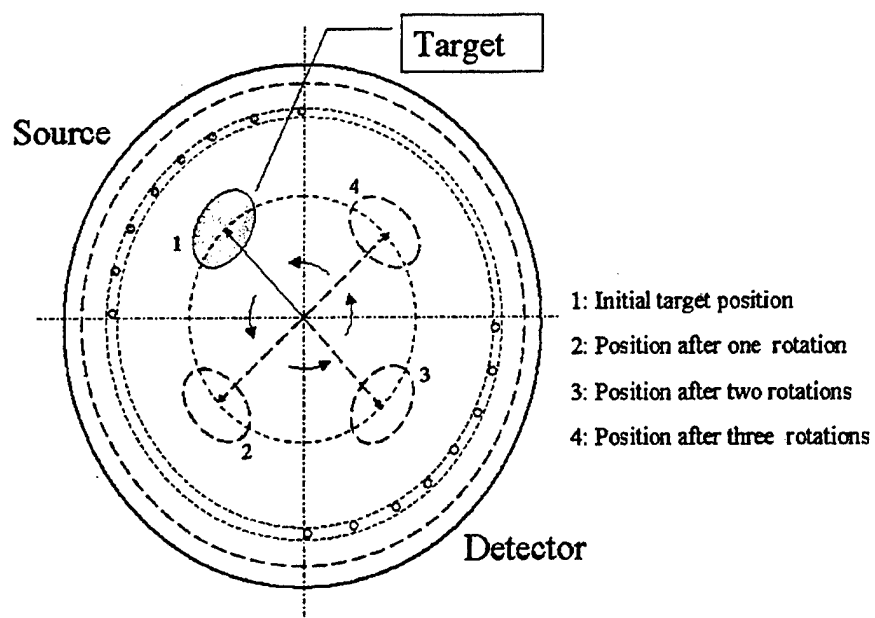
Figure 4.



(a)

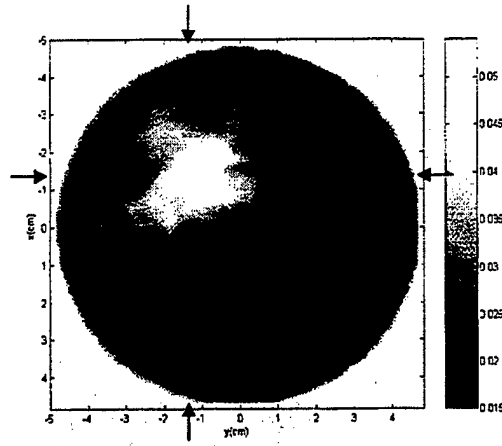


(b)

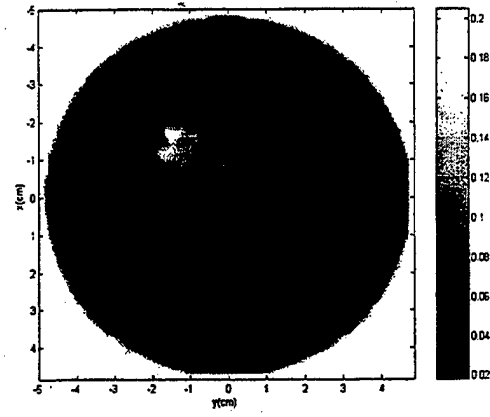


(c)

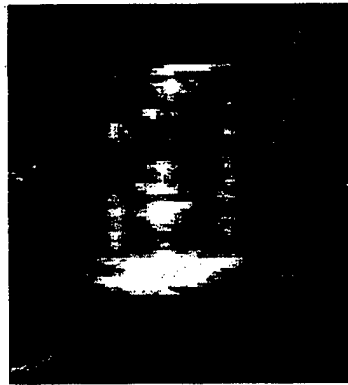
Figure 5.



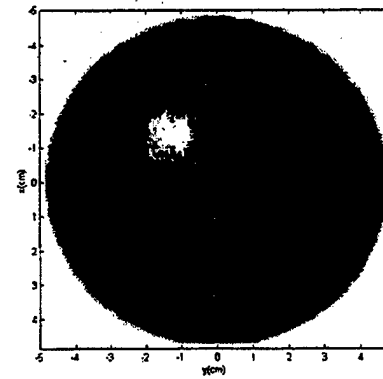
(a)



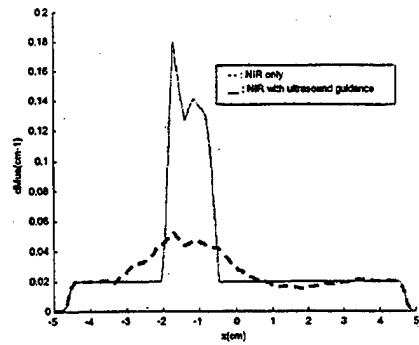
(b)



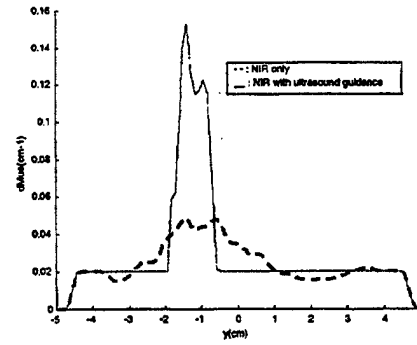
(c)



(d)



(e)



(f)

Figure 6.

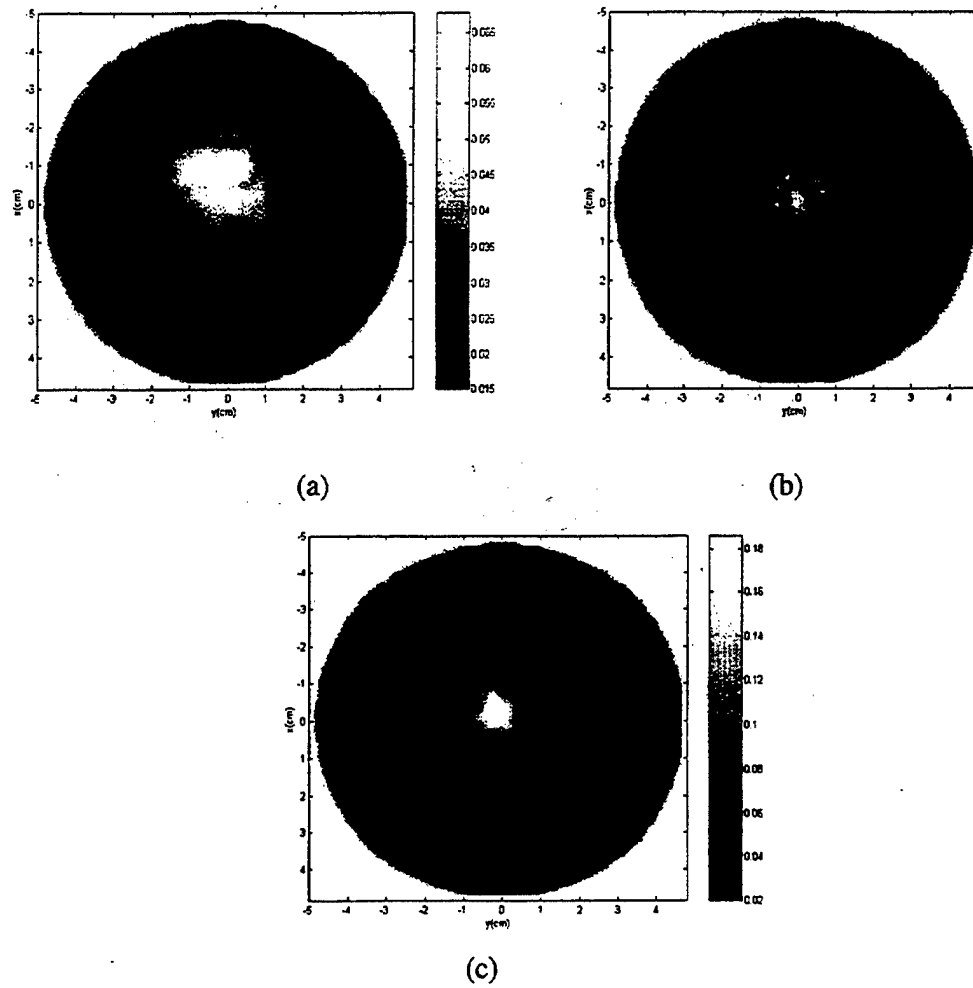


Figure 7.

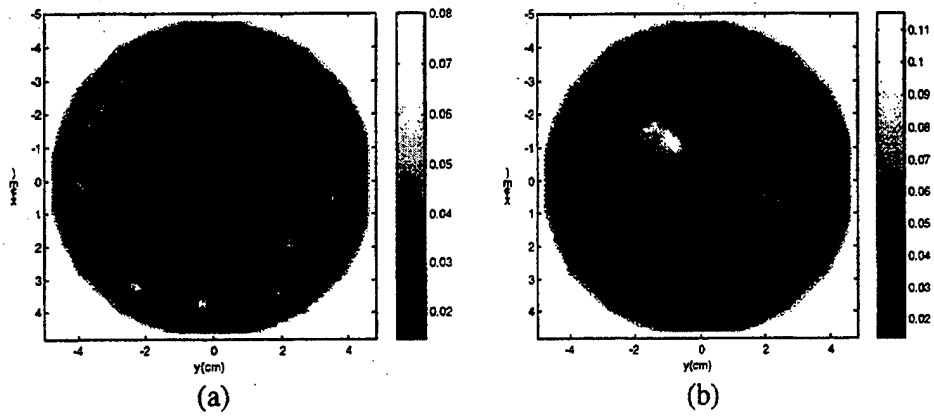


Figure 8.

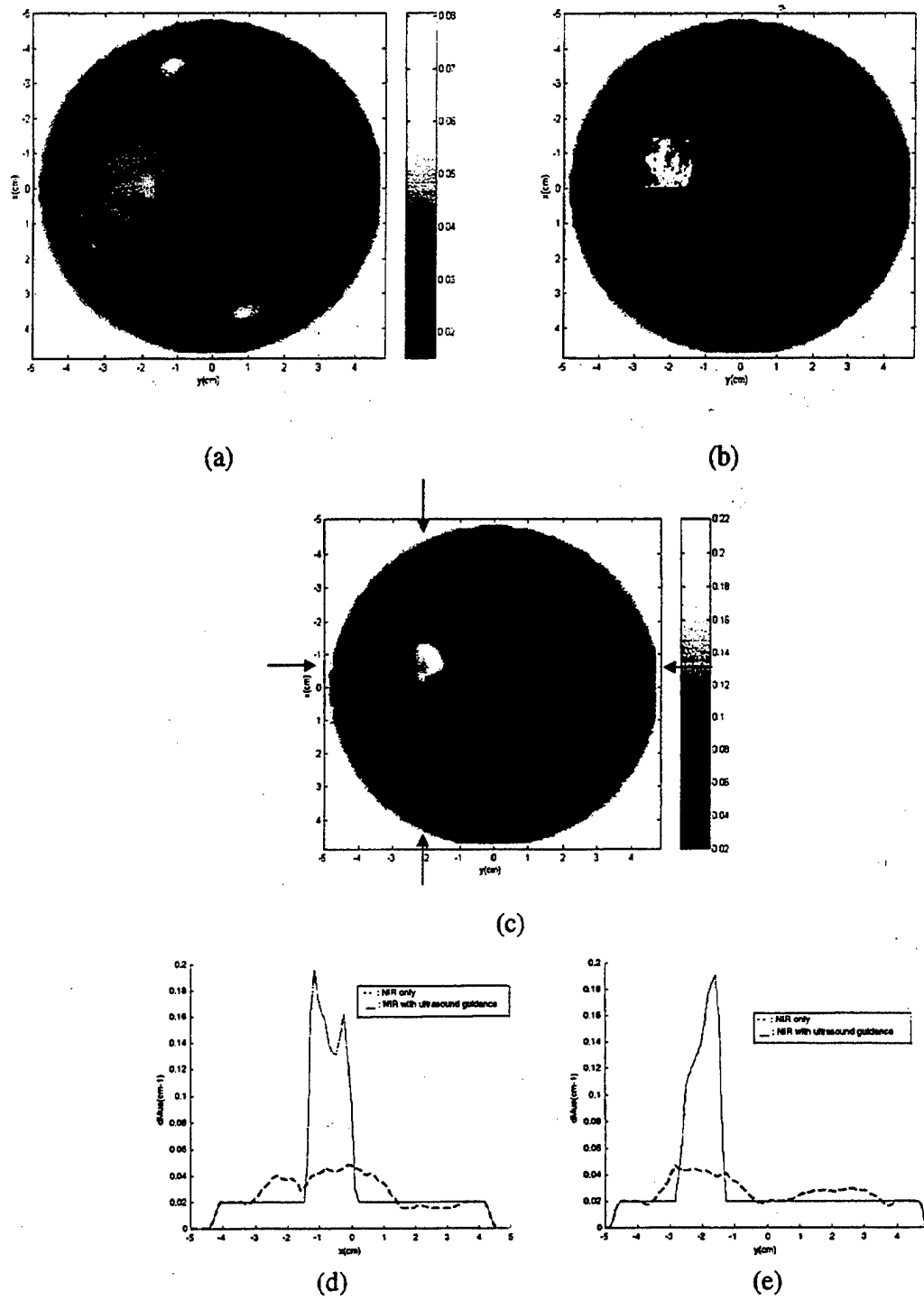


Figure 9.

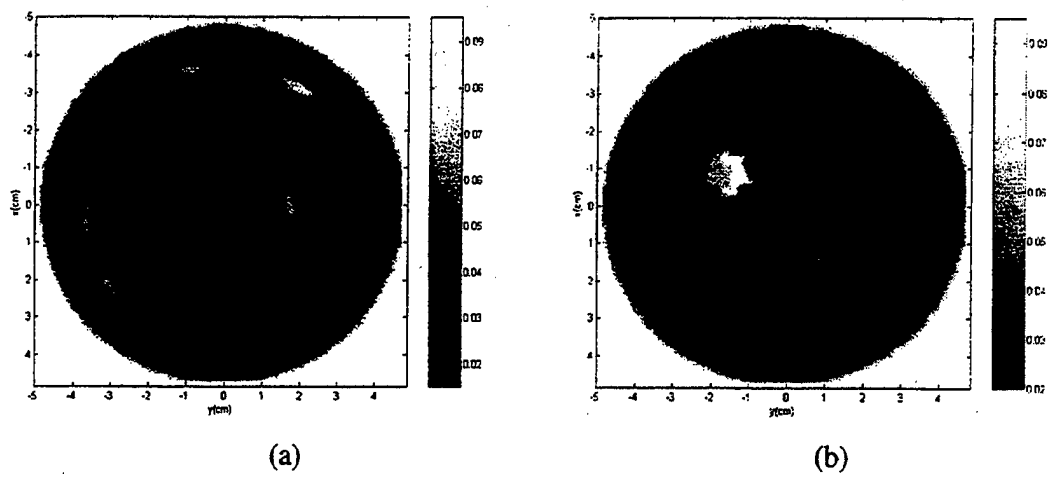


Figure 10.

**Imaging tumor angiogenesis using combined near infrared diffusive light and
ultrasound**

Quing Zhu, NanGuang Chen

Electrical and Computer Engineering Department, University of Connecticut, Storrs, CT 06269-
2157

Scott H. Kurtzman

University of Connecticut Health Center, Farmington, CT 06030

Correspondence:

Quing Zhu

<http://www.engr.uconn.edu/ece/faculty/zhu.html>

Tel: (860) 486-1815

Fax: (860) 486-2447

e-mail: zhu@engr.uconn.edu

ECE Dept. U157

University of Connecticut

260 Glenbrook Rd.,

Storrs CT 06269

Abstract

In this letter, a novel two-step reconstruction scheme using a combined near infrared and ultrasound technique and its utility in imaging distributions of optical absorption and hemoglobin concentration of breast lesions is demonstrated. In the first-step image reconstruction, the entire tissue volume is segmented based on initial co-registered ultrasound measurements, into lesion region and background region. Reconstruction is performed by using a finer grid for lesion region and a coarse grid for the background tissue. As results, the total number of voxels with unknown absorption can be maintained on the same order of total measurements and the matrix with unknown total absorption distribution is appropriately scaled for inversion. In the second-step, image reconstruction is refined by optimizing lesion parameters measured from ultrasound images. It is shown in this letter that detailed distributions of wavelength-dependent absorption and hemoglobin concentration of breast carcinoma can be obtained with the new reconstruction scheme.

OCIS codes: 170.0170, 170.3010, 170.5270, 170.7170, 170.3830

Tumor blood volume and micro-vascular density are parameters anatomically and functionally associated with tumor angiogenesis. If a single wavelength is used, optical absorption related to angiogenesis and other normal blood vessels can be measured. If two or more optical wavelengths are used, oxy-hemoglobin and deoxy-hemoglobin concentrations can be measured simultaneously and total hemoglobin concentration can be quantitatively estimated. During the last decade, modeling of the light propagation in the near infrared (NIR) region, combined with the advancements of light source and detectors, has improved the diffused light measurements and made possible the application of tomographic techniques for characterizing and imaging tumor angiogenesis.¹⁻³ However, the NIR technique has not been widely used in clinics and the fundamental problem remains the intense light scattering. As a result, diffusive light probes a widespread region instead of providing information along a straight line, and tomographic image reconstruction is, in general, underdetermined and ill-posed. We have demonstrated a combined imaging technique using *a priori* lesion structure information provided by co-registered ultrasound images to assist NIR imaging reconstruction in phantom studies.⁴⁻⁵ As a result, the NIR image reconstruction is well defined and less sensitive to noise. We have also demonstrated the feasibility of using NIR imaging as adjunct to ultrasound for breast cancer diagnosis.⁶ In this letter we report our novel two-step image reconstruction scheme using the combined approach and demonstrate its utility in imaging tumor absorption and hemoglobin distributions. It is shown that the detailed heterogeneous distributions of wavelength-dependent optical absorption and hemoglobin concentration of a breast carcinoma can be obtained. To the best of our knowledge, such detailed distributions have not been achieved by NIR only imaging reported in the literature.

A picture of our combined hand-held probe used in clinical studies is shown in Fig.1(a), and the probe dimensions and optical sensor distributions are shown in Fig. 1(b). The combined probe consists of a commercial ultrasound one-dimensional array located at the center of the probe and optical source and detector fibers distributed at the periphery and connected to a NIR imager. The NIR imager consists of 12 dual-wavelength source channels and 8 parallel receiving channels.⁵ On the transmission part, 12 pairs of dual wavelength (780nm and 830nm) laser diodes are amplitude modulated at 140 MHz. On the reception part, 8 photo multiplier tubes (PMTs) detect diffusely reflected light from the tissue. The sources and detectors are coupled to the probe through optical fibers. Both amplitude and phase at each source-detector pair are obtained and the resulting total number of measurements is $12 \times 8 \times 2 = 192$. The combined probe is made of a black plastic plate 10 cm in diameter, therefore, a semi-infinite boundary condition can be used for NIR measurement geometry. The measured amplitude and phase after calibration follow simple equations as

$$\begin{cases} \log(\rho_{\alpha\beta}^2 \hat{A}_{\alpha\beta}) = -k_i \rho_{\alpha\beta} + C_1 \\ \hat{\phi}_{\alpha\beta} = k_r \rho_{\alpha\beta} + C_2 \end{cases} \quad (1)$$

where amplitude $\hat{A}_{\alpha\beta}$ and phase $\hat{\phi}_{\alpha\beta}$ are associated with source channel α and detector channel β , $\rho_{\alpha\beta}$ is the corresponding source-detector separation, k is the wavenumber given by $k = \frac{-\mu_a + j\omega/v}{D} = k_i + jk_r$, D is the diffusion coefficient given by $D = 1/(3\mu'_s)$, ω and v are modulation frequency and speed of light, and C_1 and C_2 are constants. By fitting the amplitude and phase measured from the normal side of the breast we can obtain k_r and k_i and calculate background as

$$\bar{\mu}_a = -\bar{D}(k_r^2 - k_i^2), \bar{\mu}'_s = 1/(3\bar{D}) \text{ with } \bar{D} = \omega/(2vk_r k_i) \quad (2)$$

PAGES (3), (4)
ARE
MISSING
IN
ORIGINAL
DOCUMENT

In our two-step image reconstruction, we first segment tissue volume into two regions L and B, which contains a lesion as measured from co-registered ultrasound images and background tissue, respectively. We use Born approximation to relate the scattered field $U'_{sc}(r_{si}, r_{di}, \omega)$ measured at the source-detector pair i to absorption variations $\Delta\mu_a(r')$ in each volume element of two regions within the sample

$$U'_{sc}(r_{si}, r_{di}, \omega) = -\frac{1}{D} \left(\int_L G(r', r_{di}) U_{inc}(r', r_{si}) \Delta\mu_a(r') d^3r' + \int_B G(r', r_{di}) U_{inc}(r', r_{si}) \Delta\mu_a(r') d^3r' \right) \quad (3)$$

where $U_{inc}(r', r_{si}, \omega)$ and $G(r', r_{di}, \omega)$ are incident wave and green function of semi-infinite geometry, respectively. r_{si} and r_{di} are source and detector positions. We then discretize the lesion volume and background volume with different voxel size (a finer grid for lesion volume and a coarse grid for background). The scattered field can then be approximated as

$$U'_{sc}(r_{si}, r_{di}, \omega) \approx -\frac{1}{D} \left(\sum_{Lj} G(r_{vj}, r_{di}) U_{inc}(r_{vj}, r_{si}) \int_j \Delta\mu_a(r') d^3r' + \sum_{Bk} G(r_{vk}, r_{di}) U_{inc}(r_{vk}, r_{si}) \int_k \Delta\mu_a(r') d^3r' \right) \quad (4)$$

where $G(r_{vj}, r_{di}) U_{inc}(r_{vj}, r_{si})$ and $G(r_{vk}, r_{di}) U_{inc}(r_{vk}, r_{si})$ are weight values at the center r_{vj} of voxel j and center r_{vk} of voxel k in lesion volume L and background volume B, respectively.

The matrix form of equation (4) is given as

$$[U_{sd}]_{M \times 1} = [W_L, W_B]_{M \times N} [M_L, M_B]^T \quad (5)$$

where $W_L = [-\frac{1}{D} G(r_{vj}, r_{di}) U_{inc}(r_{vj}, r_{si})]_{M \times N_L}$ and $W_B = [-\frac{1}{D} G(r_{vk}, r_{di}) U_{inc}(r_{vk}, r_{si})]_{M \times N_B}$ are weight matrixes for lesion volume and background volume, respectively;

$[M_L] = [\int_{L_L} \Delta\mu_a(r') d^3r', \dots, \int_{N_L} \Delta\mu_a(r') d^3r']$ and $[M_B] = [\int_{L_B} \Delta\mu_a(r') d^3r', \dots, \int_{N_B} \Delta\mu_a(r') d^3r']$ are

total absorption distributions of lesion volume and background volume, respectively.

Instead of reconstructing $\Delta\mu_a$ distribution directly as the standard Born approximation, we reconstruct total absorption distribution M and then divide the total by different voxel sizes of lesion and background tissue to obtain $\Delta\mu_a$ distribution. By choosing a finer grid for lesion and a coarse grid for background tissue, we can maintain the total number of voxels with unknown absorption on the same scale of the total measurements. As a result, the inverse problem is less underdetermined and ill-posed. In addition, since the lesion absorption coefficient is higher than that of background tissue, in general, the total absorption of the lesion over a smaller voxel is on the same scale of total absorption of the background over a bigger voxel, therefore the matrix $[M_L, M_B]$ is appropriately scaled for inversion. The reconstruction is formulated as least square problem of minimizing object function $\min \|U_{sd} - W_L M_L^T - W_B M_B^T\|$. The unknown distribution M can be iteratively calculated using conjugate gradient search method.

The lesion location and volume obtained from co-registered ultrasound images are estimated as follows. Since the commercial 1-D ultrasound probe we used acquires 2-D ultrasound images in y - z plane (z is the propagation direction) and the 2-D NIR probe provides 3-D images, the co-registration is limited to an interception plane. However, if we approximate a lesion as an ellipsoid, we are able to estimate its radii from two orthogonal ultrasound images and therefore to obtain its volume. The 3-D lesion center is approximated by first obtaining a 2-D lesion center from a 2-D ultrasound image and then perturbing the 2-D center in the other orthogonal spatial direction in the second step reconstruction discussed below in an attempt to find out the best estimate of the center coordinate in that direction. Another source of error in estimating the

lesion geometry is the inaccuracy in radius measurements because lesion boundaries may not be well defined in ultrasound images. In addition, the target volumes seen by different modalities may be different because of different contrast mechanisms. In the second step, we refine image reconstruction by perturbing the center $c_0 = (x_0, y_0, z_0)$ and then the radii $r_0 = (r_x, r_y, r_z)$ and choosing the optimal set of parameters (c_{opt}, r_{opt}) . The final refined reconstruction is formulated as

$$\min \left\| U_{sd} - W_L(c_{opt}, r_{opt}) M_L^T(c_{opt}, r_{opt}) - W_B(c_{opt}, r_{opt}) M_L^T(c_{opt}, r_{opt}) \right\|^2 \quad (6)$$

Conjugate gradient method is used to search for global minimum. Since the total absorption matrix M is appropriately scaled, the iterative search converges quickly in two to three iterations. Two criteria were used for choosing (c_{opt}, r_{opt}) . First, the initial radii measured from co-registered ultrasound were fixed and optimal center c_{opt} was chosen which produced maximum total absorption energy inside the lesion. Second, the optimal center was used, and radii were increased or decreased to obtain optimal radii, which produced maximum total absorption energy inside the lesion.

Clinical studies were performed at the Health Center of the University of Connecticut and the human subject protocol was approved by Health Center IRB committee. Patients with palpable and non-palpable masses that were visible on clinical US were used as subjects. These subjects were scanned with the combined probe, and ultrasound images and optical measurements were acquired at multiple locations including the lesion region scanned at two orthogonal positions, a

normal region of the same breast scanned at two orthogonal positions (if the breast is large) and a normal region of the contralateral breast scanned at two orthogonal positions.

An example is given in this letter to demonstrate the use of our reconstruction scheme. Figure 2 (a) shows a gray scale ultrasound image of a palpable lump of a 44-year-old woman. The lesion was located at 6 to 8 o'clock position of the left breast at approximately 1.5 cm depth. Ultrasound showed an irregular poorly defined hypoechoic mass and the lesion was considered as highly suspicious for malignancy. An ultrasound guided core needle biopsy was recommended. Biopsy results revealed that the lesion was a high grade in-situ ductal carcinoma with necrosis.

Multiple optical measurements at two orthogonal positions were simultaneously made with ultrasound images at the lesion location as well as at approximately the same location of the contralateral normal breast. The fitted average tissue background measured at normal side of the breast at both wavelengths were $\bar{\mu}_a^{-780} = 0.03 \text{ cm}^{-1}$, $\bar{\mu}_a^{-830} = 0.05 \text{ cm}^{-1}$, $\bar{\mu}_s^{-780} = 9.22 \text{ cm}^{-1}$, $\bar{\mu}_s^{-830} = 7.61 \text{ cm}^{-1}$. The perturbations for both wavelengths used to calculate absorption maps

were normalized as $U'_{sc}(r_{si}, r_{di}, \omega) = \frac{U_L(r_{si}, r_{di}, \omega) - U_N(r_{si}, r_{di}, \omega)}{U_N(r_{si}, r_{di}, \omega)} U_B(r_{si}, r_{di}, \omega)$, where

$U_L(r_{si}, r_{di}, \omega)$ and $U_N(r_{si}, r_{di}, \omega)$ were measurements obtained at lesion region and contralateral normal region, and $U_B(r_{si}, r_{di}, \omega)$ was calculated incident field using fitted background $\bar{\mu}_a$ and $\bar{D} = 1/3\bar{\mu}_s$. This procedure cancels unknown system gains associated with different sources and detectors as well as electronic channels. The initial estimate of lesion center and diameters from

ultrasound images were (0, 0.39 cm, 1.7 cm) and 3.44 cm x 4.38cm x 1.76 cm, respectively. A finer grid of 0.5 x 0.5 x 0.5 (cm³) and a coarse grid of 1.5 x 1.5 x 1.0 (cm³) were chosen for the lesion and background tissue, respectively. The total reconstruction volume was chosen to be 9 x 9 x 4 cm³ and the total voxels with unknown optical absorption was 190, which was on the same order of 192 total measurements. The image reconstruction was performed using the NIR data simultaneously acquired with the ultrasound image shown in Fig.2 (a). The second step refined reconstruction revealed optimal lesion centers at approximately (-1.1 cm, 0.3 cm, 1.7 cm) for 780 nm and (-0.9 cm, -0.7 cm, 1.7 cm) for 830 nm, respectively, and optimal diameters of 4.28 cm x 5.18 cm x 1.96 cm. The detailed absorption maps with high absorption non-uniformly distributed around the lesion boundaries at both wavelengths are shown in Fig. 2 (b) and (c). By assuming that the major chromophores are oxygenated (oxyHb) and deoxygenated (deoxyHb) hemoglobin molecules in the wavelength range studied, we can estimate the distribution of total hemoglobin concentration as shown in Fig.2 (d). The extinction coefficients used for calculating oxyHb and deoxyHb concentrations were $\epsilon_{\text{Hb}}^{780}=2.544$, $\epsilon_{\text{HbO}_2}^{780}=1.695$, $\epsilon_{\text{Hb}}^{830}=1.797$, $\epsilon_{\text{HbO}_2}^{830}=2.419$ obtained in Ref. 7 in a natural logarithm scale with units of inverse millimoles times inverse centimeters. The measured average cancer and background total hemoglobin concentrations were 116.9 μ moles and 47.6 μ moles, respectively. These values agree with 3-D average measurements reported in Ref. 8.

It is interesting to note that the absorption distributions at both wavelengths as well as total hemoglobin concentration were distributed heterogeneously at the cancer periphery. To the best of our knowledge, such fine distributions have not been reported by using NIR only reconstruction techniques. However, this finding agrees with the published literature showing

that breast cancers have higher blood volumes than non-malignant tissue due to angiogenesis, especially at the cancer periphery.⁹ In addition, the carcinoma reported here had a necrotic core which could lead to low absorptions observed at both wavelengths in the center region. Ideally, pathologic report with blood vessel density count could be used to correlate the NIR findings reported here. Future plans are to obtain microvessel counts in the region of the tumor as well as surrounding, non-malignant breast tissue.

In summary, we have reported a two-step image reconstruction scheme and we demonstrate that aided with co-registered ultrasound, detailed optical absorption and total hemoglobin distributions of the breast carcinoma can be obtained. These distributions reveal tumor angiogenesis and provide valuable information for breast cancer diagnosis and treatment.

Ellen Oliver, the surgical nurse at the Cancer Center of the University of Connecticut Health Center, is greatly acknowledged for her help in patient recruiting and scheduling. Graduate students Minming Huang and Daqing Piao are acknowledged for their help on clinical data acquisition and machining work of the combined probe. The authors would like to thank the following for their funding support: the State of Connecticut (99CT21) and DOD ARMY Breast Cancer Program (DAMD17-00-1-0217, DAMD17-01-1-0216).

References:

- [1] B. Tromberg, N. shah, R. Lanning, A. Cerussi, J. Espinoza, T. Pham, L. Svaasand and J. Butler, Neoplasia vol.2, No 1:2, pp26-40, 2000.
- [2] B. Pogue, S. P. Poplack, T. O. McBride T. O., W. A. Wells, K. S. Osterman, U. Osterberg, and K. D. Paulsen, Radiology, 218: 261-266 (2001).
- [3] V. Ntziachristos, A.G.Yodh, M. Schnall and B. Chance, PNAS vol. 97 (6), 2267-2772 ,2000
- [4] Zhu, Q., Durduran, T., Holboke, M., Ntziachristos, V. and Yodh, A, Optics Letters, (24) No.15, Aug. 1, 1999.
- [5] Chen, NG, Guo, PY, Yan, SK, Piao DQ, and Zhu, Q., Applied Optics, December, Vol.40, No.34, 6367-6380, 2001.
- [6] Zhu, Q. Conant E. and Chance, B, Journal of Biomedical Optics 5(2): 229-236, 2000.
- [7] Cope M, Ph.D Dissertation, University of College London, 1991.
- [8] Holboke, M, Tromberg B. J., Li, X., Fishkin N. Shah, Kidney D., Butler, J, Chance B, Yodh, A.G., Journal of Biomedical Optics 5(2), 237-247, 2000.
- [9] Vaupel P, Kallinowski F, Okunieff P., Cancer Research 49, 6449-6465, 1989

References:

- [1] B. Tromberg, N. Shah, R. Lanning, A. Cerussi, J. Espinoza, T. Pham, L. Svaasand and J. Butler, "Non-Invasive in vivo characterization of breast tumors using photon migration spectroscopy," *Neoplasia* vol.2, No 1:2, pp26-40, 2000.
- [2] B. Pogue, S. P. Poplack, T. O. McBride T. O., W. A. Wells, K. S. Osterman, U. Osterberg, and K. D. Paulsen, "Quantitative hemoglobin tomography with diffuse near-infrared spectroscopy: pilot results in the breast," *Radiology*, 218: 261-266 (2001).
- [3] V. Ntziachristos, A.G.Yodh, M. Schnall and B. Chance, "Concurrent MRI and diffuse optical tomography of breast after indocyanine green enhancement, *PNAS* vol. 97 (6), 2267-2772, 2000
- [4] Zhu, Q., Durduran, T., Holboke, M., Ntziachristos, V. and Yodh, A., "Imager that combines near infrared diffusive light and ultrasound," *Optics Letters*, (24) No.15, Aug. 1, 1999.
- [5] Chen, NG, Guo, PY, Yan, SK, Piao DQ, and Zhu, Q., "Simultaneous near infrared diffusive light and ultrasound imaging," *Applied Optics*, December, Vol.40, No.34, 6367-6380, 2001.
- [6] Zhu, Q., Conant E. and Chance, B, "Optical imaging as an adjunct to sonograph in differentiating benign from malignant breast lesions," *Journal of Biomedical Optics* 5(2): 229-236, 2000.
- [7] Cope M, Ph.D Dissertation, University of College London, 1991.
- [8] Holboke, M, Tromberg B. J., Li, X., Fishkin N. Shah, Kidney D., Butler, J, Chance B, Yodh, A.G., "Three-dimensional diffuse optical mammography with ultrasound location in human subject," *Journal of Biomedical Optics* 5(2), 237-247, 2000.

[9] Vaupel P, Kallinowski F, Okunieff P., "Blood flow, oxygen and nutrient supply, and metabolic microenvironment of human tumors: a review," *Cancer Research* 49, 6449-6465,

1989

Figure Captions:

Fig. 1. (a) Picture of a hand-held combined probe and a frequency domain NIR imager. (b) Sensor distribution of the combined probe. The diameter of the combined probe is 10 cm. Smaller circles are optical source fibers and big circles are detector fibers. A commercial ultrasound probe is located at the center and its dimensions are 5.6 cm by 1 cm.

Fig. 2. (a) A gray scale ultrasound image of a palpable lump of a 44-year-old woman. Ultrasound showed an irregular poorly defined hypoechoic mass and the lesion was considered as highly suspicious for malignancy. Reconstructed optical absorption maps at 780 nm (b) and 830 nm (c). Vertical color bars are absorption coefficient in the unit of cm^{-1} . (d) is the total hemoglobin concentration map. The vertical color bars are μmoles . The NIR data were simultaneously acquired with ultrasound image shown in Fig.2 (a). Each image consists of 7 slices obtained in 0.5 cm spacing from 0.5 cm to 3.5 cm in depth. The vertical and horizontal axes correspond to x and y dimensions of 9 cm by 9 cm.

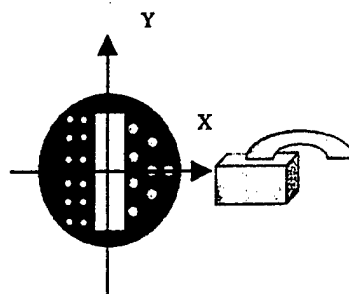
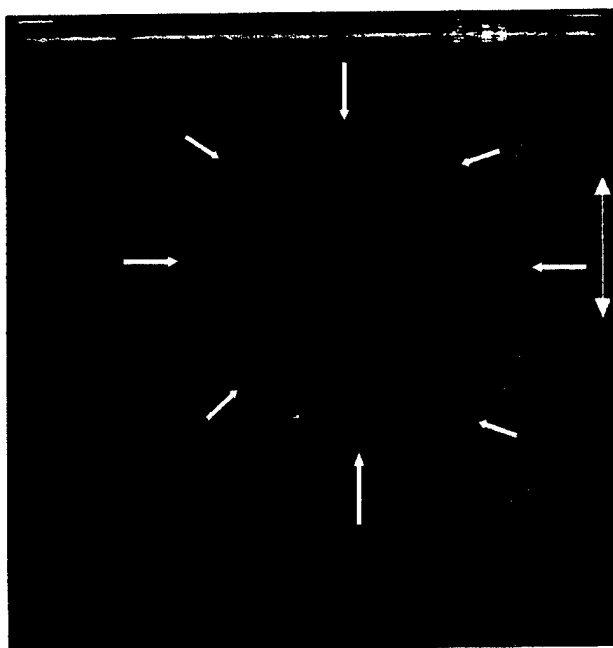
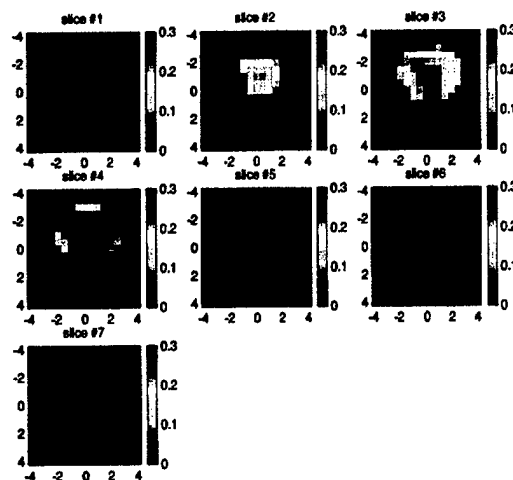


Fig.1.

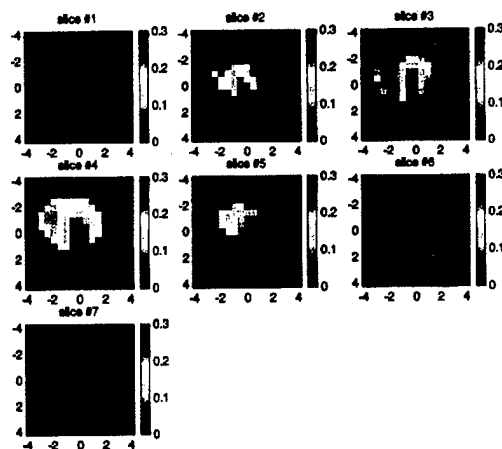
Zhu et al.



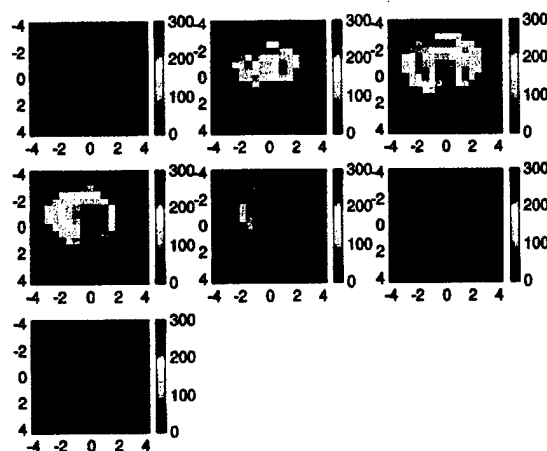
(a)



(b)



(c)



(d)

Fig. 2. (a) A gray scale ultrasound image of a palpable lump of a 44-year-old woman. Ultrasound showed an irregular poorly defined hypoechoic mass and the lesion was considered as highly suspicious for malignancy. Reconstructed optical absorption maps at 780 nm (b) and 830 nm (c). Vertical color bars are absorption coefficient in the unit of cm^{-1} . (d) is the total hemoglobin concentration map. The vertical color bars are μmoles . The NIR data were simultaneously acquired with ultrasound image shown in Fig.2 (a). Each image consists of 7 slices obtained in 0.5 cm spacing from 0.5 cm to 3.5 cm in depth. The vertical and horizontal axes correspond to x and y dimensions of 9 cm by 9 cm.

Characterization of small absorbers inside turbid media

Nan Guang Chen and Quing Zhu

Department of Electrical & Computer Engineering, University of Connecticut, Storrs, Connecticut 06269

Received October 29, 2001

We propose a novel noniterative near-infrared diffusive image reconstruction method that uses minimal *a priori* co-registered ultrasound information. Small absorbing targets embedded in a homogeneous background are described approximately in terms of their monopole, dipole, and quadrupole moments. With an approximate estimation of the center locations of these absorbers from ultrasound images, we show in simulations that the reconstruction accuracy of the absorption coefficient exceeds 80% if the noise level is less than 0.2%. We also demonstrate experimentally that the accuracy can be improved by use of additional ultrasound volume information even for a noise level as high as 1.5%. © 2002 Optical Society of America

OCIS codes: 100.3190, 170.3010, 170.3880, 290.1990.

Functional imaging with near-infrared (NIR) light has found potential applications in many areas, such as breast and brain lesion detection and diagnosis.^{1,2} Recently, a combination of NIR imaging with other imaging modalities, such as ultrasound or magnetic resonance imaging, has shown promising results^{3–5} in providing complementary contrasts and overcoming NIR reconstruction problems related to intensive light scattering.

In this Letter we introduce a novel reconstruction algorithm for NIR diffusive imaging that uses approximate target center locations estimated from co-registered ultrasound. Our new method is based on estimation of major characteristics of isolated small absorbers. These characteristics are monopole, dipole, and quadrupole moments. Higher-order moments have negligible effects in characterizing the absorbers and are ignored. It is shown in this Letter that measurements of diffusive photon density waves cannot readily achieve a signal-to-noise ratio that is good enough for reconstructing the detailed shape information of targets. However, the quadrupole moment can provide an approximate extension of the target, which is necessary for distributing the integral absorption (the monopole) to an appropriate target region. In situations in which the measurement system suffers from unexpected noise, accurate estimation of the quadrupole moment might not be possible. The target volume estimated from co-registered ultrasound images can be used for distributing the integral absorption inside the target volume. We have conducted a series of simulations at different noise levels to evaluate the performance of this new method. We have also conducted experiments using our combined NIR-ultrasound imager⁵ to test the algorithm.

If it is assumed that there are only a few small inhomogeneous targets embedded in a homogeneous background, the distribution of the absorption coefficient can be expressed as

$$\mu_a(\mathbf{r}) = \mu_a^0 + \Delta\mu_a(\mathbf{r}). \quad (1)$$

The background absorption coefficient, μ_a^0 , can be as small as 0.02 cm^{-1} for normal breast tissues, whereas $\Delta\mu_a$ can be well beyond 0.1 cm^{-1} for tumors because of the blood. In the Born approximation, the photon

density wave is decomposed into an incident wave and a scattering wave:

$$\Phi(\omega, \mathbf{r}) = \Phi_{\text{inc}}(\omega, \mathbf{r}) + \Phi_{\text{sct}}(\omega, \mathbf{r}). \quad (2)$$

The incident wave is the solution of a homogeneous diffusion equation, and the scattering wave can be given approximately by the linear perturbation theory:

$$\Phi_{\text{sct}}(\omega, \mathbf{r}) \approx - \int_V \frac{\Delta\mu_a(\mathbf{r}')}{D} \Phi_{\text{inc}}(\omega, \mathbf{r}') G(\mathbf{r}, \mathbf{r}') d^3\mathbf{r}'. \quad (3)$$

In this equation, $G(\mathbf{r}, \mathbf{r}')$ is the Green's function, and $D = 1/3\mu_s'$ is inversely proportional to the reduced scattering coefficient, μ_s' . In the context of early stage breast cancer detection, we can further assume that those heterogeneities are confined to a few isolated regions. Then, the scattering wave can be expanded around each of N target centers as

$$\begin{aligned} \Phi_{\text{sct}}(\omega, \mathbf{r}) = & - \frac{1}{D} \sum_{\nu=1}^N [M^\nu W(\mathbf{r}_0^\nu) + \mathbf{D}^\nu \cdot \nabla W(\mathbf{r}_0^\nu) \\ & + \mathbf{Q}^\nu \cdot \nabla \nabla W(\mathbf{r}_0^\nu)/2 + O(a^3)]. \end{aligned} \quad (4)$$

Here \mathbf{r}_0^ν is the center of the ν th target, and $W(\mathbf{r}_0^\nu) = \Phi_{\text{inc}}(\omega, \mathbf{r}_0^\nu) G(\mathbf{r}, \mathbf{r}_0^\nu)$ is the weight function. For the ν th target, M^ν , \mathbf{D}^ν , and \mathbf{Q}^ν are its monopole, dipole, and quadrupole moments, respectively. Terms beyond the second order of target dimension a have negligible effects in characterizing the absorbers and are neglected in our model. For the ν th target, its monopole, dipole, and quadrupole moments are scalar, vector, and second-order tensor, respectively, and they are given as

$$\begin{aligned} M^\nu &= \int_{V_\nu} \Delta\mu_a(\mathbf{r}') d^3\mathbf{r}', & \mathbf{D}^\nu &= \int_{V_\nu} \Delta\mu_a(\mathbf{r}') \mathbf{r}' d^3\mathbf{r}', \\ \mathbf{Q}^\nu &= \int_{V_\nu} \Delta\mu_a(\mathbf{r}') \mathbf{r}' \mathbf{r}' d^3\mathbf{r}'. \end{aligned} \quad (5)$$

The integrations are over a small isolated region V_ν .

A multiple-source, multiple-detector configuration is typical for frequency-domain diffusive imaging systems. We are using 12 sources (780 nm) that are amplitude modulated at 140 MHz and eight detectors

in our simulations as well as in the experiments. These sources and detectors are deployed on an absorbing plane, which simplifies boundary conditions. The reflection mode with a semi-infinite geometry is used for both simulation and experiment. The measured scattering wave is related to the target moments by the following equation:

$$[\hat{\phi}_1 \dots \hat{\phi}_m]^T \approx \Omega [M^1 \ D^1 \ Q^1 \ \dots \ Q^N]^T. \quad (6)$$

An element of Ω is either the weight function for one target or its derivatives up to the second order.

The inverse problem is to retrieve the characteristics of those embedded absorbers from measured photon density waves on the surface. Based on our simplified forward model, it is necessary to have certain information about absorbers, such as the number of targets and their center positions, in advance. The ultrasound system of our combined imager can provide such information. Once the initial center locations have been specified, the weight function, together with its first and second derivatives, can be calculated immediately. Since the inverse problem has only a few unknowns, reconstruction of target moments is overdetermined and least-squares solutions can be adopted. For each target, the monopole moment represents the integral absorption, the dipole moments result in correction of the center position, and the quadrupole moments lead to estimation of the target volume, in which the integral absorption can be redistributed. The target volume is estimated by simple matching of the quadrupole moments with those of an ellipsoid, which has the freedom to rotate about the center in any direction to any angle.

Figure 1 shows a schematic of the combined probe for experiments, which is a circular plate made of rigid absorbing material. One or two cuboid absorbers were placed 2.5 cm deep in a homogeneous medium. For phantom experiments, raw data were acquired with our combined imaging system. The ultrasound array was translated in the x direction to yield target volume estimates. We used 0.6% Intralipid as a homogeneous background, which yielded a reduced scattering coefficient of 6 cm^{-1} and an absorption coefficient of 0.015 cm^{-1} . The embedded targets were as scattering as the background but were more absorbing. For simulations, the simulated measurement data were the sum of forward model prediction and random noises ranging from 0.1% to 1% (with respect to the amplitudes of the incident waves). The optical properties of homogeneous media and targets are similar to those used in phantom experiments.

Shown in Fig. 2 are simulation results for a single target. The target was a cuboid of (1.2, 0.8, 1) cm in the x , y , and z directions, respectively, and was centered at (0.2, 0, 2.5) cm. The volume of the target was 0.96 cm^3 . The absorption coefficient above the background was 0.25 cm^{-1} . Here we provide the results for one dipole moment (D_x) and one quadrupole moment (Q_{xx}), but similar results were obtained for other components. The initial target position that was input into the reconstruction algorithm was (0,

0, 2.5) cm, which deviated slightly from the true position. This initial location error resulted in a negligible effect on the reconstructed monopole values, as shown in Fig. 2(a). The offset of center position can be corrected by the estimated dipole moment, D_x [see Fig. 2(c)], which is slightly lower than the true value. However, the inaccuracy of the initial center position obviously affects the reconstructed quadrupole moment. The circles in Fig. 2(e) represent values greater than the true values. After we correct the center position according to the estimated dipole moments, the reconstructed values of Q_{xx} , plotted as asterisks in the same figure, are much closer to the true values. Although the mean values of reconstructed moments are essentially independent of noise

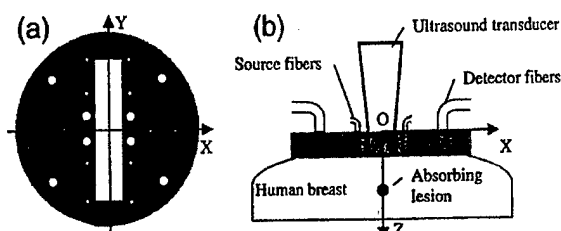


Fig. 1. (a) Bottom view of the combined probe. The central rectangular slot gives the ultrasound array access to tissues underneath the probe. The circular holes are used to hold optical fibers. The small holes are for light sources, and the larger ones are for detectors. The diameter of the probe is 10 cm. (b) Side view of the probe.

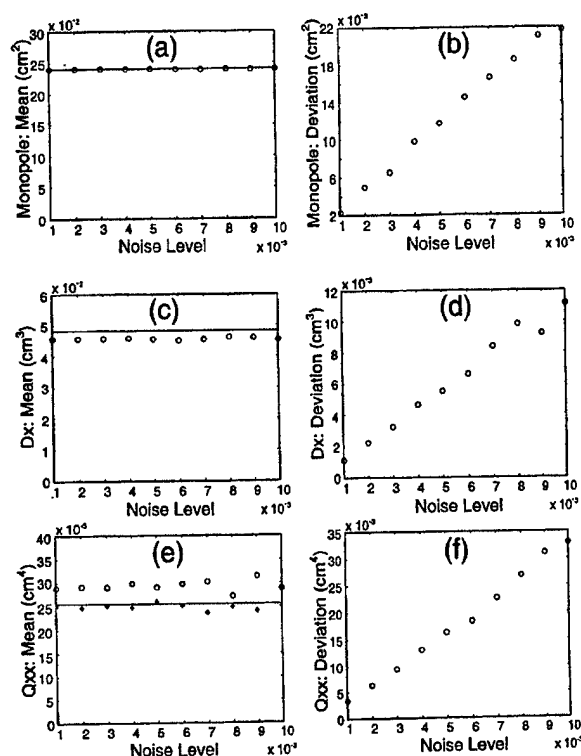


Fig. 2. Simulation results for a single target. (a), (c), and (e) mean values of monopole, dipole, and quadrupole moments, respectively. (b), (d), and (f) standard deviations of the corresponding quantities. The solid lines in (a), (c), and (e) are true values.

Table 1. Reconstructed Absorption Coefficients from Phantom Experiments^a

Value (cm ⁻¹)	Combination 1		Combination 2	
	Target 1	Target 2	Target 1	Target 2
True	0.065	0.065	0.102	0.065
Reconstructed	0.064 ± 0.028	0.064 ± 0.027	0.106 ± 0.026	0.064 ± 0.017

^aThe average values and standard deviations are estimated from six sets of experimental data.

level, the standard deviations of all moments increase linearly with increasing noise level. Higher-order moments suffer more from noise, as expected intuitively. For the quadrupole moments, as small as a 0.2% noise level could lead to a relative error of ~20%. This is the main reason that we did not attempt to reconstruct moments beyond the second order.

To test the capability of our algorithm to characterize multiple targets, we performed simulations with two absorbers of different absorption coefficients. The absorbers were the same size as the single target. One absorber was located at (-1.2, 0, 2.5) cm, with an absorption coefficient 0.25 cm⁻¹ beyond the background. The other absorber was located at (1.2, 0, 2.5) cm, with an absorption coefficient 0.1 cm⁻¹ beyond the background. The main effect of adding one target was that the relative error in the reconstructed monopole moments increased to ~2.5 times. Less of an effect on the dipole moments was observed, although an even more trivial difference for the quadrupole could be seen. It was also found that the noise-induced deviation was independent of target optical properties.

Our current NIR imaging system has a noise level near 1.5%. According to the simulation results, the system cannot readily retrieve the accurate quadrupole moments from measured photon density waves. Thus we have to use the volume information obtained from co-registered ultrasound images in target characterization. We used two geometrically identical targets that were approximately 1-cm³ cubes. They were gel phantoms made from 0.6% Intralipid solution, ink, and ultrasound scatterers. The boundaries of these targets can clearly be seen in ultrasound images, and target centers and volumes can be estimated accurately. For example, a 1.07-cm³ target was measured as 1.05 cm³ by ultrasound. For co-registered NIR imaging, two different combinations of targets were adopted. The first was a pair of equally absorbing cubes with an absorption coefficient of 0.065 cm⁻¹. The second was a pair of absorbing cubes with absorption coefficients of 0.065 and 0.1 cm⁻¹, respectively. We simply distribute the estimated monopole evenly over the target volume. So the reconstructed absorption coefficient was an average value within each target. The true and the reconstructed values are compared in Table 1. The mean values and standard deviations were based on six sets of measurements.

Since target monopole moments can be estimated with sufficient accuracy, the reconstructed absorption coefficient depends more on the estimation of target volume, which can be obtained from the reconstructed quadrupole moment or co-registered ultrasound images. It is possible that the extent of the optical volume of a lesion is larger than the volume esti-

mated from the acoustic images. This is one of our motivations for estimating the optical volume from the quadrupole moments. Further improvements are needed for an accurate estimate of quadrupole moments. In the moment-based method we assume that the lesions are isolated and are embedded in a homogeneous background. This assumption is quite true for more-homogeneous fatty breasts and may not hold for dense breasts that consist of both glandular tissue and fat. In the latter case, we could segment ultrasound images, identify tissue types, and estimate background optical properties of different tissues in the reconstruction as well. Both acoustic and optical contrasts exist in tumors but the sensitivities of these two modalities may be different. Therefore, the correlation between acoustic and optical heterogeneities remains unknown at the current stage and will be determined in our future clinical studies.

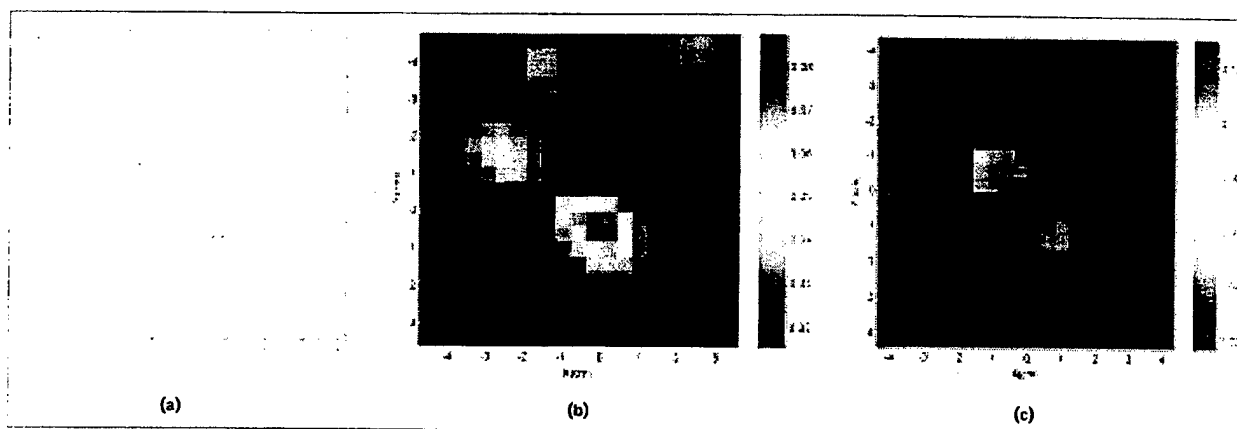
In comparison with current sophisticated NIR image reconstruction algorithms, our method is very simple in terms of computation. Once an ultrasound image has been taken and targets have been identified, it is possible to monitor the local change of absorption continuously and in real time. Averaging over a large number of samples will help suppress the effect of random noise.

In this Letter an algorithm for characterizing absorbers has been demonstrated. Theoretically, a similar algorithm is possible for characterizing scattering targets as well. However, since the weights of monopole, dipole, and quadrupole moments of scattering targets are related to spatial derivatives, which are two order higher than those of absorbers, the quadrupole moments will be even harder to reconstruct.

We thank the following for their funding support: the State of Connecticut (99CT21) and the U.S. Department of Defense Army Breast Cancer Program (DAMD17-00-1-0217, DAMD17-01-1-0216). N. G. Chen's e-mail address is chenng@engr.uconn.edu.

References

1. B. Tromberg, N. Shah, R. Lanning, A. Cerussi, J. Espinoza, T. Pham, L. Svaasand, and J. Butler, *Neoplasia* **2**, 26 (2000).
2. R. M. Danen, Y. Wang, X. D. Li, W. S. Thayer, and A. G. Yodh, *Photochem Photobiol.* **67**, 33 (1998).
3. B. Pogue and K. Paulsen, *Opt. Lett.* **23**, 1716 (1998).
4. Q. Zhu, N. G. Chen, D. Q. Piao, P. Y. Guo, and X. H. Ding, *Appl. Opt.* **40**, 3288 (2001).
5. N. G. Chen, P. Y. Guo, S. K. Yan, D. Q. Piao, and Q. Zhu, *Appl. Opt.* **40**, 6367 (2001).



Near Infrared Diffusive Light Imaging with Ultrasound Localization

Quing Zhu, Nan Guang Chen, Puyun Guo, Shikui Yan, and Daqing Piao

Functional imaging with near infrared (NIR) diffusive light has found potential applications in many areas. Although huge efforts have been made to bring this technique to a clinically acceptable stage, intense light scattering remains a fundamental problem. Subsequently, diffusive light continues to probe a widespread region instead of providing information along a straight line. Multiple measurements are always correlated as a result of overlapping probed regions. Therefore, increasing the total number of measurements does not necessarily provide more independent information for image reconstruction. Image reconstruction is generally affected by many factors, including system signal to noise ratio, probe configuration, and regulation schemes used in the imaging algorithms.

We have constructed a novel combined imager suitable for simultaneous NIR diffusive light and ultrasound imaging and co-registration.^{1,2} The imager consists of a two-dimensional (2D) ultrasound array deployed at the center of a hand-held probe. Twelve dual wavelength laser source fibers and eight optical detector fibers are deployed at the periphery of the probe. The combined imaging uses target locations and shapes provided by co-registered ultrasound images to localize the NIR imaging reconstruction. As a result, the NIR image reconstruction is well defined. Since the convergence can be achieved within a small number of iterations, the NIR image reconstruction is less sensitive to noise.

In experiments where co-registered ultrasound provided the target depth information, the reconstructed optical absorption coefficient accuracy has been improved by 15% for high contrast agents and 30% for low contrast agents³ (AQ:1). The speed of reconstruction has been improved by ten times on average. In experiments where the three-dimensional (3D) target distributions were provided by co-registered ultrasound, the optical image reconstruction converges very fast and needs only one iteration to reconstruct accurate optical absorption coefficient.² This result is very encouraging because there is no known robust stopping criterion to terminate iterative image reconstruction algorithms. No further iterations are needed with the *a priori* knowledge from co-registered ultrasound.

Figure 1 shows an example of ultrasound assisted NIR image reconstruction.² Figure 1(a) shows the contours of ultrasound image of two targets of 1 cm in size. Figure 1(b) is the NIR image of the two targets. The target pointed by the white arrow in part (b) is displaced from its true location by about 1 cm and the reconstructed absorption coefficient is only 50% of the true value. With the ultrasound localization shown in part (a), the NIR image shown in Fig. 1(c) provides correction target locations and the reconstructed absorption coefficients are within 20% of the true values. By adding optical contrasts to ultrasonically detected lesions, the combined approach has great promise in improving breast cancer diagnosis.⁴ Optical contrasts will significantly improve diagnostic ultrasound in differentiating benign from malignant solid lesions.

References

1. Q. Zhu, T. Dunrana, M. Holboke, V. Ntziachristos, and A. Yodh, *Opt. Lett.*, **24**, 1050-2 (1999).

Figure 1. (a) Contours of the ultrasound image of two low optical contrast targets (absorption coefficients are 0.1 cm⁻¹) embedded 2.5 cm deep in the intralipid of 0.5% concentration. (b) NIR image of the two targets without ultrasound localization. One target (pointed by the white arrow) is only 50% of the true value and is displaced from its true location by 1 cm. Two image artifacts appear at the top edge of the image. (c) NIR image assisted by ultrasound localization. The targets appear at correct location and the reconstructed optical absorption coefficients are within 20% of the true value.

2. N.G. Chen, P.Y. Guo, S.K. Yan, D.Q. Piao, and Q. Zhu, "Simultaneous near infrared diffusive light and ultrasound imaging," *Appl. Opt.* In press.
3. Q. Zhu, N.G. Chen, D.Q. Piao, P.Y. Guo, and X.H. Ding, *Appl. Opt.* **40**, 3288-303 (2001).
4. Q. Zhu, E. Conant, and B. Chance, *Journal of Biomedical Optics* **5**, 229-36 (2000).

Quing Zhu, Nan Guang Chen, Puyun Guo, Shikui Yan, and Daqing Piao, Electrical and Computer Engineering Department University of Connecticut, Storrs, CT.

Author Queries

1. Edit OK?

Simultaneous near-infrared diffusive light and ultrasound imaging

Nan Guang Chen, Puyun Guo, Shikui Yan, Daqing Piao, and Quing Zhu

We have constructed a near-real-time combined imager suitable for simultaneous ultrasound and near-infrared diffusive light imaging and coregistration. The imager consists of a combined hand-held probe and the associated electronics for data acquisition. A two-dimensional ultrasound array is deployed at the center of the combined probe, and 12 dual-wavelength laser source fibers (780 and 830 nm) and 8 optical detector fibers are deployed at the periphery. We have experimentally evaluated the effects of missing optical sources in the middle of the combined probe on the accuracy of the reconstructed optical absorption coefficient and assessed the improvements of a reconstructed absorption coefficient with the guidance of the coregistered ultrasound. The results have shown that, when the central ultrasound array area is in the neighborhood of $2\text{ cm} \times 2\text{ cm}$, which corresponds to the size of most commercial ultrasound transducers, the optical imaging is not affected. The results have also shown that the iterative inversion algorithm converges quickly with the guidance of *a priori* three-dimensional target distribution, and only one iteration is needed to reconstruct an accurate optical absorption coefficient.

© 2001 Optical Society of America

OCIS codes: 170.0170, 170.3010, 170.5270, 170.7170, 170.3830.

1. Introduction

Ultrasound is used extensively for differentiation of cysts from solid lesions in breast examinations, and it is routinely used in conjunction with mammography. Ultrasound can detect breast lesions a few millimeters in size.¹ However, its specificity in breast cancer diagnosis is not considered to be high enough as a result of overlapping characteristics of benign and malignant lesions.^{2,3} Optical imaging based on diffusive near-infrared (NIR) light has the great potential to differentiate tumors from normal breast tissues through determination of tissue parameters, such as blood volume, blood O_2 saturation, tissue light scattering, water concentration, and the concentration and lifetime of exogenous contrast agents.⁴⁻¹² As a potential diagnostic tool, however, NIR diffusive light imaging suffers from low spatial resolution and lesion location uncertainties because of intense light scattering in tissue.

Most NIR imaging reconstruction algorithms are based on tomographic inversion techniques.¹³⁻²⁰ Reconstruction of tissue optical properties in general is underdetermined and ill-posed because the total number of unknown optical properties always exceeds the number of measurements, and the perturbations produced by the heterogeneities are much smaller than the background signals. In addition, the inversion reconstruction algorithms are sensitive to measurement noise and model errors.

Our group and others have introduced a novel hybrid imaging method that combines the complementary features of ultrasound and NIR diffusive light imaging.²¹⁻²⁵ The hybrid imaging obtains coregistered ultrasound and NIR diffusive light images through simultaneous deployment of an ultrasound array and NIR source-detector fibers on the same probe.^{21,22,24} Coregistration permits joint evaluation of acoustic and optical properties of breast lesions and enables use of lesion morphology provided by high-resolution ultrasound to improve the lesion optical property estimate. With the *a priori* knowledge of lesion location and shape provided by coregistered ultrasound, NIR imaging reconstruction can be localized within specified three-dimensional (3-D) regions. As a result, the reconstruction is overdetermined because the total number of unknown optical properties is reduced significantly. In addition, the reconstruction is less sensitive to noise because the

The authors are with the Department of Electrical and Computer Engineering, University of Connecticut, Storrs, Connecticut 06269. N. G. Chen's e-mail address is chenng@engr.uconn.edu, and Q. Zhu's e-mail address is zhu@engr.uconn.edu.

Received 27 November 2000; revised manuscript received 24 July 2001.

0003-6935/01/346367-14\$15.00/0

© 2001 Optical Society of America

convergence can be achieved with a small number of iterations.

The clinical use of the combined diagnosis relies on the coregistration of both ultrasound and NIR sensors at the probe level. Conventional ultrasound pulse-echo imaging requires that an imaging transducer be located on top of the target, whereas NIR diffusive light imaging is feasible when the optical source and detector fibers are distributed at the periphery of the ultrasound transducer. However, the effects of missing optical sources in the middle of the combined probe on the accuracy of the reconstructed optical properties have to be evaluated. In addition, the improvements of reconstructed optical properties with the guidance of the coregistered ultrasound need to be quantitatively assessed. Furthermore, real-time data acquisition is necessary to avoid errors in coregistration caused by patient motion during the clinical experiments. In this paper we report our experimental results on the optimal probe configuration, and we quantify the improvements on reconstructed optical properties using a combined probe. We also demonstrate simultaneous combined imaging with a near-real-time imager.

2. Near-Infrared Diffusive Wave Imaging

We used the Born approximation to relate the scattered field $U_{sc}'(\mathbf{r}, \omega)$ measured at the probe surface to absorption variations in each volume element within the sample. In the Born approximation, the scattered wave originated from a source at \mathbf{r}_{si} and measured at \mathbf{r}_{di} it can be related to the medium absorption heterogeneity $\Delta\mu_a(\mathbf{r}_{vj})$ at \mathbf{r}_{vj} by

$$[U_{sd}]_{MX1} = [W]_{MXN} \{\Delta\mu_a\}_{NX1} \quad (1)$$

where M is the total number of source-detector pairs, N is the total number of imaging voxels, and $W_{ij} = G(\mathbf{r}_{vj}, \mathbf{r}_{di}, \omega) U_{inc}(\mathbf{r}_{vj}, \mathbf{r}_{si}, \omega) \nu \Delta \mathbf{r}_{vj}^3 / \bar{D}$ is the weight matrix given in Ref. 19. $G(\mathbf{r}_{vj}, \mathbf{r}_{di}, \omega)$ and $U_{inc}(\mathbf{r}_{vj}, \mathbf{r}_{si}, \omega)$ are a Green's function and incident wave, respectively. ω is the modulation frequency and \bar{D} is the average or background diffusion coefficient, which is the average value over the background or whole tissue.

With M measurements obtained from all possible source-detector pairs in the planar array, we can solve N unknowns of μ_a by inverting the above matrix equation. In general, the perturbation Eq. (1) is underdetermined ($M < N$) and ill-posed.

NIR imaging by itself generally has poor depth discrimination. However, ultrasound is excellent in providing accurate target depth. Once the target depth is available from coregistered ultrasound, we can set $\Delta\mu_a$ of a nontarget depth equal to zero. This implies that all the measured perturbations originate from the particular depth that contains the target. Because the number of unknowns is reduced significantly, the reconstruction converges very fast. In Ref. 23 we reported that, with *a priori* target depth provided by ultrasound, the accuracy of the reconstructed μ_a has been improved by 15–30% on aver-

age, and the speed of reconstruction has been improved by an order of magnitude. In this paper we furthermore demonstrate that, with the 3-D target distribution provided by coregistered ultrasound, the accuracy of reconstructed μ_a and the reconstruction speed can be further improved.

To solve the unknown optical properties of Eq. (1), we used the total least-squares (TLS) method^{26,27} to iteratively invert Eq. (1). The TLS method performs better than other least-squares when the measurement data are subject to noise and the linear operator W contains errors. We found that the TLS method provides more accurate reconstructed optical properties than other least-squares methods, and we adopted TLS in solving inverse problems. It has been shown in Ref. 28 that the TLS minimization is equivalent to the following minimization problem:

$$\min \frac{\|U_{sd} - WX\|^2}{\|X\|^2 + 1}, \quad (2)$$

where X represents unknown optical properties. The conjugate gradient technique was employed to iteratively solve Eq. (2).

3. Methods

A. Combined Probe and Imaging Geometry

There are four basic requirements to guide the design of the combined probe. First, reflection geometry is preferred because a conventional ultrasound scan is performed with this geometry. Second, an ultrasound array needs to occupy the center of the combined probe for coherent imaging. Third, NIR sources and detectors have to be distributed at the periphery. Because photon propagation distribution exhibits a banana shape, imaging of the tissue volume underneath the probe is feasible even through there are no sources and detectors deployed in the central portion of the probe. Fourth, the minimum source-detector separation should be larger than 1 cm for the diffusion approximation to be valid, and the maximum separation should be ~8–9 cm to effectively probe depths of 3–4 cm.

On the basis of these requirements we deployed 12 dual-wavelength optical source fibers and 8 detector fibers over a 9 cm × 9 cm probe area (see Fig. 1). The minimum and maximum source-detector separations in the configuration are 1.4 and 8 cm, respectively. To study the effect of the central optical hole on the accuracy of the reconstructed optical properties, we compared the reconstruction results with an extra center source and without the center source. The configuration without the center source corresponds to a 2 cm × 2 cm hole area. We further moved the noncenter 12 sources and 8 detectors toward periphery by leaving a 3 cm × 3 cm hole area in the middle. Figure 2 shows the picture of a combined probe with the 3 cm × 3 cm central area occupied by an ultrasound array. The ultrasound array consists of 64 elements made of 1.5-mm-diameter piezoelectric transducers (Valpey Fisher Inc). The

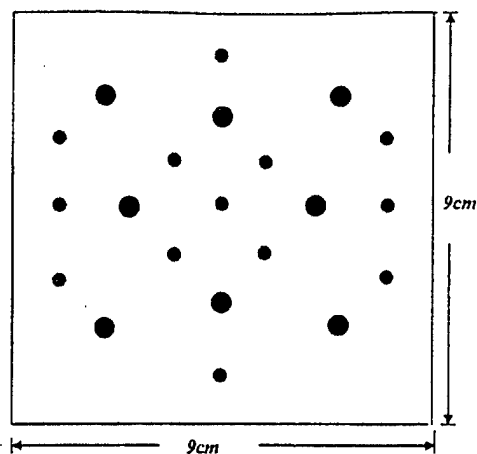


Fig. 1. Schematic arrangement of NIR source and detector fibers on the probe. Small solid circles are the source fibers and larger solid cycles are the detector fibers.

transducers are deployed in a rectangular matrix with 4-mm spacing in both x and y directions. The center frequency of the transducer is 6 MHz and the bandwidth is 40%. The transducers are made from the same piece of piezoelectric transducer material. Therefore the gain difference among different transducers is less than 3 dB. The 12 dual-wavelength optical laser diode sources (760 and 830 nm) and 8 photomultiplier tube (PMT) detectors are coupled to the probe through optical fibers, which are deployed at the periphery of the two-dimensional (2-D) ultrasound array. This hybrid array deployment compromises ultrasound coherent imaging and NIR diffusive light imaging characteristics.

The $9\text{ cm} \times 9\text{ cm} \times 4\text{ cm}$ image volume underneath the probe is discretized into voxels of size $0.4\text{ cm} \times 0.4\text{ cm} \times 1\text{ cm}$. There is a trade-off between the accurate estimation of the weight matrix W and the voxel

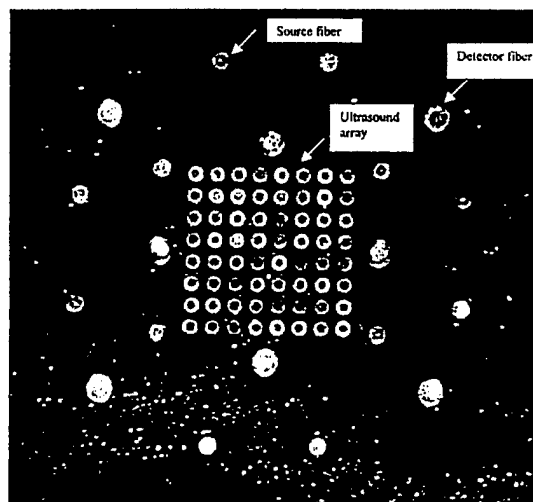


Fig. 2. Picture of an experimental probe. An ultrasound array of $8 \times 8 = 64$ transducers occupies the central $3 \text{ cm} \times 3 \text{ cm}$ area, and 12 dual-wavelength source fibers and 8 detector fibers are deployed at the periphery.

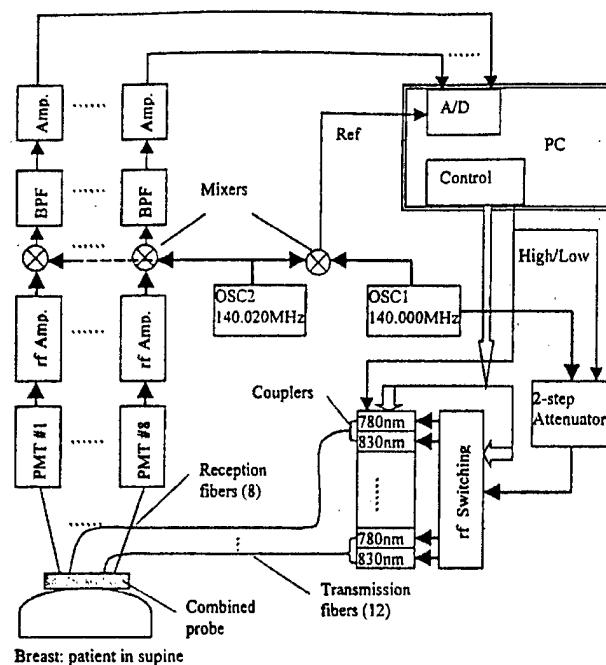


Fig. 3. Schematic of the NIR frequency-domain imaging system. The modulation frequency is 140 MHz. The 12 dual-wavelength source channels are switched on sequentially by a PC, and 8 detector channels receive signals in parallel. BPF, bandpass filter; OSC, oscillator.

size. Because W_{ij} is a discrete approximation of the integral

$$\int G(\mathbf{r}_v, \mathbf{r}_d, \omega) U_{\text{inc}}(\mathbf{r}_v, \mathbf{r}_s, \omega) \frac{v}{D} d\mathbf{r}_v^3,$$

it is more accurate when the voxel size is smaller. However, the total number of reconstructed unknowns will increase dramatically with the decreasing voxel size. Furthermore, the rank of W does not increase in the same order as the total number of voxels when the voxel size decreases. This suggests that neighboring W_{ij} 's are correlated when the voxel size is smaller, and a further decrease in voxel size will not add more independent information to the weight matrix. We found that a $0.4 \text{ cm} \times 0.4 \text{ cm} \times 1 \text{ cm}$ voxel size is a good compromise. Therefore we used this voxel size in image reconstructions reported in this paper.

B. Experimental Systems

1. Near-Infrared Imaging System

We constructed a NIR frequency-domain imaging system. The block diagram of the system is shown in Fig. 3. This system has 12 dual-wavelength source channels and 8 parallel receiving channels. On the transmission part, 12 pairs of dual-wavelength (780 and 830 nm) laser diodes are used as light sources, and their outputs are amplitude modulated at 140.000 MHz. Each one of the 12 optical combiners (OZ Optics Inc.) looks like a Y adapter, guiding the emission of two diodes of different wave-

lengths through the same thin optical fiber (approximately 0.2 mm in diameter). To reduce noise and interference, an individual driving circuit is built for each diode. As a laser diode works in series, a control board that interprets instructions from a PC is used to coordinate operations of associated components. When a single transmission channel is selected, it turns on the corresponding driving circuit so that a dc driving current can be set up for the diode. At the same time, a selected signal is sent to a rf switching unit, which distributes a rf signal to the right channel to modulate the optical output. On the reception part, eight PMTs are employed to detect diffusely reflected light from turbid media. Each PMT is housed in a sealed aluminum box, shielding both environment lights and electromagnetic fields, and an optical fiber (3 mm in diameter) couples NIR light from the detection point to the reception window of the PMT. The electrical signal converted from the optical input is generally weak and rather high in frequency, so high-gain amplification and frequency transform are necessary before it can be sampled by an analog-to-digital (A/D) board inside the PC. We built eight parallel heterodyne amplification channels to measure the response of all detectors simultaneously, which reduces the data-acquisition time. Each amplification channel consists of a rf amplifier (40 dB), a mixer in which the rf signal (OSC1, 140.000 MHz) is mixed with a local oscillator (OSC2, 140.020 MHz), a bandpass filter centered at 20 kHz, and a low-frequency amplifier of 30 dB. The heterodyned two-stage amplification scheme helps suppress wide-band noises efficiently. We also generated a reference signal of 20 kHz by directly mixing OSC1 and OSC2, which is necessary for retrieving phase shifts. Eight detection signals and one reference are sampled, converted, and acquired into the PC simultaneously, in which the Hilbert transform is used to compute the amplitude and phase of each channel. The entire data acquisition takes less than 1 min, which is fast enough to acquire data from patients.

One of the challenges encountered in the design of a NIR imaging system is the huge dynamic range of signals received at various source-detector distances. For example, for a semi-infinite phantom made of 0.5% Intralipid solution, the amplitude measured at 1 cm away from a source is approximately 5000 times larger than that at 8-cm separation. In addition, the perturbation that is due to an embedded heterogeneity with optical properties similar to a tumor is normally a few percent of the background signal. As a result, a reflection-mode NIR imaging system should have at least a 120-dB dynamic range to probe a target up to 4 cm in depth. It is hard to build amplifiers that work linearly over such a wide dynamic range. We overcome this difficulty by implementing two-level source outputs. The dc output of a laser diode is controlled when its feedback loop is adjusted, whereas the rf signal is switched simultaneously by a two-step attenuator (no attenuation or 30-dB attenuation). When the source and detector are close to each other, the source is controlled to

yield a low-level output. When the separation becomes larger, a 30-dB higher output level should be used. With this two-level source scheme, our system achieved fairly good linearity over a wide range of source-detector separations (from 1.5 to 8 cm).

Because the parameters of an individual laser diode or a PMT vary considerably from one to another, we have to calibrate the gain and phase shift for each channel. A set of measurements obtained from all source-detector pairs placed on the boundary of a homogeneous medium is

$$\bar{A}_{\alpha\beta}, \bar{\phi}_{\alpha\beta}, \quad \alpha = 1, 2, \dots, m; \quad \beta = 1, 2, \dots, n.$$

Here, amplitude $\bar{A}_{\alpha\beta}$ and phase $\bar{\phi}_{\alpha\beta}$ are related to source α and detector β , and m and n are the total number of sources and detectors, respectively. From the diffusion theory, we can obtain the following set of equations⁷:

$$\bar{A}_{\alpha\beta} = I_s(\alpha)I_d(\beta) \frac{\exp(-k_i\rho_{\alpha\beta})}{\rho_{\alpha\beta}^2},$$

$$\bar{\phi}_{\alpha\beta} = \varphi_s(\alpha) + \varphi_d(\beta) + k_r\rho_{\alpha\beta},$$

in which $I_s(\alpha)$ and $\varphi_s(\alpha)$ are the relative gain and phase delay associated with source channel α , $I_d(\beta)$ and $\varphi_d(\beta)$ are similar quantities associated with detector channel β , $\rho_{\alpha\beta}$ is the corresponding separation, and $k_r + jk_i$ is the complex wave number. We obtain the following set of linear equations by taking a logarithm of the above equations related to amplitude:

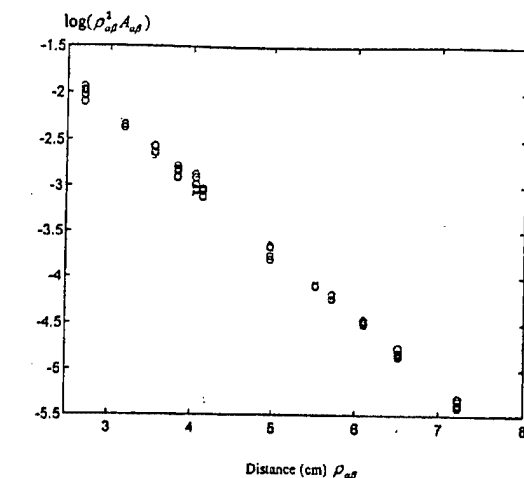
$$\log(\rho_{\alpha\beta}^2 \bar{A}_{\alpha\beta}) = \log[I_s(\alpha)] + \log[I_d(\beta)] - k_i\rho_{\alpha\beta},$$

$$\bar{\phi}_{\alpha\beta} = \varphi_s(\alpha) + \varphi_d(\beta) + k_r\rho_{\alpha\beta}. \quad (3)$$

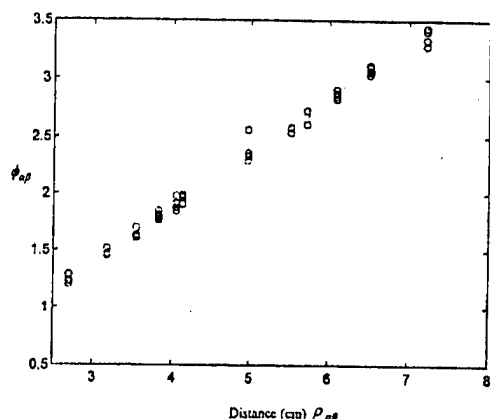
Although the optical properties of the calibration medium are known in advance, we leave the wave number as a variable and use fitted k_r and k_i to calculate the background scattering and absorption coefficients. We verified our calibration method by comparing the best fitted k 's with real values. The results of our using 0.5–0.8% Intralipid solutions always yielded scattering and absorption coefficients with a rather good accuracy. With the two unknown wave numbers included, the total number of unknowns is $2(m + n + 2)$, which is generally far smaller than the number of measurements $m \times n$. Consequently, Eq. (3) is overdetermined. We can solve all $I_s(\alpha)$, $I_d(\beta)$, $\varphi_s(\alpha)$, and $\varphi_d(\beta)$ terms as well as two unknown wave numbers in a least-squares sense. Then all measurements can be calibrated accordingly. The results of amplitude $A_{\alpha\beta} = \exp(-k_i\rho_{\alpha\beta})/\rho_{\alpha\beta}^2$ and phase $\phi_{\alpha\beta} = k_r\rho_{\alpha\beta}$ after calibration are shown in Fig. 4. As one can see, the calibrated amplitude ($\log \rho_{\alpha\beta}^2 A_{\alpha\beta}$) and the phase from various source-detector pairs change linearly with distance.

2. Ultrasound System

The ultrasound system diagram is shown in Fig. 5, and the system consists of 64 parallel transmission and receiving channels. Each transmission circuit can generate a high-voltage pulse of 200-ns duration (6 MHz) with 125 V peak to peak to the connected



(a)



(b)

Fig. 4. (a) $\log(p_{\alpha\beta}^2 A_{\alpha\beta})$ versus distance $p_{\alpha\beta}$ after calibration. (b) Phase $\phi_{\alpha\beta}$ versus distance $p_{\alpha\beta}$ after calibration.

transducer. Each receiving circuit has two-stage amplifiers followed by an A/D converter with 40-MHz sampling frequency. The amplifier gain can be controlled based on the target strength. A group of transmission channels can be addressed simultaneously to transmit pulses from neighbor transducers with specified delays and therefore to focus the transmission beam. The returned signals can be received simultaneously by a group of transducers, and the signals can be summed with specified delays to form a receiving beam.

The data-acquisition procedure is the following. The first 9-element neighbor subarray (dashed rectangle in Fig. 6) from the 64-element transducer array and the corresponding channels are chosen, and then the transmission delay profiles are generated in the computer according to the prespecified focal depth. The delay profile data are transferred to the 64-channel delay profile generator, which triggers the 64 high-voltage pulser profiles as well as the receiving channels. The returned ultrasound signals are amplified

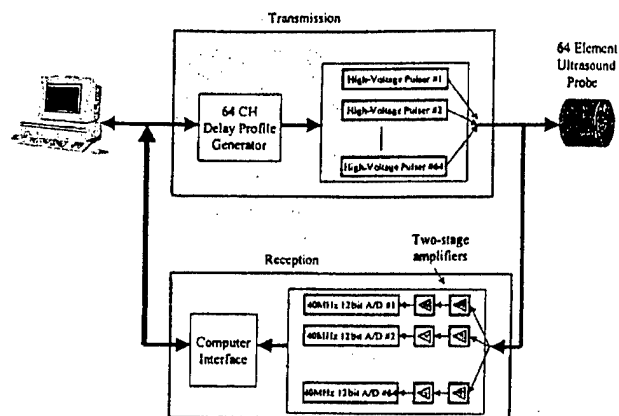


Fig. 5. Schematic of our ultrasound scanner. We connected 64 ultrasound transducers to 64 parallel transmission and reception channels. The transmission part consists of 64 high-voltage pulsers, which can be controlled by computer-generated delay profiles. The reception part consists of 64 two-stage amplifiers and A/D converters. CH, channel.

by two-stage amplifiers and sampled by A/D converters. The data are buffered in the memories and are read by the computer after the entire data acquisition is completed. The second subarray (solid rectangle in Fig. 6) is chosen and the same data-acquisition process is repeated. A total of 64 subarrays is used in the data acquisition. After the 64-subarray data acquisition is completed, the data stored in the memories are read by the computer for image formation. The entire data acquisition and imaging display are performed in approximately 5 s, which is fast enough for clinical experiments. To ensure good signal-to-noise ratio, we perform all the electronics using printed circuit boards.

Figure 7 shows the picture of the entire system and the combined probe. Both the NIR system (top) and the ultrasound system (bottom) are mounted on a hospital cart. The combined probe, which houses the ultrasound array and the NIR source-detector fibers, is designed to be hand held to scan patients.

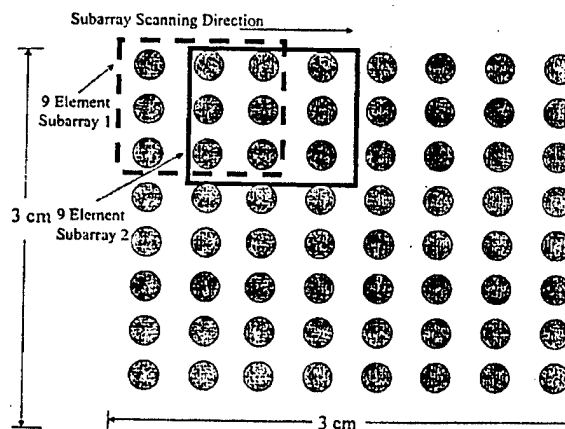


Fig. 6. Ultrasound subarray scanning configuration.

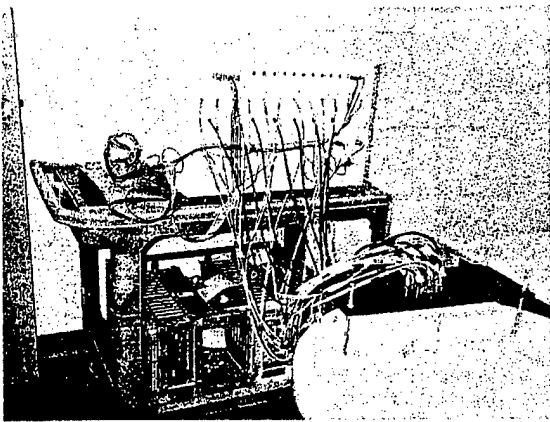


Fig. 7. Picture of our combined system. NIR system (top) and ultrasound system (bottom) are mounted on a hospital cart.

C. Phantoms

We used 0.5–0.6% Intralipid solutions to mimic normal human breast tissues in all experiments, and the corresponding reduced scattering coefficient μ_s' ranges from 5 to 6 cm^{-1} . The Intralipid is contained in a large fish tank to set up approximately a semi-infinite homogeneous phantom. Small semispherical balls (1 cm in diameter), made of acrylamide gel,²² are inserted into Intralipid to emulate lesions embedded in a breast. The reduced scattering coefficients of the gel phantoms are similar to that of the background medium ($\mu_s' \approx 6 \text{ cm}^{-1}$), and we changed the absorption coefficients to different values by adding different concentrations of India ink to emulate high-contrast ($\mu_a = 0.25 \text{ cm}^{-1}$) and low-contrast ($\mu_a = 0.1 \text{ cm}^{-1}$) lesions. Ultrasound scattering particles of 200 μm in diameter are added to the gel phantom before the gel is formed.

4. Experimental Results

A. Effects of Missing Optical Sources in the Combined Probe

A series of experiments was conducted to estimate the optimal hole size. Three probe configurations were investigated: (a) no-hole, (b) 2 cm \times 2 cm central hole, and (c) 3 cm \times 3 cm hole probes. The no-hole probe was essentially the same as case (b) except that an additional light source was added in the middle. Figure 8 shows reconstructed NIR images for on-center targets of high ($\mu_a = 0.25 \text{ cm}^{-1}$, left column) and low contrast ($\mu_a = 0.1 \text{ cm}^{-1}$, right column) located 2.5 cm deep inside the Intralipid. The fitted background μ_a and μ_s are 0.015 and 5.36 cm^{-1} , respectively. With the target depth provided by ultrasound, we performed reconstruction in the target layer. The centers of the voxels in this layer were (x , y , 2.5 cm), where x and y were discrete spatial x - y coordinates, and the thickness of the layer was 1 cm. For the high-contrast target case, there are no important differences in image quality associated with different probes [Figs. 8(a) and 8(c)] except that with a 3 cm \times 3 cm hole. The first row of Table 1 provides

measured maximum μ_a values from the corresponding images. Because of the low spatial resolution of diffusive imaging, the boundaries of the targets are not well defined. The maximum value is a better estimation of reconstructed target μ_a . From no hole to 2 cm \times 2 cm, the reconstructed maximum μ_a decreases slowly. But for 3 cm \times 3 cm, the maximum μ_a drops suddenly to 0.104 cm^{-1} , which is less than half of the original value. Another imaging parameter we measured is the full width at half-maximum (FWHM) of the corresponding images. Because the image lobes were elliptical in general, we measured the widths of longer and shorter axes and used the geometric mean to estimate the FWHM. The results are shown in Table 1, and the FWHM almost increases with the hole size. We also measured the image artifact level, which was defined as the ratio of the peak artifact to the maximum strength of the image lobe and is given in decibels. The results are shown in Table 1. No artifacts were observed in the images of no-hole and 2 cm \times 2 cm hole probes. However, the peak artifact level at the -14.3-dB level was measured in the image of the 3 cm \times 3 cm hole probe. When the contrast was low, the reconstructed maximum absorption coefficients and measured FWHMs were essentially the same for the no-hole and 2 cm \times 2 cm hole probes. However, the reconstructed maximum value dropped to 60% of the true value for the 3 cm \times 3 cm probe. The artifact levels measured in the images of three probe configurations were similar and were worse than the high-contrast case. The image artifacts are related to the reconstruction algorithm. When the target contrast is weak or the signal-to-noise ratio is low, the inversion algorithm produces artifacts around the edges of the images.

For shallow targets (here we set the target depth to be 1.5 cm) the NIR system has a relatively poorer performance. This is due to less source-detector pairs experiencing the existence of a shallow absorber. As shown in Fig. 9, image artifacts are obviously worse compared with Fig. 8. However, the conclusion about the hole size of the probe remains true. Table 2 lists all the measured imaging parameters obtained from three probe configurations. Although a 3 cm \times 3 cm hole is somewhat too big to obtain good enough results, the optimal hole size is in the neighborhood of 2 cm \times 2 cm. This optimal size is approximately the size of commercial ultrasound transducers.

In the above studies, we used the iteration number obtained from the no-hole configuration for the rest of the configurations. Ideally, the iteration should stop when the object function [see Eq. (2)] or the error performance surface reaches the noise floor. However, system noise, particularly coherent noise, was difficult to estimate from experimental data. In general, we found that the reconstructed values were closer to true values when the object function reached approximately 5–15% of the initial value (total energy in the measurements). Therefore we used this criterion ($\sim 10\%$ of the initial value) for the no-hole configuration. Because the signal-to-noise ratio of

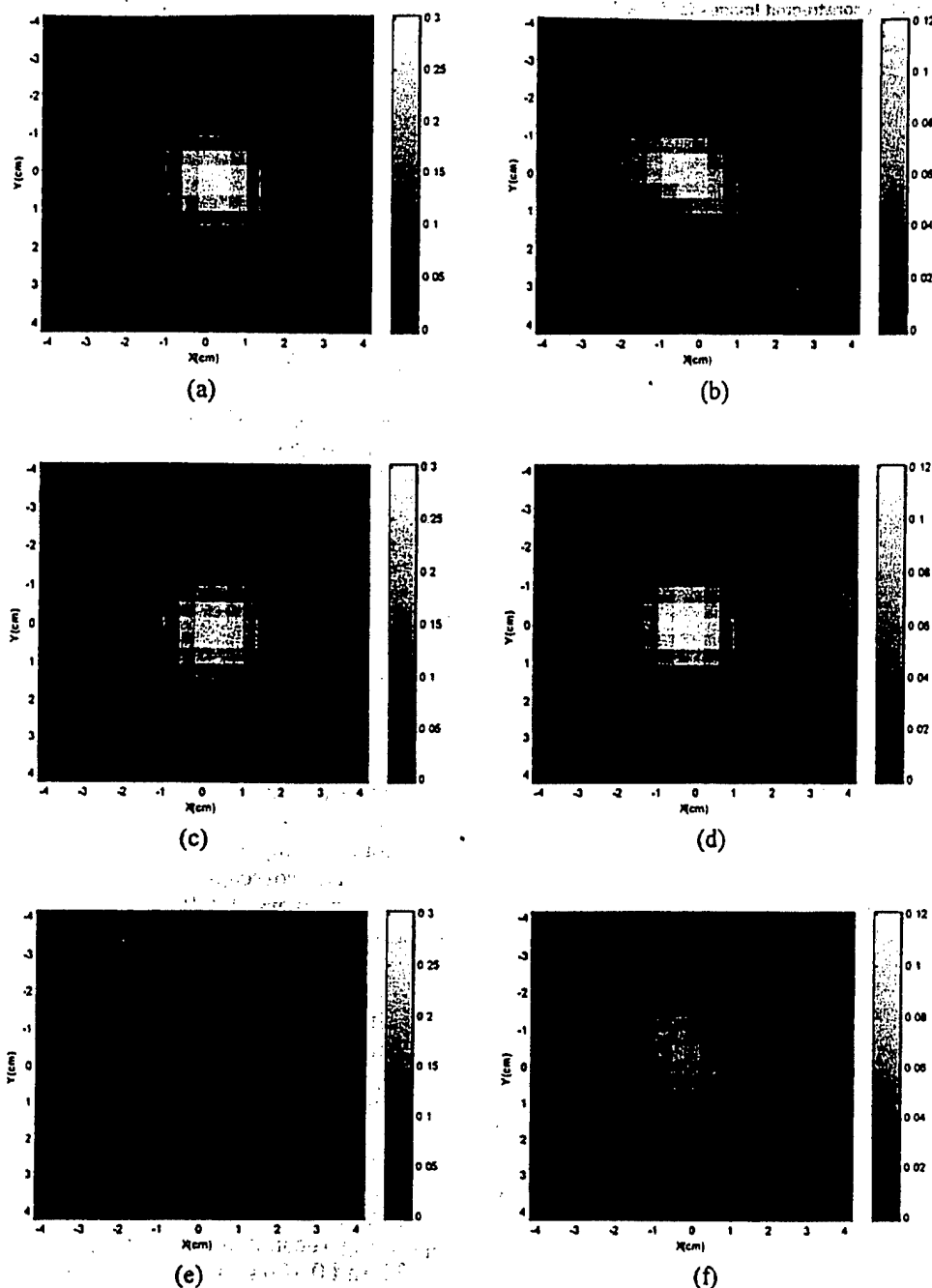


Fig. 8. Reconstructed NIR images of deeper targets (2.5 cm in depth, 1 cm in diameter, and the fitted background μ_a and μ_s' are 0.015 and 5.36 cm^{-1} , respectively). The left column corresponds to images of a high-contrast target ($\mu_a = 0.25 \text{ cm}^{-1}$) obtained from different probe configurations, and the right column corresponds to images of a low-contrast target ($\mu_a = 0.1 \text{ cm}^{-1}$). Each row is related to a specific hole size: (a) and (b) no hole, (c) and (d) $2 \text{ cm} \times 2 \text{ cm}$, (e) and (f) $3 \text{ cm} \times 3 \text{ cm}$.

the data decreased with the increase in hole size, we could not find consistent criterion for both no-hole and hole data. Therefore we used the same iteration number obtained from the no-hole case for the hole configurations, and the comparison was based on the same iteration number.

B. Ultrasound-Guided Near-Infrared Imaging

Three-dimensional ultrasound images can provide 3-D distributions of targets. With the *a priori* target

depth information, the optical reconstruction can be improved significantly. An example is given in Fig. 10. The target again was a 1-cm-diameter gel ball of low ($\mu_a = 0.1 \text{ cm}^{-1}$) optical contrast and was embedded at approximately (0, 0, 2.5 cm) inside the Intralipid medium. The fitted background μ_a and μ_s' are 0.02 and 5.08 cm^{-1} , respectively. The combined probe shown in Fig. 2 was used to obtain the ultrasound and NIR data simultaneously. Figure 10(a) shows an A-scan line of a returned ultrasound echo

Table 1. Parameters of Reconstructed Images for Deep High-Contrast ($\mu_a = 0.25\text{-cm}^{-1}$) and Low-Contrast ($\mu_a = 0.1\text{-cm}^{-1}$) Targets^a

Parameter	Probe Type		
	No Hole	2 cm × 2 cm	3 cm × 3 cm
High contrast			
$\hat{\mu}_{a(\max)}^b$ (cm^{-1})	0.251	0.234	0.104
FWHM ^c (cm)	1.85	1.91	2.44
Artifacts (dB)	Background (-22)	Background	-14.3
Low contrast			
$\hat{\mu}_{a(\max)}$ (cm^{-1})	0.105	0.111	0.064
FWHM (cm)	2.02	1.83	2.16
Artifacts (dB)	-6.90	-8.10	-5.65

^aThe fitted background μ_a and μ_s' are 0.015 and 5.36 cm^{-1} , respectively.

^b $\hat{\mu}_{a(\max)}$ is the measured maximum value of the reconstructed absorption coefficient map.

^cFWHM is defined as the geometric mean of the widths measured at longer and shorter axes of the elliptical image lobe.

signal received by one ultrasound transducer located on top of the target. As acoustic scatters were uniformly distributed in the target, signals were reflected from inside the target as well as from the surfaces. The reflected signals from the front and back surfaces of the gel ball can be clearly identified in the echo signal. On the basis of the target depth, we reconstructed the optical absorption coefficient at the target depth only (1 cm in thickness) by setting the perturbations from the other depths equal to zero. We also performed 3-D optical-only reconstruction. Figure 10(b) shows the reconstructed absorption image from a 3-D optical-only reconstruction [layer three of voxel coordinates ($x, y, 2.5\text{ cm}$) and 1 cm thick], whereas Fig. 10(c) shows the reconstructed image of the corresponding target from ultrasound-guided reconstruction. For optical-only reconstruction, the algorithm did not converge to a localized spatial region, and the image contrast was poor. The measured maximum absorption coefficient was 0.088 cm^{-1} , which was close to the true value. However, the measured spatial location of the maximum value was $(-1.6, -1.2\text{ cm})$, which was too far from the true target location. With the *a priori* target depth, the reconstruction performed at the target layer can localize the target to the correct spatial position. The measured maximum absorption coefficient was 0.12 cm^{-1} and its location was $(0, 0.4\text{ cm})$, which was very close to the true target location. This example demonstrates that *a priori* target depth can significantly improve the reconstruction accuracy and target localization.

In addition to use of *a priori* target depth information, we can also use the target spatial distribution provided by ultrasound to guide the reconstruction. We performed a set of experiments with two targets

located at 2.5 cm in depth inside the Intralipid. Each target is a 1-cm^3 gel cube containing ultrasound scatters. For optical properties, they both could be high contrast ($\mu_a = 0.25\text{ cm}^{-1}$) or low contrast ($\mu_a = 0.1\text{ cm}^{-1}$), but had the same reduced scattering coefficient as the background. The fitted background μ_a and μ_s' are 0.017 and 4.90 cm^{-1} , respectively. One target was centered approximately at $(-1.0, -1.0, 2.5\text{ cm})$, whereas the other was at $(1.0, 1.0, 2.5\text{ cm})$. The distance between the centers of the two targets was 2.8 cm.

Figure 11(a) is the ultrasound image of two high-contrast targets. As the field of view of the ultrasound system was nearly a $3\text{ cm} \times 3\text{ cm}$ square, these two targets appeared at diagonal corners. The measured peak positions of the two targets were $(-0.6, -1.0\text{ cm})$ and $(1.0, 1.0\text{ cm})$, which differed from the true target locations by only one voxel. The low contrast of the ultrasound image is related to the speckle noise. Because our ultrasound array is sparse, the imaging quality is not state of the art (see more discussion in Section 5). The NIR image of these targets was obtained simultaneously and is shown in Figure 11(b). We performed the reconstruction at the target layer by taking advantage of target depth information. A total of 123 iterations was used to obtain Fig. 11(b). The measured peak positions of the two targets were $(-1.4, -1.0\text{ cm})$ and $(0.6, 0.6\text{ cm})$, which were one voxel off from the true target locations $(-1.0, -1.0\text{ cm})$ and $(1.0, 1.0\text{ cm})$, respectively. The corresponding reconstructed absorption coefficients were 0.242 and 0.251 cm^{-1} , which were close to the true values. However, the two targets were almost connected to each other, and their spatial localization was poor. For low-contrast targets, the ultrasound image is shown in Fig. 11(c), and the measured peak locations of the two targets were $(-1.0, -0.6\text{ cm})$ and $(0.6, 1.0\text{ cm})$, which differed from the true target locations by only one voxel. The corresponding NIR image is shown in Fig. 11(d), and the measured peak locations of the two targets were $(-2.2, -1.0\text{ cm})$ and $(0.6, 1.0\text{ cm})$. The left target was off the true location by three voxels. The corresponding reconstructed absorption coefficients were 0.063 and 0.1004 cm^{-1} at 87 iteration steps. As one can see, the target shape and localization were poorer than those in the high-contrast case. In addition, an artifact appeared at the edge of the image.

From the coregistered ultrasound images, we obtained spatial distributions of the two targets and specified target regions. Figures 12(a) and 12(c) show the -6-dB contour plots of Figs. 11(a) and 11(c). Applying the same reconstruction scheme to these specific regions, we obtained Figs. 12(b) and 12(d) in one iteration. The reconstructed absorption coefficients were 0.2357 and 0.219 cm^{-1} for the two high-contrast target cases and 0.123 and 0.131 cm^{-1} for the low-contrast case. We can see much better improvement in the low-contrast target case when we compare Fig. 12(d) with Fig. 11(d). This example demonstrates that, when the targets are visible in ultrasound images, their morphology information

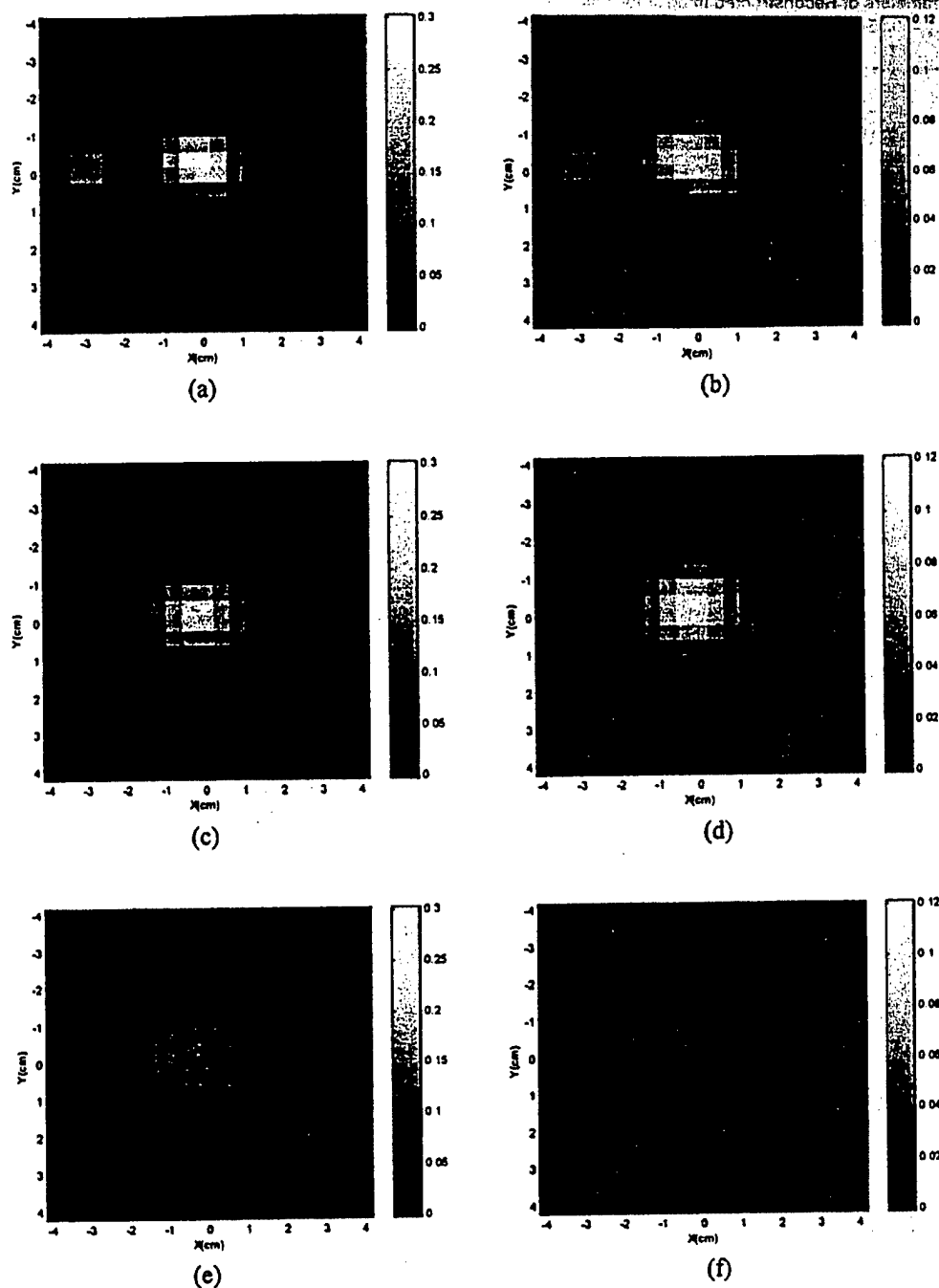


Fig. 9. Reconstructed NIR images for shallow targets (1.5 cm in depth, 1 cm in diameter, and the fitted background μ_a and μ_s' are 0.015 and 5.36 cm^{-1} , respectively). The left column corresponds to images of a high-contrast target ($\mu_a = 0.25 \text{ cm}^{-1}$), and the right column corresponds to images of a low-contrast target ($\mu_a = 0.1 \text{ cm}^{-1}$). Each row is related to a specific hole size: (a) and (b) no hole, (c) and (d) $2 \text{ cm} \times 2 \text{ cm}$, (e) and (f) $3 \text{ cm} \times 3 \text{ cm}$.

provided by ultrasound can be used to guide the optical reconstruction in the specified regions.

The result regarding the iteration step is significant. As we discussed above, there is no known stopping criterion to terminate the iteration because it is difficult to estimate the noise level in the measurements. With the *a priori* target depth and spatial distribution provided by coregistered ultrasound, we can obtain an accurate optical absorption coefficient in one iteration. Therefore no stopping crite-

rion is needed for the inversion algorithms. However, this result will need to be further evaluated with more samples of different contrasts.

5. Discussion

Commercial ultrasound scanners use one-dimensional probes that provide 2-D images of x - z views of the targets, where x and z are the spatial and propagation dimensions, respectively. Such x - z images cannot coregister with NIR images, which are

Table 2. Parameters of Reconstructed Images for Shallow High-Contrast ($\mu_a = 0.25\text{-cm}^{-1}$) and Low-Contrast ($\mu_a = 0.1\text{-cm}^{-1}$) Targets^a

Parameter	Probe Type		
	No Hole	2 cm \times 2 cm	3 cm \times 3 cm
High contrast			
$\hat{\mu}_{a(\max)}$ (cm^{-1})	0.250	0.194	0.118
FWHM (cm)	1.32	1.61	2.08
Artifacts (dB)	-7.98	-12.7	-9.76
Low contrast			
$\hat{\mu}_{a(\max)}$ (cm^{-1})	0.100	0.091	0.042
FWHM (cm)	1.88	2.11	3.17
Artifacts (dB)	-6.25	-7.44	-0.65

^aThe fitted background μ_a and μ_s' are 0.015 and 5.35 cm^{-1} , respectively.

obtained from x - y views of the targets. Our current 2-D ultrasound array is capable of providing x - y views of the targets, which can be used to coregister with NIR images. However, the array is sparse and therefore the image resolution is not state of the art. Nevertheless, its spatial resolution is comparable to NIR imaging and can be used to guide NIR image reconstruction. With 3-D ultrasound guidance, only one iteration is needed to obtain accurate absorption coefficients. This result is significant because no stopping criterion is necessary. More studies with a variety of target contrasts and locations will be performed to verify this result.

We purchased a 2-D state-of-the-art ultrasound array of 1280 transducer elements and we are building a multiplexing unit for our 64-channel electronics. In addition, the new 2-D transducer size is approximately $2\text{ cm} \times 3\text{ cm}$, which is in the neighborhood of the optimal hole size we found through this study. With the new 2-D ultrasound transducer, we will be able to obtain high-resolution ultrasound images and delineate the target boundaries with finer details for optical reconstruction.

Ultrasound contrast depends on lesion acoustic properties, and NIR optical contrast is related to lesion optical properties. Both contrasts exist in tumors, but the sensitivities of these two modalities may be different. It is possible that some early-stage cancers have NIR contrast but are not detectable by ultrasound. It would be desirable if we could obtain sensitivity of optical imaging alone. However, light scattering is a main problem that prevents the accurate and reliable localization of lesions. It is also possible that some lesions have acoustic contrast but no NIR contrast or low NIR contrast. Currently, ultrasound is routinely used as an adjunct tool to x-ray mammography; the combined sensitivity of these two modalities in breast cancer detection is

more than 90%.²⁹ Recently, ultrasound has also been advocated to screen dense breasts.³⁰ We anticipate that our combined imaging will add more specificity to the ultrasonically detected lesions.

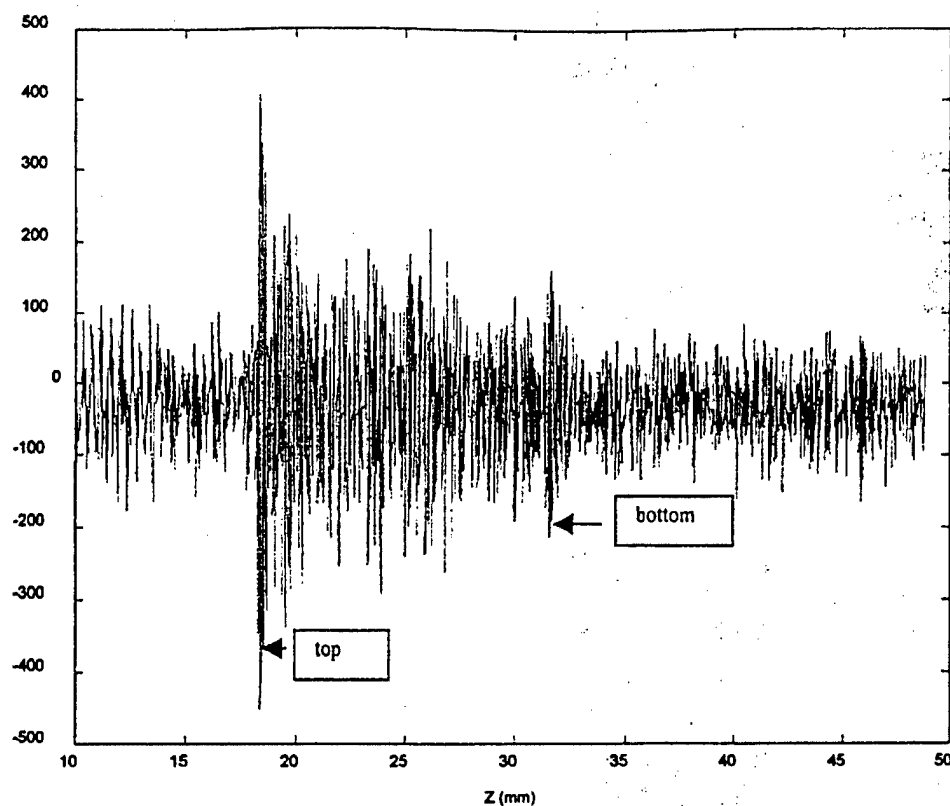
In the reported phantom studies, we assigned zero perturbations to the regions where no targets were present. In clinical studies, we plan to segment the ultrasound images and specify different tissue types as well as suspicious regions in the segmented images. We will then reduce the reconstructed optical unknowns by assigning unknown optical properties to different tissue types as well as to suspicious regions. Finally, we will reconstruct the reduced sets of unknown optical properties. We expect a more accurate estimation of reconstructed optical properties and fast convergence speed, as reported in this paper. However, it is still too early to judge the clinical performance of the combined method; further clinical studies are needed.

Probing regions of the banana-shaped diffusive photons depend on source-detector separations and measurement geometry. For a semi-infinite geometry, the probing regions extend further into the medium when source-detector separation increases. This is why we have multiple source-detector pairs of various separations to detect targets at variable depths from 0.5 to 4 cm . Of course it is hard to achieve uniform sensitivity in the entire region of interest. For example, a superficial target ($\sim 1\text{ cm}$ deep) would cause strong perturbations when it is close to a source or a detector, but will result in much weaker signals when it is located deeper. Normalization of scattering photon density waves with respect to the incident waves makes it possible for reconstruction algorithms to handle the huge dynamic range of signals and to detect a target as deep as 4 cm . This normalization procedure was applied to the reconstruction algorithm used to obtain the reported images.

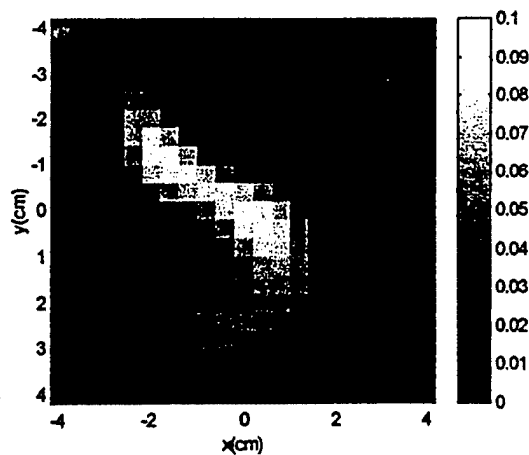
In this study, the target absorption coefficient was reconstructed from the measurements. Because the target μ_s' was similar to the background μ_s' , the coupling between μ_a and μ_s' in our measurements was negligible. We also performed experiments with gel phantom made with Intralipid with a concentration similar to that of the background and did not observe perturbation beyond the noise level. Similar reconstruction studies can be performed for scattering coefficients as well. Simultaneous reconstruction of both absorption and scattering coefficients is also possible. Because the eigenvalues of the absorption and scattering weight matrices are significantly different, good regulation schemes are needed for simultaneous reconstruction. This subject is one of our topics for further study.

6. Summary

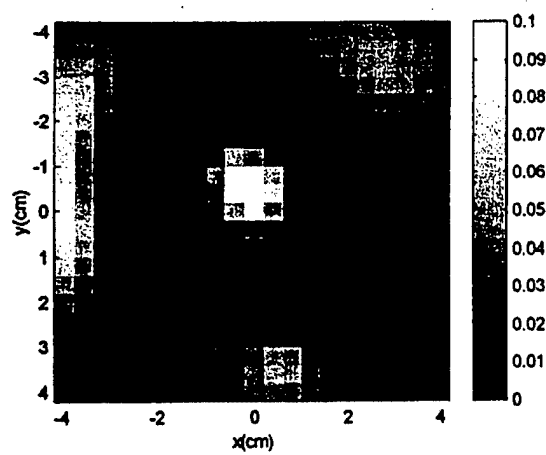
We have constructed a near-real-time imager that can provide coregistered ultrasound and NIR images simultaneously. This new technique is designed to improve the specificity of breast cancer diagnosis. Because the ultrasound transducer needs to occupy



(a)



(b)



(c)

Fig. 10. Deep target (2.5 cm in depth, 1 cm in diameter) of low optical contrast ($\mu_a = 0.10 \text{ cm}^{-1}$ and fitted background μ_a and μ_s' are 0.02 and 5.08 cm^{-1} , respectively). (a) A-scan line of the reflected ultrasound pulse-echo signal indicating the target depth. (b) Absorption image of the low-contrast target obtained from optical-only reconstruction. (c) Ultrasound-guided reconstruction at target depth.

the central region of the combined probe, a series of experiments were conducted to investigate the effects of missing optical sensors in the middle of the combined probe on the NIR image quality. Our results have shown that, as long as the central ultrasound transducer area is in the neighborhood of $2 \text{ cm} \times 2$

cm, essentially similar reconstruction results as those of no missing optical sensors in the middle of the combined probe can be obtained. This $2 \text{ cm} \times 2$ cm dimension is approximately the size of most commercial ultrasound phased-array transducers. When the central missing optical sensor area is in-

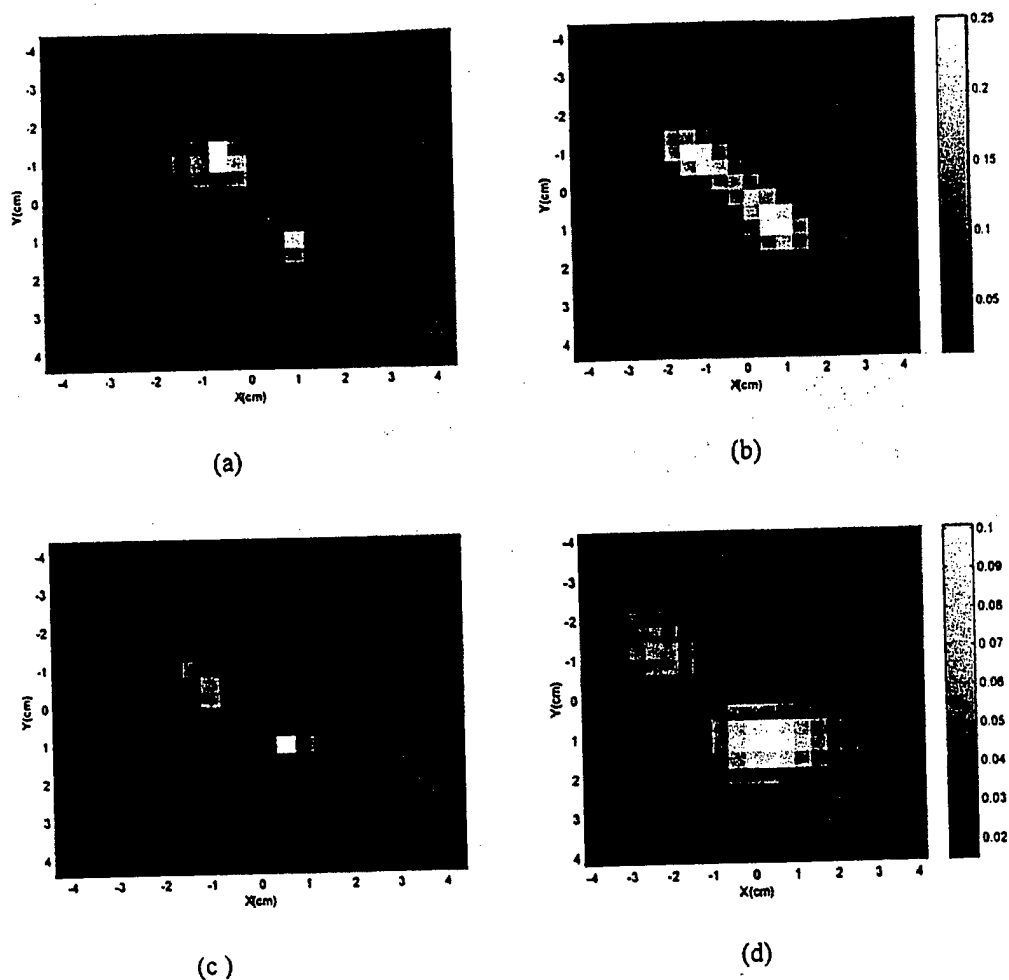


Fig. 11. Simultaneously obtained ultrasound and NIR absorption images. The fitted background μ_a and μ_s' are 0.017 and 4.90 cm^{-1} , respectively. (a) Ultrasound and (b) NIR absorption image of two high-contrast targets (target $\mu_a = 0.25 \text{ cm}^{-1}$). (c) Ultrasound and (d) NIR image of two low-contrast targets (target $\mu_a = 0.10 \text{ cm}^{-1}$). In both high- and low-contrast cases, the two targets were located at 2.5 cm in depth.

creased to $3 \text{ cm} \times 3 \text{ cm}$, however, the reconstructed values are obviously lower than real values. If we increase the iteration steps, artifacts in the reconstructed images would soon become dominant.

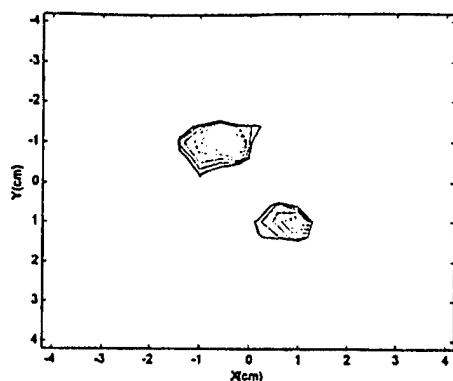
With the target 3-D distribution provided by coregistered ultrasound, significant improvements in algorithm convergence and reconstruction speed were achieved. In general, *a priori* target depth information guides the inversion algorithm to reconstruct the heterogeneities at the correct spatial locations and improves the reconstruction speed by an order of magnitude. In addition, the *a priori* target spatial distribution can further reduce the iteration to one step and also obtain accurate optical absorption coefficients. Given the fact that no known stopping criterion is available, this result is significant because no iteration is needed. However, this result will need to be evaluated with more samples of different contrasts.

We acknowledge the following for their funding support: the state of Connecticut (99CT21), U.S. Department of Defense Army Breast Cancer Pro-

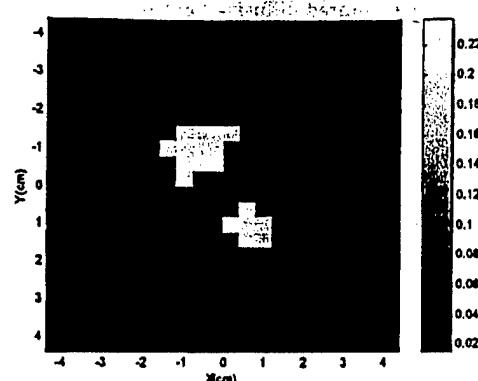
gram (DAMD17-00-1-0217, DAMD17-01-1-0216), and Multiple-Dimensional Technology, Inc.

References

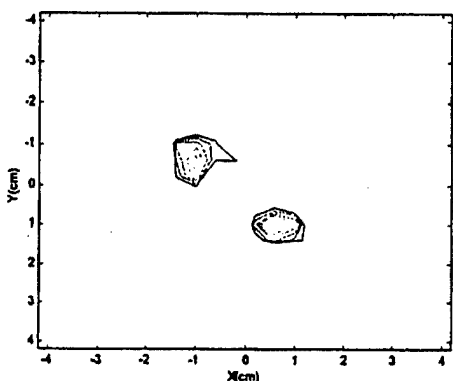
1. T. A. Stavros, D. Thickman, and C. Rapp, "Solid breast nodules: use of sonography to distinguish between benign and malignant lesions," *Radiology* **196**, 123-134 (1995).
2. G. Rahbar, A. C. Sie, G. C. Hansen, J. S. Prince, M. L. Melany, H. Reynolds, V. P. Jackson, J. W. Sayre, and L. W. Bassett, "Benign versus malignant solid breast masses: US differentiation," *Radiology* **213**, 889-894 (1999).
3. V. P. Jackson, "The current role of ultrasonography in breast imaging," *Radiol. Clin. North Am.* **33**, 1161-1170 (1995).
4. B. Tromberg, N. Shah, R. Lanning, A. Cerussi, J. Espinoza, T. Pham, L. Svaasand, and J. Butler, "Non-invasive *in vivo* characterization of breast tumors using photon migration spectroscopy," *Neoplasia* **2**, 26-40 (2000).
5. S. Fantini, S. Walker, M. Franceschini, M. Kaschke, P. Schlag, and K. Moesta, "Assessment of the size, position, and optical properties of breast tumors *in vivo* by noninvasive optical methods," *Appl. Opt.* **37**, 1982-1989 (1998).
6. S. M. Nioka, M. Shnall, M. Miwa, S. Orel, M. Haida, S. Zhao, and B. Chance, "Photon imaging of human breast cancer," *Adv. Exp. Med. Biol.* **16**, 171-179 (1994).
7. R. M. Danen, Y. Wang, X. D. Li, W. S. Thayer, and A. G. Yodh,



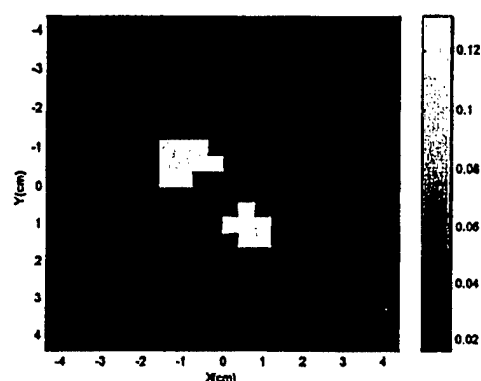
(a)



(b)



(c)



(d)

Fig. 12. (a) and (c) -6-dB contour plots of ultrasound images shown in Figs. 11(a) and 11(c). The outer contour is -6 dB from the peak, and the contour spacing is 1 dB. (b) and (d) Corresponding NIR absorption maps reconstructed in target regions specified by ultrasound.

- "Regional imager for low resolution functional imaging of the brain with diffusing near-infrared light," *Photochem. Photobiol.* **67**, 33-40 (1998).
8. T. McBride, B. W. Pogue, E. Gerety, S. Poplack, U. Osterberg, B. Pogue, and K. Paulsen, "Spectroscopic diffuse optical tomography for the quantitative assessment of hemoglobin concentration and oxygen saturation in breast tissue," *Appl. Opt.* **38**, 5480-5490 (1999).
 9. M. A. Franceschini, K. T. Moesta, S. Fantini, G. Gaida, E. Gratton, H. Jess, M. Seeber, P. M. Schlag, and M. Kashke, "Frequency-domain techniques enhance optical mammography: initial clinical results," *Proc. Natl. Acad. Sci. USA* **94**, 6468-6473 (1997).
 10. J. B. Fishkin, O. Coquoz, E. R. Anderson, M. Brenner, and B. J. Tromberg, "Frequency-domain photon migration measurements of normal and malignant tissue optical properties in a human subject," *Appl. Opt.* **36**, 10-20 (1997).
 11. T. L. Troy, D. L. Page, and E. M. Sevick-Muraca, "Optical properties of normal and diseased breast tissues: prognosis for optical mammography," *J. Biomed. Opt.* **1**, 342-355 (1996).
 12. R. J. Grable, D. P. Rohler, and S. Kla, "Optical tomography breast imaging," in *Optical Tomography and Spectroscopy of Tissue: Theory, Instrumentation, Model, and Human Studies II*, B. Chance and R. Alfano, eds., *Proc. SPIE* **2979**, 197-210 (1997).
 13. Y. Yao, Y. Wang, Y. Pei, W. Zhu, and R. L. Barbour, "Frequency-domain optical imaging of absorption and scattering distributions by a Born iterative method," *J. Opt. Soc. Am. A* **14**, 325-341 (1997).
 14. H. Jiang, K. Paulsen, U. Osterberg, B. Pogue, and M. Patterson, "Optical image reconstruction using frequency-domain data: simulations and experiments," *J. Opt. Soc. Am. A* **12**, 253-266 (1995).
 15. X. Li, T. Durduran, A. Yodh, B. Chance, and D. N. Pattanayak, "Diffraction tomography for biomedical imaging with diffuse-photon density waves," *Opt. Lett.* **22**, 573-575 (1997).
 16. C. Matson and H. Liu, "Backpropagation in turbid media," *J. Opt. Soc. Am. A* **16**, 1254-1265 (1999).
 17. M. A. O'Leary, "Imaging with diffuse photon density waves," Ph.D. dissertation (University of Pennsylvania, Philadelphia, Pa., 1996).
 18. K. Paulsen, P. Meaney, M. Moskowitz, and J. Sullivan, Jr., "A dual mesh scheme for finite element based reconstruction algorithms," *IEEE Trans. Med. Imaging* **14**, 504-514 (1995).
 19. S. Arridge and M. Schweiger, "Photon-measurement density functions. Part I: Analytical forms," *Appl. Opt.* **34**, 7395-7409 (1995).
 20. S. Arridge and M. Schweiger, "Photon-measurement density functions. II. Finite-element-method calculations," *Appl. Opt.* **34**, 8026-8037 (1995).
 21. Q. Zhu, T. Dunrana, M. Holboke, V. Ntziachristos, and A. Yodh, "Imager that combines near-infrared diffusive light and ultrasound," *Opt. Lett.* **24**, 1050-1052 (1999).
 22. Q. Zhu, D. Sullivan, B. Chance, and T. Dambro, "Combined

- ultrasound and near infrared diffusive light imaging," *IEEE Trans. Ultrason. Ferroelectr. Freq. Control* **46**, 665-678 (1999).
23. Q. Zhu, E. Conant, and B. Chance, "Optical imaging as an adjunct to sonograph in differentiating benign from malignant breast lesions," *J. Biomed. Opt.* **5**(2), 229-236 (2000).
24. Q. Zhu, N. G. Chen, D. Q. Piao, P. Y. Guo, and X. H. Ding, "Design of near-infrared imaging probe with the assistance of ultrasound localization," *Appl. Opt.* **40**, 3288-3303 (2001).
25. M. Jholboke, B. J. Tromberg, X. Li, N. Shah, J. Fishkin, D. Kidney, J. Butler, B. Chance, and A. G. Yodh, "Three-dimensional diffuse optical mammography with ultrasound localization in human subject," *J. Biomed. Opt.* **5**(2), 237-247 (2000).
26. W. Zhu, Y. Wang, and J. Zhang, "Total least-squares reconstruction with wavelets for optical tomography," *J. Opt. Soc. Am. A* **15**, 2639-2650 (1998).
27. P. C. Li, W. Flax, E. S. Ebbini, and M. O'Donnell, "Blocked element compensation in phased array imaging," *IEEE Trans. Ultrason. Ferroelectr. Freq. Control* **40**(4), 283-292 (1993).
28. G. H. Golub, "Some modified matrix eigenvalue problems," *SIAM (Soc. Ind. Appl. Math.) Rev.* **15**, 318-334 (1973).
29. H. Zonderland, E. G. Coerkamp, J. Hermans, M. J. van de Vijver, and A. E. van Voorthuisen, "Diagnosis of breast cancer: contribution of US as an adjunct to mammography," *Radiology* **213**, 413-422 (1999).
30. T. M. Kolb, J. Lichy, and J. H. Newhouse, "Occult cancer in women with dense breast: detection with screening US-diagnostic yield and tumor characteristics," *Radiology* **207**, 191-199 (1998).

Design of near-infrared imaging probe with the assistance of ultrasound localization

Quing Zhu, Nan Guang Chen, Daqing Piao, Puyun Guo, and XiaoHui Ding

A total of 364 optical source-detector pairs were deployed uniformly over a 9 cm × 9 cm probe area initially, and then the total pairs were reduced gradually to 60 in experimental and simulation studies. For each source-detector configuration, three-dimensional (3-D) images of a 1-cm-diameter absorber of different contrasts were reconstructed from the measurements made with a frequency-domain system. The results have shown that more than 160 source-detector pairs are needed to reconstruct the absorption coefficient to within 60% of the true value and appropriate spatial and contrast resolution. However, the error in target depth estimated from 3-D images was more than 1 cm in all source-detector configurations. With the *a priori* target depth information provided by ultrasound, the accuracy of the reconstructed absorption coefficient was improved by 15% and 30% on average, and the beam width was improved by 24% and 41% on average for high- and low-contrast cases, respectively. The speed of reconstruction was improved by ten times on average. © 2001 Optical Society of America

OCIS codes: 170.0170, 170.3010, 170.5270, 170.7170, 170.3830.

1. Introduction

Recently, optical imaging techniques based on diffusive near-infrared (NIR) light have been employed to obtain interior optical properties of human tissues.¹⁻⁸ Functional imaging with NIR light has the potential to detect and diagnose diseases or cancers through the determination of hemoglobin concentration, blood O₂ saturation, tissue light scattering, water concentration, and the concentration and lifetime of exogenous contrast agents. Optical imaging requires that an array of sources and detectors be distributed directly or coupled through optical fibers on a boundary surface. Measurements made at all source-detector positions can be used in tomographic image reconstruction schemes to determine optical properties of the medium. The frequently used geometric configurations of sources and detectors are ring arrays^{4,9-11} and planar arrays.^{3,12-15} A ring array consists of multiple sources and detectors that can be distributed uniformly on a ring. Optical properties of the thin tissue slice (two-dimensional slice) enclosed by

the ring can be determined from all measurements. A planar array can be configured with either transmission or reflection geometries. In transmission geometry, multiple detectors can be deployed on a planar array, and multiple sources or a single source can be deployed on an opposite plane parallel to the detector plane. Optical properties of the three-dimensional (3-D) tissue volume between the source and the detector planes can be determined from all measurements. In reflection geometry, multiple sources and detectors can be distributed on a planar probe that can be hand-held.^{3,15} Optical properties of the 3-D tissue volume at slice depths below the probe can be determined from all measurements. The reflection probe configuration is desirable for the imaging of brain and breast tissues.

Although many researchers in the field have constructed imaging probes using reflection geometry,^{2,3,15} to our knowledge the required total number of source-detector pairs over a given probe area needed to accurately reconstruct optical properties and localized spatial and depth distributions has not been addressed before. In this paper we study the relationship between the total number of source-detector pairs and the reconstructed imaging quality through experimental measurements. Computer simulations are performed to assist in understanding the experimental results.

Because the target localization from diffusive waves is difficult, our group and others have introduced use of *a priori* target location information pro-

The authors are with the Department of Electrical and Computer Engineering, University of Connecticut, 260 Glenbrook Road, U157, Storrs, Connecticut 06269. Q. Zhu's e-mail address is zhu@engr.uconn.edu.

Received 20 September 2000; revised manuscript received 21 March 2001.

0003-6935/01/193288-16\$15.00/0

© 2001 Optical Society of America

vided by ultrasound to improve optical imaging.¹⁵⁻¹⁸ In this paper we demonstrate experimentally that the accurate target depth information can significantly improve the accuracy of the reconstructed absorption coefficient and the reconstruction speed for any optical array configuration.

The required total number of source-detector pairs is also related to the image reconstruction algorithms used. In this paper we obtained experimental measurements using a frequency-domain system with the source amplitude modulated at 140 MHz. In simulations, forward measurements were generated by use of the analytic solution of a photon density wave scattered by a spherical inhomogeneity embedded in a semi-infinite scattering medium.¹⁹ In both experiments and simulations, linear perturbation theory within the Born approximation was used to relate optical signals at the probe surface to absorption variations in each volume element within the sample. The total least-squares (TLS) method²⁰⁻²² was used to formulate the inverse problem. The conjugate gradient technique was employed to iteratively solve the inverse problem. Therefore the results we obtained are directly relevant to the probe design with reconstruction algorithms based on the linear perturbation theory and can be used as a first-order approximation if high-order perturbations are employed in image reconstructions.

This paper is organized as follows. In Section 2 we describe an analytic solution used to generate simulated forward data, the Born approximation, and the TLS method for image reconstruction. In Section 3 we discuss the probe geometry, a frequency-domain NIR system used to acquire the experimental measurements, and an ultrasound subsystem used to acquire the target depth information, computation procedures used to obtain both simulated and experimental absorption images. In Sections 4 and 5 we report experimental results obtained from the dense and sparse arrays with and without *a priori* target depth information. A high-contrast example is given in Section 4, and a low-contrast case is given in Section 5. Simulations are performed to assist in understanding the noise on the image reconstruction. Imaging parameters evaluated are a -6-dB width of the image lobe, the reconstructed maximum value of the absorption coefficient and its spatial location, and the image artifact level. In Sections 6 and 7 we provide a discussion and summary, respectively.

2. Basic Principles

A. Forward Model

In our experiments, forward measurements were made with a frequency-domain system operating at a 140-MHz modulation frequency. In computer simulations, forward measurements were generated from an analytic solution of a photon density wave scattered by a spherical inhomogeneity.¹⁹ When the center of the sphere coincides with the origin of spherical coordinates, the solution for the scattered

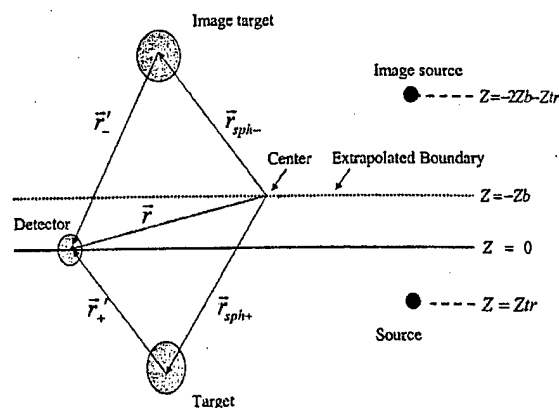


Fig. 1. Target, source, and detector configurations for a semi-infinite medium.

photon density wave U_{sc} outside the sphere at a detector position $\mathbf{r} = (r, \theta, \phi)$ is of the form

$$U_{sc}(\mathbf{r}, \omega) = \sum_{l,m} \{A_{l,m} [j_l(k^{out}r) + j_n_l(k^{out}r)] Y_{l,m}(\theta, \phi)\}, \quad (1)$$

where j_l and n_l are spherical Bessel and Neuman functions, respectively; $Y_{l,m}(\theta, \phi)$ are the spherical harmonics, and $k^{out} = [(-\nu\mu_a^{out} + j\omega)/D^{out}]^{1/2}$ is the complex wave number outside the sphere. ω is the angular modulation frequency of the light source, μ_a^{out} is the absorption coefficient outside the sphere, and D^{out} is the photon diffusion coefficient outside the sphere given by $D^{out} = 1/(3\mu_s')$, where μ_s' is the reduced scattering coefficient outside the sphere. The coefficients $A_{l,m}$, determined by the boundary conditions, are

$$A_{l,m} = -(j\nu S k^{out}/D^{out}) h_l^{(1)}(k^{out}r_s) Y_{l,m}^*(\theta_s, \phi_s) \times \frac{D^{out} x j_l(y) j_l'(x) - D^{in} y j_l'(y) j_l(x)}{D^{out} x h_l^{(1)'}(x) j_l(y) - D^{in} y h_l^{(1)}(x) j_l'(y)}, \quad (2)$$

where $x = k^{out}a$, $y = k^{in}a$, $\mathbf{r}_s = (r_s, \theta_s, \phi_s)$ is the source position, $h_l^{(1)}$ are the Hankel functions of the first kind, and j_l' and $h_l^{(1)'}$ are the first derivatives of j_l and $h_l^{(1)}$. The analytic solution has the important advantage in that it is exact to all orders of perturbation theory and thus can represent accurate measurements.

We generalized the above analytic solution to a semi-infinite geometry by using a method of images with extrapolated boundary conditions (see Fig. 1). A type I boundary condition (zero light energy density at the extrapolated boundary) is used to derive the scattered wave U_{sc}' . To calculate the U_{sc}' in semi-infinite geometry, we use $\mathbf{r}_{sph+} = (r_{0+}, \theta_{0+}, \phi_{0+})$ and $\mathbf{r}_{sph-} = (r_{0-}, \theta_{0-}, \phi_{0-})$ to represent the centers of the sphere and the image sphere, respectively. The vectors $\mathbf{r}_+ = \mathbf{r} - \mathbf{r}_{sph+} = (r_+, \theta_+, \phi_+)$ and $\mathbf{r}_- = \mathbf{r} - \mathbf{r}_{sph-} = (r_-, \theta_-, \phi_-)$ are therefore pointing to the detector position $\mathbf{r} = (r, \theta, \phi)$ from the sphere and the

image sphere, respectively. The semi-infinite solution of U_{sc}' can be approximated as

$$U_{sc}'(\mathbf{r}, \omega) = \sum_{l,m} \{A_{l,m}^+[j_l(k^{\text{out}}r_+')]Y_{l,m}(\theta_+', \phi_+') + jn_l(k^{\text{out}}r_+')Y_{l,m}(\theta_+', \phi_+')\} - \sum_{l,m} \{A_{l,m}^-[j_l(k^{\text{out}}r_-')]Y_{l,m}(\theta_-', \phi_-') + jn_l(k^{\text{out}}r_-')Y_{l,m}(\theta_-', \phi_-')\} + \sum_{l,m} \{A_{l,m}^+[j_l(k^{\text{out}}r_+')]Y_{l,m}(\theta_+', \phi_+') + jn_l(k^{\text{out}}r_+')Y_{l,m}(\theta_+', \phi_+')\} - \sum_{l,m} \{A_{l,m}^-[j_l(k^{\text{out}}r_-')]Y_{l,m}(\theta_-', \phi_-') + jn_l(k^{\text{out}}r_-')Y_{l,m}(\theta_-', \phi_-')\}, \quad (3)$$

where

$$A_{l,m}^+ = -(j\nu SK^{\text{out}}/D^{\text{out}})h_l^{(1)}(k^{\text{out}}r_s^+)Y_{l,m}^*(\theta_s^+, \phi_s^+) \times \left[\frac{D^{\text{out}}x_{j_l}(y)j_l'(x) - D^{\text{in}}y_{j_l'}(y)j_l(x)}{D^{\text{out}}xh_l^{(1)'}(x)j_l(y) - D^{\text{in}}yh_l^{(1)}(x)j_l'(y)} \right], \quad (4)$$

$$A_{l,m}^- = -(j\nu SK^{\text{out}}/D^{\text{out}})h_l^{(1)}(k^{\text{out}}r_s^-)Y_{l,m}^*(\theta_s^-, \phi_s^-) \times \left[\frac{D^{\text{out}}x_{j_l}(y)j_l'(x) - D^{\text{in}}y_{j_l'}(y)j_l(x)}{D^{\text{out}}xh_l^{(1)'}(x)j_l(y) - D^{\text{in}}yh_l^{(1)}(x)j_l'(y)} \right]. \quad (5)$$

$\mathbf{r}_s^+ = (r_s^+, \theta_s^+, \phi_s^+)$ and $\mathbf{r}_s^- = (r_s^-, \theta_s^-, \phi_s^-)$ are the positions of the source and the image source, respectively.

The incident photon density wave at the detector position \mathbf{r} has the following form³:

$$U_{\text{inc}}(\mathbf{r}, \omega) = \frac{S}{4\pi D^{\text{out}}} \left[\frac{\exp(jk^{\text{out}}|\mathbf{r} - \mathbf{r}_s^+|)}{|\mathbf{r} - \mathbf{r}_s^+|} - \frac{\exp(jk^{\text{out}}|\mathbf{r} - \mathbf{r}_s^-|)}{|\mathbf{r} - \mathbf{r}_s^-|} \right]. \quad (6)$$

The total photon density at detector \mathbf{r} is a superposition of its incident (homogeneous) and scattered (heterogeneous) waves:

$$U(\mathbf{r}, \omega) = U_{\text{inc}}(\mathbf{r}, \omega) + U_{sc}'(\mathbf{r}, \omega). \quad (7)$$

B. Born Approximation for Reconstruction

The Born approximation was used to relate $U_{sc}'(\mathbf{r}, \omega)$ measured at the probe surface to absorption variations in each volume element within the sample. In the Born approximation, the scattered wave that originated from a source at \mathbf{r}_s and measured at detector \mathbf{r}_d can be related to the medium heterogeneity $\Delta\mu_a(\mathbf{r}_v)$ by

$$U_{sc}'(\mathbf{r}_d, \mathbf{r}_s, \omega) = \int G(\mathbf{r}_v, \mathbf{r}_d, \omega) U_{\text{inc}}(\mathbf{r}_v, \mathbf{r}_s, \omega) \times [\nu\Delta\mu_a(\mathbf{r}_v)/\bar{D}] d\mathbf{r}_v^3, \quad (8)$$

where $G(\mathbf{r}_v, \mathbf{r}_d, \omega)$ is the Green function and $\Delta\mu_a(\mathbf{r}_v) = \mu_a(\mathbf{r}_v) - \bar{\mu}_a$ is the medium absorption variation.¹¹ $\bar{\mu}_a$ is the average value of the medium absorption coefficient. By breaking the medium into discrete voxels, we obtain the following linear equations:

$$U_{sc}'(\mathbf{r}_{di}, \mathbf{r}_{si}, \omega) = \sum_j^N G(\mathbf{r}_{vj}, \mathbf{r}_{di}, \omega) U_{\text{inc}}(\mathbf{r}_{vj}, \mathbf{r}_{si}, \omega) \times [\nu\Delta\mu_a(\mathbf{r}_{vj})/\bar{D}] \Delta r_v^3. \quad (9)$$

When $W_{ij} = G(\mathbf{r}_{vj}, \mathbf{r}_{di}, \omega) U_{\text{inc}}(\mathbf{r}_{vj}, \mathbf{r}_{si}, \omega) \nu\Delta r_v^3/\bar{D}$, we obtain the matrix equation of Eq. (9):

$$[W]_{M \times N} \{\Delta\mu_a\}_{N \times 1} = [U_{sd}]_{M \times 1}. \quad (10)$$

The realistic constraints on $\Delta\mu_a$ are $(-\alpha \times \text{background } \mu_a) < \Delta\mu_a < 1$, where $0 < \alpha < 1$.

The above constraints ensure that the reconstructed absorption coefficient $\hat{\mu}_a = \text{background } \mu_a + \Delta\mu_a$ is positive and not unrealistically higher than unity. With M measurements obtained from all possible source-detector pairs in the planar array, we can solve N unknowns of $\Delta\mu_a$ by inverting the matrix Eq. (10). In general, the perturbation in Eq. (10) is underdetermined ($M < N$) and ill-posed.

When the target depth is available from ultrasound, we can set $\Delta\mu_a$ of a nontarget depth equal to zero. This implies that all the measured perturbations were originated from the particular depth that contained the target. Because the number of unknowns was reduced significantly, the reconstruction converged fast.

C. Total Least-Squares Solution

To solve the unknown optical properties of Eq. (10), several iterative algorithms have been used in the literature including the regularized least-squares method¹⁰ and the TLS method.^{20,21} The TLS performs better than the regularized least-squares method when the measurement data are subject to noise and the linear operator W contains errors. The operator errors can result from both the approximations used to derive the linear model and the numerical errors in the computation of the operator. We found that the TLS method provides more accurate reconstructed optical properties than the regularized least-squares method, so we adapted the TLS method to solve the inverse problems. It has been shown by Golub²² that the TLS minimization is equivalent to the following minimization problem:

$$\min \frac{\|U_{sd} - WX\|^2}{\|X\|^2 + 1}, \quad (11)$$

where X represents unknown optical properties. The conjugate gradient technique was employed to iteratively solve Eq. (11).

3. Methods

A. Probe Design and Imaging Geometry

There are two basic requirements to guide the design of the NIR probe. First, all source-detector separa-

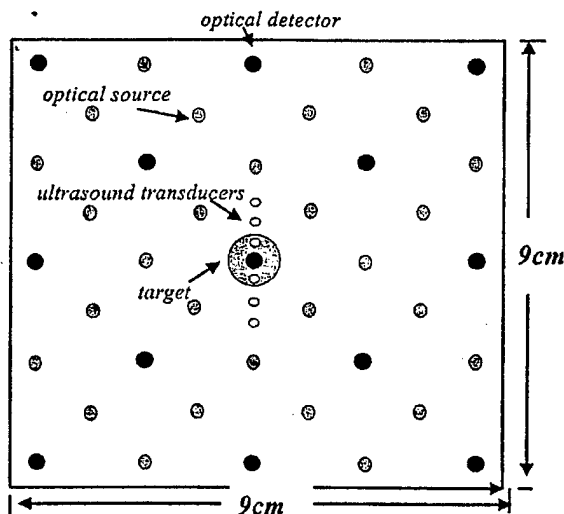


Fig. 2. Configuration of a dense array with 28 optical sources and 13 detectors as well as six ultrasound transducers. Large black circles are optical detectors, gray circles are optical sources, and small white circles are ultrasound transducers. A 1-cm-diameter spherical target was located at various depths in simulations and experiments.

tions have to be as large as 1 cm so that diffusion theory is a valid approximation for image reconstruction. Second, because the depth of a photon path is measured approximately one third to one half the source-detector separation, the distribution of source-detector distances should be from approximately 1 to 10 cm to effectively probe the depth from approximately 0.5 to 4 cm. On the basis of these requirements, we deployed a total of 28 sources and 13 detectors over a probe area of 9 cm \times 9 cm (see Fig. 2). The minimum source-detector separation in the configuration is 1.4 cm and the maximum is 10.0 cm. We call this array a filled or dense array (a term adapted from ultrasound array design). The 9 cm \times 9 cm \times 4 cm imaging volume was discretized into voxels of size 0.5 cm \times 0.5 cm \times 1 cm; therefore a total of four layers in depth was obtained. The target was a 1-cm-diameter sphere located at different locations. Because one of the objectives of this study was to evaluate the target depth distribution, the centers of the four layers in depth were adapted to the target depth. For example, if the target depth was $z = 3$ cm, the centers of the four layers were chosen as 1, 2, 3, and 4 cm, respectively.

The ultrasound transducers shown in Fig. 2 were deployed simultaneously on the same probe. The diameter of each ultrasound transducer is 1.5 mm and the spacing between the transducers is 4 mm, except the two located closer to the optical detector in the middle. The spacing between these two transducers is 8 mm. Because this study requires accurate target location as a reference to compare with the reconstructed absorption image location, six transducers are used to guide the spatial positioning of a target. The target is centered when the two

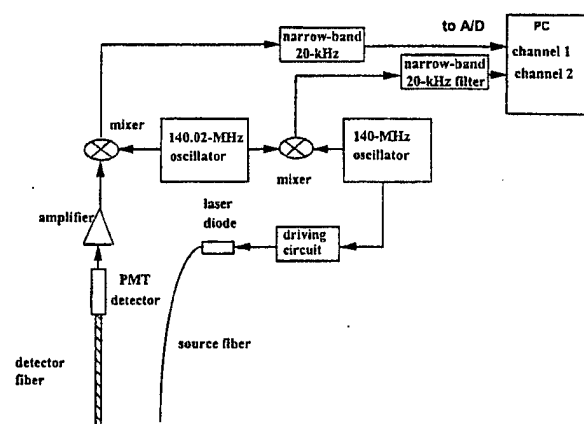


Fig. 3. Schematic of a single-channel optical data-acquisition system. A 140.02-MHz oscillator is used to drive the laser diode (780 nm) that delivers the light to the medium through the fiber. The detected signals are amplified and mixed with signals from a 140-MHz oscillator. The heterodyned 20-kHz signals are amplified, filtered, and digitized. The signals from two oscillators are also directly mixed to provide reference signals. The amplitude and phase of the waveform received through the medium are calculated from signals measured through the medium and the reference. PMT, photomultiplier tube.

middle ultrasound transducers receive the strongest signals. The target depth is determined from returned pulse-echo signals. In this study we do not intend to provide ultrasound images of the target with such a sparse ultrasound array, but we demonstrate the feasibility of using *a priori* depth information to improve optical reconstruction.

In regard to the image voxel size, there is a trade-off between the accurate estimation of the weight matrix W and the voxel size. Because W_{ij} is a discrete approximation of the integral

$$\int_v G(\mathbf{r}_v, \mathbf{r}_d, \omega) U_{\text{inc}}(\mathbf{r}_v, \mathbf{r}_s, \omega) (v/\bar{D}) d\mathbf{r}_v^3,$$

it is more accurate when the voxel size is smaller. However, the total number of reconstructed unknowns will increase dramatically with the decreasing voxel size. Because the rank of the matrix W is less than or equal to the total number of measurements [Eq. (10)], a further decrease in voxel size will not add more independent information to the weight matrix. We found that a 0.5 cm \times 0.5 cm \times 1 cm voxel size is a good compromise. Therefore we used this voxel size in image reconstructions reported in this paper.

B. Experimental System

We constructed a NIR frequency-domain system, and the block diagram of the system is shown in Fig. 3. On the source side, a 140.000-MHz sine-wave oscillator was used to modulate the output of a 780-nm diode laser that was housed in an optical coupler (OZ Optics Inc.). The output of the diode was coupled to the turbid medium through a single 200- μ m multimode

optic fiber. On the reception side, an optical fiber of 3 mm in diameter was used to couple the detected light to a photomultiplier tube detector. The output of the photomultiplier tube was amplified and then mixed with a local oscillator at a frequency of 140.020 MHz. The heterodyned signal at 20 kHz after the mixer was further amplified and filtered by a band-pass filter. The outputs of two oscillators (140.000- and 140.020-MHz signals) were directly mixed to produce 20-kHz reference signals. Both signals were sampled simultaneously by a dual-channel 1.25-MHz analog-to-digital converter (A/D) board. The Hilbert transform was performed on both sampled and reference waveforms. The amplitude of the Hilbert transform of the sampled waveform corresponds to the measured amplitude, and the phase difference between the phases of the Hilbert transforms of the sampled and reference waveforms corresponds to the measured phase.

A black probe with holes shown in Fig. 2 was used to emulate the semi-infinite boundary condition. Two 3-D positioners were moved independently to position the source and detector fibers at the desired spatial locations within the 9 cm \times 9 cm area.

A challenge in the reflection NIR probe design is to preserve a huge dynamic range in received signals. For example, the amplitude at a 1-cm source-detector separation measured from 0.6% Intralipid in reflection mode is approximately 84 dB larger than that at a 9-cm separation. So the signals can be saturated when they are measured from closer source-detector pairs, but they may be too low at more distant source-detector pairs. The problem can be overcome by means of controlling the light illumination. At least two illumination conditions need to be used: a low source level for closer source-detector pairs and a high level for distance source-detector pairs. In our system, a 30-dB attenuator connected to the 140-MHz oscillator was switched on and off to provide two different source levels and thus to preserve the dynamic range. Figure 4(a) shows a plot of the measured $\log [\rho^2 U_{sd}(\rho)]$ versus the source-detector separation ρ , and Fig. 4(b) shows the plot of the measured phase versus the source-detector separation. The Intralipid concentration was 0.6%, which corresponded to $\mu_s' = 6 \text{ cm}^{-1}$. Theoretically both $\log [\rho^2 U_{sd}(\rho)]$ and phase are linearly related to the source-detector separation because of the semi-infinite boundary condition used,³ and experimental measurements shown in Fig. 4 validate that they are linearly related to the source-detector separation.

The ultrasound system consists of six transducers (see Fig. 5), a pulser (Panametrics Inc.), an A/D converter, and a multiplexer. The pulser provided a high-voltage pulse of 6-MHz central frequency to drive each selected transducer. The returned signals were received by the same transducer, amplified by the receiving circuit inside the pulser, and sampled by the A/D converter with a 100-MHz sampling frequency.

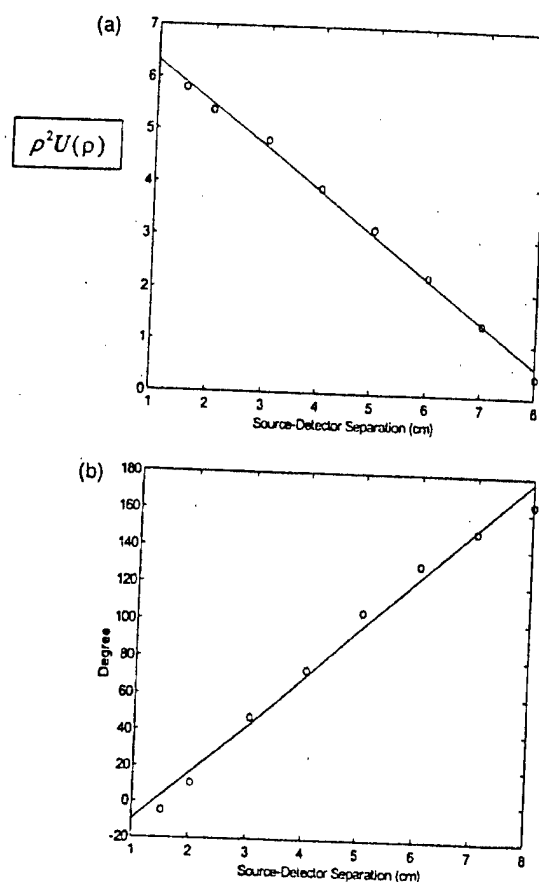


Fig. 4. Calibration curves. (a) $\log [\rho^2 U(\rho)]$ versus source-detector separation. (b) Phase versus source-detector separation.

C. Computation Procedures

1. Computation Procedures of Experimental Data

To study the relationship between the total number of source-detector pairs and distributions of reconstructed optical absorption coefficients, we started from the dense array with a total of 28 sources and 13 detectors (see Fig. 2) and gradually reduced this number to generate sparse arrays with 24×13 (24 sources and 13 detectors), 20×13 , 28×9 , 24×9 , 16×13 , 20×9 , 12×13 , 16×9 , 28×5 , 24×5 , 12×9 , 20×5 , 16×5 , and 12×5 source-detector pairs, respectively. Each sparse array was a subset of the

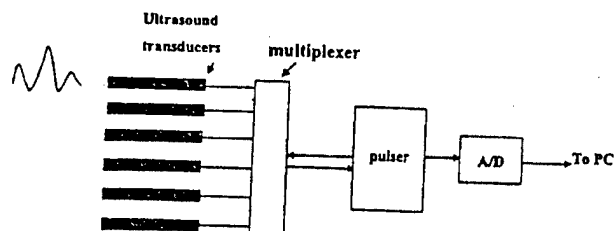


Fig. 5. Ultrasound data-acquisition system. The pulser is used to generate high-voltage pulses that are used to excite the selected ultrasound transducer. The returned signals are received by the selected transducer and are sampled by the A/D converter.

dense array, and its probe area was the same as the dense array. For each sparse array configuration, we compared the reconstructed optical imaging parameters measured from the dense array with those from the sparse arrays. The parameters include the maximum values of reconstructed $\hat{\mu}_a$ at different layers and their spatial locations, spatial resolution and artifact level of the $\hat{\mu}_a$ image, and target depth distribution. Targets of different absorption contrasts were located at different positions inside the Intralipid. For each target case, one set of measurements with the dense array was obtained, and subsets of the measurements were used as sparse array measurements. In all experiments, the background Intralipid concentration was approximately 0.6%, and μ_s' was experimentally determined from curve fitting results. Currently, we did not reconstruct target μ_s' , and we used the common μ_s' for both the background and the target.

The total number of iterations or stopping criterion was difficult to determine for experimental data. Ideally, the iteration should stop when the object function [see Eq. (11)] or the error performance surface reaches the noise floor. However, the system noise, particularly coherent noise, was difficult to estimate. In general, we found that the reconstructed values were closer to true values when the object function reached approximately 5–15% of the initial value (total energy in the measurements). However, this criterion was applicable only to reconstructions with total source–detector pairs closer to the dense array case. Therefore we used this criterion for the dense array reconstruction and used the same iteration number obtained from the dense array for the sparse arrays. Thus the iteration number is normalized to the dense array case.

2. Computation Procedures of Simulation

Simulations were performed to assist the understanding of the random noise on the reconstructed absorption coefficient. In simulations, Gaussian noise with different standard deviations proportional to the average value of each forward data set was added to the forward measurements. Typically, 0.5%, 1.5%, and 2.0% of the average value of each forward data set were used as standard deviations to generate noise. In simulations, the target μ_a was changed to different contrast values, and target μ_s' was kept the same as the background. The background μ_a and μ_s' were 0.02 and 6 cm⁻¹, respectively.

The stopping criterion used in the simulations was based on the noise level of the object function. Considering that the object function fluctuates within one standard deviation σ around the mean E when the iteration number is large, we can use $E + \sigma$ as a stopping criterion, i.e., the iteration will stop if the object function is less than $E + \sigma$. When the linear perturbation is assumed, E can be approximated as $\sum_j^n n(j)^2$ and σ as $\sum_j^n [2n(j)^4]^{1/2}$, where N is the total number of source–detector pairs and $n(j)$ is the generated random noise with a standard deviation pro-

portional to the specified percentage of the mean of the forward data set.

D. Testing Targets

Spherical testing targets of ~1 cm in diameter were made of acrylamide gel.¹⁶ The acrylamide powder was dissolved in distilled water, and 20% concentration of Intralipid was added to the acrylamide solution to dilute the solution to a 0.6% Intralipid concentration ($\mu_s' = 6$ cm⁻¹). India ink was added to the solution to produce target μ_a of different values. Acoustic scattering particles of 200 μ m in diameter were added to the solution before polymerization. Components of ammonium persulfate and tetramethylethylenediamine (known as TEMED) were added to the solution to produce polymerization.

4. Results of a High-Contrast Target Case

A. Experimental Results of a Dense Array

Figure 6(a) is an experimental image of a high-contrast target ($\mu_a = 0.25$ cm⁻¹) located in the Intralipid background ($\mu_s' = 6$ cm⁻¹). The target was a 1-cm-diameter sphere and its center was located at ($x = 0$, $y = 0$, $z = 3.0$ cm), where x and y were the spatial coordinates and z was the propagation depth. The target depth was well controlled by use of ultrasound pulse-echo signals, and the error was less than 1 mm. The 3-D images were reconstructed from the measurements made with the dense array, and the image shown was obtained at target layer 3. The centers of the imaging voxels in z are 1, 2, 3, and 4 cm for layers 1, 2, 3, and 4, respectively. The measured maximum value of the image lobe [$\hat{\mu}_{a(\max)}$] was 0.233 cm⁻¹, which was a close estimate of the target μ_a . The measured spatial location of $\hat{\mu}_{a(\max)}$ was ($x = 0.5$ cm, $y = 0.0$ cm), which agreed reasonably well with the true target location. The spatial resolution can be estimated from the -6-dB contour plot of Fig. 6(a), which is shown in Fig. 6(b). The outer contour is -6 dB from the $\hat{\mu}_{a(\max)}$, and the contour spacing is 1 dB. The width of the image lobe measured at the -6 dB-level corresponds to a full width at half-maximum (FWHM), which is commonly used to estimate resolution. The measured widths of longer and shorter axes were 1.01 and 1.60 cm, respectively, and the geometric mean was 1.27 cm, which was used to represent the -6-dB beam width. The contrast resolution can be estimated from the peak artifact level, and no artifact was observed in the image. The target depth can be assessed from the images obtained from other nontarget layers. Figure 6(c) is the image obtained at nontarget layer 4, and an image lobe of $\hat{\mu}_{a(\max)} = 0.138$ cm⁻¹ was observed. The spatial location of $\hat{\mu}_{a(\max)}$ was ($x = 0.0$, $y = 0.0$), which agreed well with the true target location. No distinct lobes were observed at nontarget layers 1 and 2, which indicates that the error in the target depth estimated from 3-D images was approximately 1 cm. Because the error in the true target depth was less

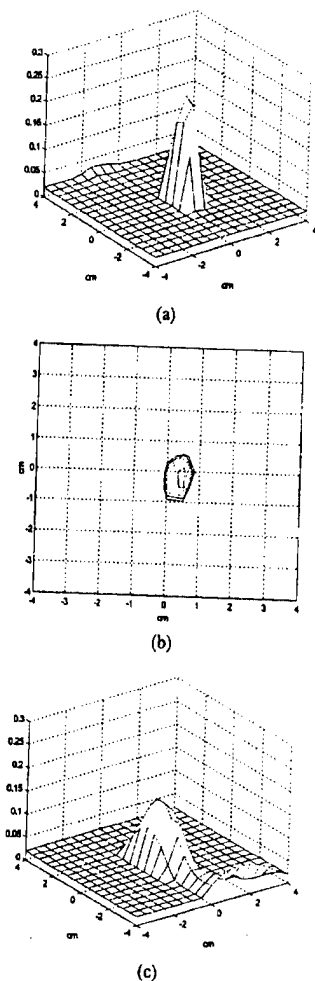


Fig. 6. Experimental 3-D images of μ_a reconstructed with a total of $28 \times 13 = 364$ source-detector pairs at 2437 iterations. The target ($\mu_a = 0.25 \text{ cm}^{-1}$) was located at $(x = 0, y = 0, z = 3.0 \text{ cm})$ inside the Intralipid background. (a) Reconstructed μ_a at target layer 3. The horizontal axes represent spatial x and y coordinates in centimeters, and the vertical axis is the μ_a . The measured maximum value of the image lobe [$\mu_{a(\text{max})}$] was 0.233 cm^{-1} , and its location was $(x = 0.5, y = 0.0)$. No image artifacts were observed. (b) -6-dB contour plot of (a). The outer contour is -6 dB from the $\mu_{a(\text{max})}$, and the contour spacing is 1 dB. The measured -6-dB beam width was 1.27 cm. (c) Reconstructed μ_a at nontarget layer 4. An image lobe of strength 0.138 cm^{-1} and spatial location of $(x = 0.0, y = 0.0)$ was observed.

than 1 mm, this 1-cm error was due largely to the depth uncertainty of diffusive waves.

B. Simulation Results of a Dense Array

Our simulations support the experimental results. Figure 7 shows simulation results obtained with the dense array. A simulated 1-cm-diameter absorber ($\mu_a = 0.25 \text{ cm}^{-1}$) was located at $(x = 0, y = 0, z = 3 \text{ cm})$ inside a homogeneous scattering background ($\mu_s' = 6 \text{ cm}^{-1}$). We added 0.5% Gaussian noise to the forward data generated from the analytic solution. Images obtained at nontarget layer 2, target layer 3, and nontarget layer 4 are shown in Fig. 7(a), Fig. (b), and 7(c), respectively. No target was found at layer

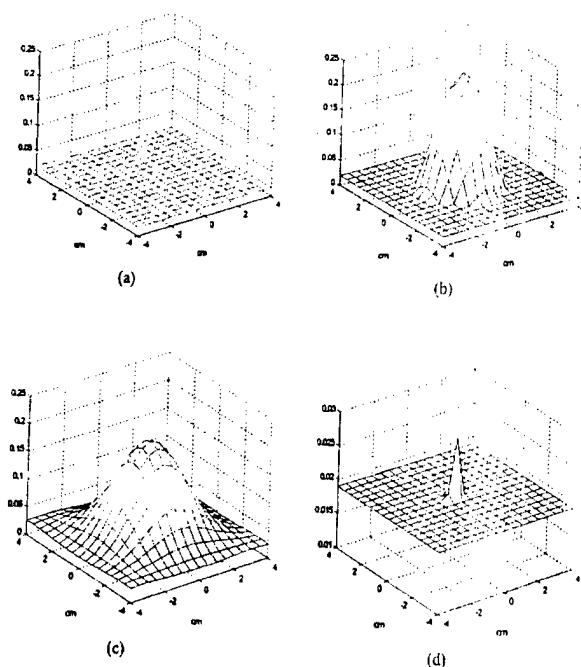


Fig. 7. Simulated 3-D images of μ_a reconstructed with a total of $28 \times 13 = 364$ source-detector pairs. The target ($\mu_a = 0.25 \text{ cm}^{-1}$) was located at $(x = 0, y = 0, z = 3.0 \text{ cm})$ inside the Intralipid background. (a) Reconstructed μ_a at nontarget layer 2 (simulation, 0.5% noise). No image lobe was observed. (b) Reconstructed μ_a at target layer 3 (simulation, 0.5% noise). The target of strength $\mu_{a(\text{max})} = 0.248 \text{ cm}^{-1}$ and the spatial location $(0.0, 0.0)$ was observed. (c) Reconstructed μ_a at nontarget layer 4 (simulation, 0.5% noise). The target of strength 0.190 cm^{-1} and location $(x = 0.0, y = 0.0)$ was observed. (d). Reconstructed μ_a at nontarget layer 2 with 1.0% noise. The target of 0.028 cm^{-1} was observed. Note that the scale of (d) is different from (a)-(c).

2, and the target of strengths 0.248 and 0.190 cm^{-1} appeared at layers 3 and 4, respectively. However, when the noise level in the forward data was increased to 1.0%, the target of strength $\mu_{a(\text{max})} = 0.028 \text{ cm}^{-1}$ appeared at nontarget layer 2 [Fig. 7(d)] as well as target layer 3 [$\mu_{a(\text{max})} = 0.163 \text{ cm}^{-1}$] and nontarget layer 4 [$\mu_{a(\text{max})} = 0.111 \text{ cm}^{-1}$]. This suggests that measurement noise is an important parameter to affect the target depth estimate.

C. Experimental Results of a Dense Array with Ultrasound Assistance

From ultrasound we obtained the target depth as well as the target boundary information. Figure 8(a) shows the received pulse-echo signals (from a depth of 2.3–3.5 cm) obtained from the six ultrasound transducers (see Fig. 2). The spatial dimension covered by the six transducers is 2.4 cm. The front surface of the target was indicated clearly by the returned pulses shown by two arrows, and the back surface was seen through the reflection of a soft plastic plate. The reflected signals of the back surface are also shown by arrows. The plate was used to hold the target and was transparent to light. The measured depth of the target front surface was 2.44 cm and the back surface was 3.43 cm. The distance

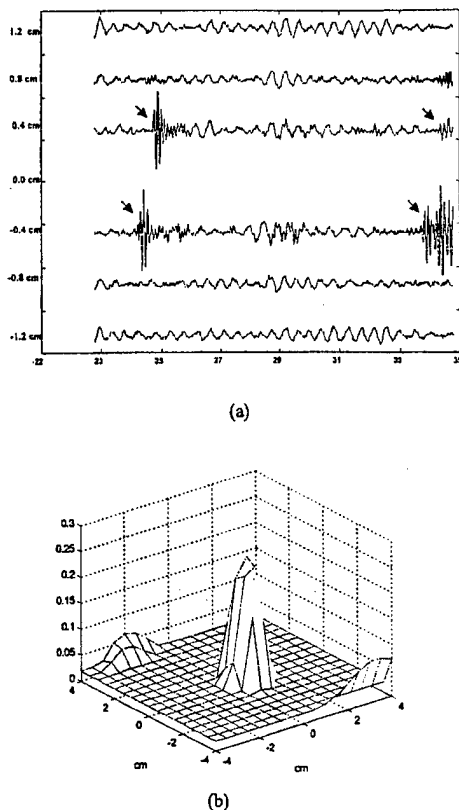


Fig. 8. (a) Ultrasound pulse-echo signals or A-scan lines obtained from six transducers. The abscissa is the propagation depth in millimeters. From reflected signals, the measured depth of the target front surface is 2.44 cm, and the back surface is 3.43 cm. The center of the target is ~ 3 cm. The total length of the signal corresponds to 1.2 cm in depth, and the measured distance between the front and the back surfaces is 0.993 cm. The spatial dimension covered by the transducers is 2.4 cm. (b) An image of the high-contrast target reconstructed at a target layer when we used only *a priori* target depth information provided by ultrasound. The reconstructed $\hat{\mu}_{a(\max)}$ reached 0.245 cm^{-1} at 216 iterations.

between the peaks of front reflection and backreflection was 0.993 cm, which corresponded to the target size. With the assistance of target depth, we reconstructed the absorption image at the target layer only. Figure 8(b) is the reconstructed $\hat{\mu}_a$ obtained from the dense array measurements. A total of 216 iterations were used to obtain $\hat{\mu}_{a(\max)} = 0.245 \text{ cm}^{-1}$, and the reconstruction was approximately ten times faster than that without the depth information. The spatial resolution was approximately the same as Fig. 6(a), and the -6 -dB beam width was 1.31 cm. The contrast resolution was 5 dB poorer because the measurement noise was lumped to single-layer reconstruction instead of being distributed to four layers.

D. Experimental Results of a Sparse Array

The imaging quality of sparse arrays decreased. Figure 9(a) is an experimental image at target layer 3 obtained from the 16×5 sparse array. The sparse array measurements used were a subset of the dense

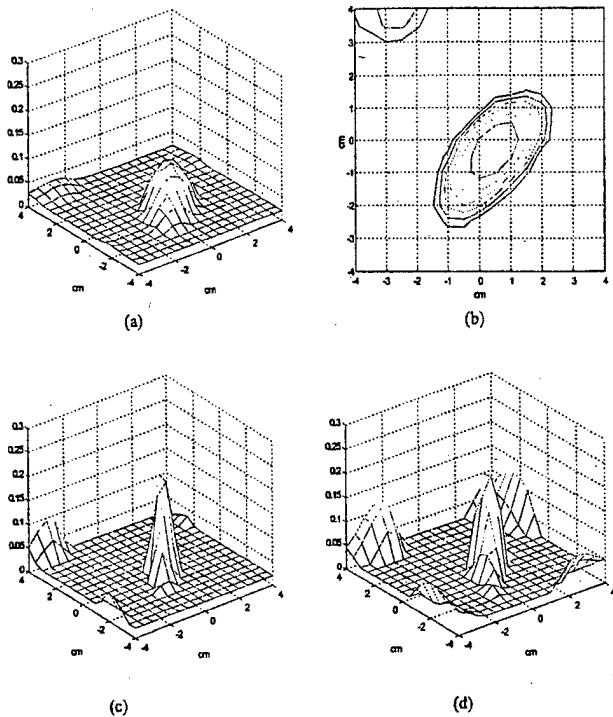


Fig. 9. Experimental images at target layer 3 reconstructed with a total of $16 \times 5 = 80$ source-detector pairs. (a) Reconstructed $\hat{\mu}_a$ at target layer 3 with 2478 iterations. The measured $\hat{\mu}_{a(\max)}$ was 0.107 cm^{-1} , which was 43% of the true value, and the spatial location of $\hat{\mu}_{a(\max)}$ was $(x = 0.5, y = -0.5)$. The measured peak image artifact level was -10 dB below the peak of the main image lobe. (b) -12 -dB contour plot of (a). The outer contour is -12 dB, and the contour spacing is 2 dB. The measured -6 -dB beam width was 2.55 cm, which was 200% broader than that of the dense array. (c) Reconstructed $\hat{\mu}_a$ at target layer 3 with 10,000 iterations. The measured $\hat{\mu}_{a(\max)}$ reached 0.264 cm^{-1} , and the peak artifact level was increased by 2 dB as well. (d) Reconstructed $\hat{\mu}_a$ at the target layer with only *a priori* target depth information provided by ultrasound. $\hat{\mu}_{a(\max)} = 0.173 \text{ cm}^{-1}$ at 216 iterations.

array measurements. The measured $\hat{\mu}_{a(\max)}$ was 0.107 cm^{-1} , which was 43% of the true value. The -6 -dB beam width was 2.55 cm, which was 200% broader than that of the dense array. Edge artifacts were observed and are best seen from Fig. 9(b), which is the -12 -dB contour plot of Fig. 9(a). The outer contour is -12 dB, and the spacing is 2 dB. The peak artifact level is -10 dB from the $\hat{\mu}_{a(\max)}$. The reconstructed $\hat{\mu}_a$ can be increased if the iteration is significantly increased. The iteration number used to obtain Fig. 9(a) was 2478, which was the same as that used to obtain Fig. 6. When the iteration number was increased to 10,000 for the sparse array case, the reconstructed $\hat{\mu}_{a(\max)}$ reached 0.264 cm^{-1} , which was close to the true target μ_a . However, the image artifact level was increased too [see Fig. 9(c)], and the ratio of the peak artifact to $\hat{\mu}_{a(\max)}$ was 2 dB higher than that shown in Fig. 9(a). In addition, the background noise fluctuation of nontarget layers 1 and 2 was increased. The noise fluctuation can be estimated from the standard deviations of reconstructed $\hat{\mu}_a$ at nontar-

get layers 1 and 2. At 2478 iterations, the averages and the standard deviations of $\hat{\mu}_a$ were 0.0233 (± 0.0028) and 0.0202 cm^{-1} ($\pm 0.0022 \text{ cm}^{-1}$) for nontarget layers 1 and 2, respectively, and these values were 0.0244 (± 0.0078) and 0.0208 cm^{-1} ($\pm 0.0073 \text{ cm}^{-1}$) at 10,000 iterations.

The measured maximum values of the image lobes or target strengths at the target layer and nontarget layer 4 continuously grew with each iteration, even though the reconstructed values at the target layer were close to the true value. This problem was mentioned in the literature,¹¹ but was not explained well. It is largely related to use of nonlinear constraints on $\Delta\mu_a$ in Eq. (10), particularly the choice of α . When α is close to 1, the reconstruction converges fast, and the target strength increases little after a certain number of iterations. When α is close to 0, the reconstruction converges slowly, and the target strength grows continuously. However, when the measurement signal-to-noise ratio (SNR) is not high, for example, in sparse array or low-contrast cases, the choice of $\alpha \approx 1$ can cause unstable reconstruction. In some cases, the reconstructed images can jump from one set of $\hat{\mu}_a$ to another, which causes the object function to increase suddenly and reduce again. This is related to the underdetermined nature of Eq. (10), i.e., the unknowns are far more than the measurements. In some cases the reconstructed images have multiple lobes of similar strengths, which indicate that the reconstruction does not converge at all. In all cases, the image background fluctuations were large compared with the fluctuations when a smaller α was used. We found that α between 0.1 and 0.4 can provide stable reconstruction, and we used $\alpha \approx 0.1$ for all experiments.

Another factor that accounts for the slow increase in the reconstructed value is use of linear perturbation to approximate the measurements that contain all higher-order perturbations. The minimization procedure [Eq. (11)] blindly minimizes the difference between the measurements and their linear approximation $W\Delta\mu_a$ and therefore reconstructs higher and higher $\Delta\mu_a$ if the iteration continues.

The target depth estimate was poorer than that of the dense array because of the lower SNR of the sparse array measurements. Similar to the dense array case, a target of strength $\hat{\mu}_{a(\max)} = 0.072 \text{ cm}^{-1}$ and location ($x = 0.5, y = 0.0$) was observed at nontarget layer 4. In addition, a target of strength $\hat{\mu}_{a(\max)} = 0.0348 \text{ cm}^{-1}$ and location ($x = 0.5, y = -0.5$) was observed at nontarget layer 2. However, the target mass, which was approximately the volume underneath the image lobe, was much smaller than that obtained at layers 3 and 4, and the target at layer 2 was buried in the background noise.

Figure 9(d) is the reconstructed $\hat{\mu}_a$ at the target layer from only the sparse array measurements. A total of 216 iteration steps were used to obtain $\hat{\mu}_{a(\max)} = 0.173 \text{ cm}^{-1}$, and the reconstruction was approximately 50 times faster than that without the depth information. The measured -6-dB beam width was 1.49 cm, which was approximately the

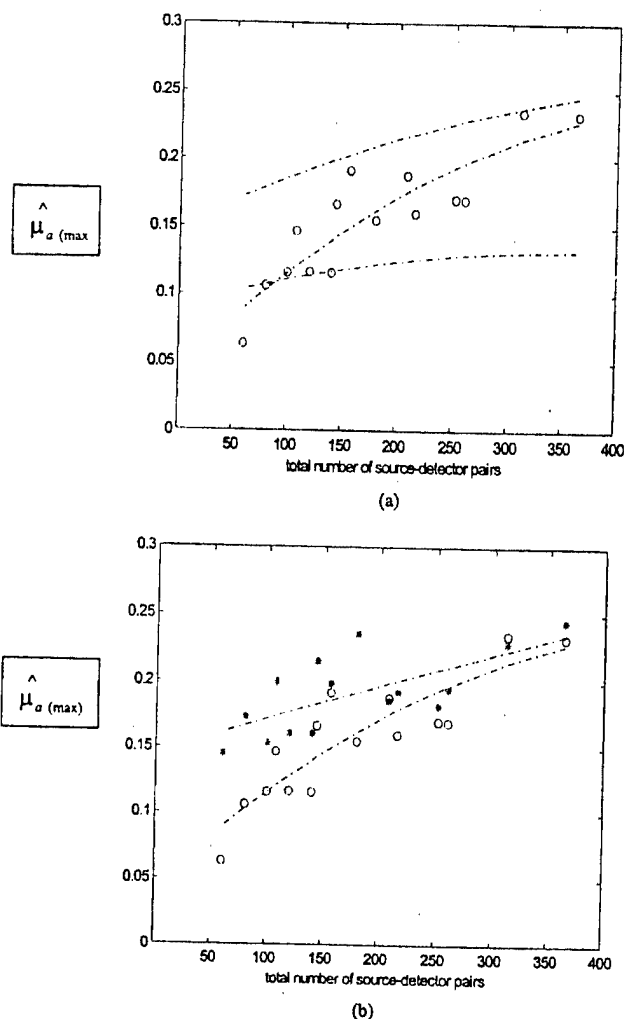


Fig. 10. $\hat{\mu}_{a(\max)}$ versus the total number of source-detector pairs. The center of the target ($\mu_a = 0.25 \text{ cm}^{-1}$) was located at ($x = 0.0, y = 0.0, z = 3.0 \text{ cm}$) in computer simulations and experiments. (a) Curves were obtained at the target layer. Two dashed curves (upper and lower) are the curve-fitting results of simulation data points obtained with 0.5% and 2.0% noise added to the forward data, respectively. The experimental data are plotted with circles, and the dashed curve in the middle is the fitting result of the experimental points. (b) The measured target strength (circles) and the curve-fitting result (lower curve). The measured target strength (stars) was reconstructed at the target layer only by use of *a priori* depth information and the curve fitting result (upper curve).

same as Fig. 9(c) but was improved 42% from Fig. 9(a). The contrast resolution was 2 dB worse for the same reason discussed above.

E. Simulation and Experimental Results of Reconstructed $\hat{\mu}_{a(\max)}$ versus Total Number of Source-Detector Pairs

To understand the effects of random noise on the performance of the reconstruction, we performed simulations for each array configuration. Gaussian noise of 0.5%, 1.0%, 1.5%, and 2.0% were added to each forward data set generated from the analytic solution [see Eq. (3)]. The center of a simulated 1-cm-diameter spherical target ($\mu_a = 0.25$

cm^{-1}) was located at $(x = 0, y = 0, z = 3.0 \text{ cm})$. Reconstructed images at different noise levels were obtained for each array configuration, and the peak values of image lobes $[\hat{\mu}_{a(\max)}]$ at target layer 3 were measured. Figure 10(a) shows simulation and experimental results of reconstructed $\hat{\mu}_{a(\max)}$ versus the total number of source-detector pairs. Two dashed curves are the fitting results of simulated data points with 0.5% (upper) and 2.0% (lower) noise. The dashed curve in the middle is the fitting result of experimental points plotted with circles. Second-order polynomials were used for all curve fittings. The reduction of the reconstructed $\hat{\mu}_{a(\max)}$ was significant when the noise level went up in the simulated data. Because the SNR of experimental data was decreased when the total number of source-detector pairs was reduced, the data were scattered around the 0.5% noise curve when the total pairs were large and were distributed around the 2.0% noise curve (values were 60% less than that obtained from the dense array) when the total pairs were reduced to less than 140. However, because our experimental system has both coherent and random noise, simulations based on random noise can only qualitatively explain the noise effect on the experimental data.

Figure 10(b) shows the experimental results of reconstructed $\hat{\mu}_{a(\max)}$ versus the total number of source-detector pairs obtained from 3-D imaging (circles) and ultrasound-assisted imaging (stars). The upper curve is the fitting result of the circles, and the lower curve is the result of the stars. In both cases, the reconstructed values were decreased when the total number of pairs was reduced. However, the reconstructed values were more accurate when the target depth information was available, and the improvement on average was 15%. The improvement was more dramatic when the total pairs were less.

For sparse arrays with total source-detector pairs less than 140, the reconstructed $\hat{\mu}_{a(\max)}$ could be increased if the iterations were significantly increased. However, the image artifact level of the target layer and the noise level of the nontarget layers were increased too. With the assistance of simulations, we offer the following explanations to the increased image artifact and noise level problem. In simulations, the iteration was stopped when the TLS error between the measurement and the linear approximation reached the noise floor, which was

$$E + \sigma = \sum_j^N n(j)^2 + \sum_j^N [2n(j)^4]^{1/2},$$

where $n(j)$ was the generated random noise with the standard deviation proportional to a certain percent of the mean of the forward data set for each array

configuration. When the object function reached the noise floor, the gradient

$$\nabla g = \frac{-2(U_{sd} - W\Delta\mu_a)^T(W)}{\Delta\mu_a^T \Delta\mu_a + 1} - \frac{-2(U_{sc} - W\Delta\mu_a)^T(U_{sd} - W\Delta\mu_a)(\Delta\mu_a)}{(\Delta\mu_a^T \Delta\mu_a + 1)^2}$$

can be approximated as

$$\nabla g \approx \frac{-2(N)^T(W)}{\Delta\mu_a^T \Delta\mu_a + 1} - \frac{-2(N)^T(N)(\Delta\mu_a)}{(\Delta\mu_a^T \Delta\mu_a + 1)^2},$$

where N is the noise vector. Therefore the search procedure of Eq. (11) is more random and noisy. Because $\Delta\mu_{a(\text{new})} = \Delta\mu_{a(\text{old})} + \beta \nabla g$, the $\Delta\mu_a$ updating is more random and noisy. β is proportional to the square of the gradient. Continuous iteration when the object function has reached the noise floor may destroy the convergence of the reconstruction. We found that when the SNR of the data is high, for example, high-contrast cases, continuous iteration in general increases reconstructed μ_a and sidelobes. However, when the SNR of the data is low, for example, low-contrast cases, continuous iteration does not increase the reconstructed μ_a , but destroys the convergence of the reconstruction [see Fig. 12(c) below].

F. Experimental Results of Imaging Parameters Versus Total Number of Source-Detector Pairs

The imaging parameters measured from different array configurations are listed in Table 1. Listed first are the measured parameters at target layer 3. These parameters are a -6-dB beam width of the image lobe, the peak sidelobe level, $\hat{\mu}_{a(\max)}$, and the distance in the x - y plane between the location of $\hat{\mu}_{a(\max)}$ and the true target location. Next are the same parameters measured at nontarget layer 4. The increase in beam width was negligible for the arrays with more than 140 source-detector pairs and was 100% broader for the sparse arrays with total pairs less than this number. The sidelobe level was progressively increased when the total pairs were reduced. At nontarget layer 4, when the total pairs were reduced to less than 140, the measured image lobes were broad and no sidelobes were seen. The agreement between the measured $\hat{\mu}_{a(\max)}$ location and the true target location is good for all the array configurations, which suggests that this parameter is not sensitive to the total number of source-detector pairs in high-contrast cases. Table 1 next lists the strength of the target measured at nontarget layer 2 and its spatial location. Because the SNR of the sparse array measurement was lower, the target appeared at layer 2 when total pairs were less than 180. However, in all cases, the target mass measured at this layer was much smaller than that obtained at the target layer and nontarget layer 4. Finally, Table 1 lists the measured imaging parameters when the target depth was available to optical reconstruction. Compared with parameters obtained from optical im-

Table 1. Imaging Parameters Measured with Different Array Configurations: High-Contrast Target Case ($\mu_s = 0.25 \text{ cm}^{-1}$)

Parameter	Total Pairs															
	28 × 13	24 × 13	20 × 13	28 × 9	24 × 9	16 × 13	20 × 9	12 × 13	16 × 9	28 × 5	24 × 5	12 × 9	20 × 5	16 × 5	12 × 5	
Target layer 3 (2437 iterations)																
-6-dB beam width (cm)	1.27	1.42	1.65	1.67	1.70	1.44	1.78	1.39	1.55	2.45	2.34	1.69	2.50	2.55	3.09	
Peak sidelobe (dB)	-18	-13	-12	-14	-13	-16	-12	-13	-11	-12	-11	-10	-11	-10	-8	
$\hat{\mu}_{\alpha(max)}$ (cm ⁻¹)	0.23	0.23	0.17	0.17	0.16	0.18	0.16	0.19	0.17	0.12	0.12	0.15	0.12	0.11	0.06	
$ \hat{\mu}_{\alpha(max)} - (0,0) $ (cm)	0.5	0.7	0.7	0.5	0.5	0.7	0.5	0.7	0.7	0.5	0.5	0.7	0.5	0.7	0.7	
Nontarget layer 4 (2437 iterations)																
-6-dB beam width (cm)	2.10	2.11	2.48	2.40	2.52	2.26	2.59	2.40	2.54	4.35	4.10	2.63	3.93	4.51	5.36	
Peak sidelobe (dB)	-8	-9	-17	-14	-13	-19	-12	-13	-12							
$\hat{\mu}_{\alpha(max)}$ (cm ⁻¹)	0.14	0.14	0.12	0.11	0.11	0.14	0.11	0.14	0.13	0.06	0.07	0.12	0.06	0.07	0.07	
$ \hat{\mu}_{\alpha(max)} - (0,0) $ (cm)	0.0	0.5	0.0	0.7	0.7	0.5	0.7	0.0	0.7	0.5	0.5	0.7	0.5	0.5	0.5	
Nontarget layer 2 (2437 iterations)																
$\hat{\mu}_{\alpha(max)}$ (cm ⁻¹)	0.00	0.00	0.00	0.00	0.00	0.00	0.043	0.024	0.047	0.026	0.043	0.048	0.032	0.035	0.038	
$ \hat{\mu}_{\alpha(max)} - (0,0) $ (cm)							1.12	0.70	1.12	0.70	1.00	1.12	0.70	0.70	0.5	
Target layer only (216 iterations)																
-6-dB beam width (cm)	1.31	1.40	1.68	1.61	1.55	1.57	1.50	1.41	1.20	1.71	1.48	1.45	1.77	1.49	1.75	
Peak sidelobe (dB)	-12	-12	-12	-9	-8	-12	-7	-9	-7	-8	-8	-6	-8	-8	-8	
$\hat{\mu}_{\alpha(max)}$ (cm ⁻¹)	0.25	0.23	0.19	0.18	0.19	0.19	0.24	0.20	0.22	0.16	0.16	0.20	0.15	0.17	0.15	
$ \hat{\mu}_{\alpha(max)} - (0,0) $ (cm)	0.5	0.5	0.5	0.5	0.5	0.5	0.5	0.5	0.5	0.5	0.5	0.5	0.5	0.5	0.5	

Note: Italicized entries are 100% broader than the dense array beam width.

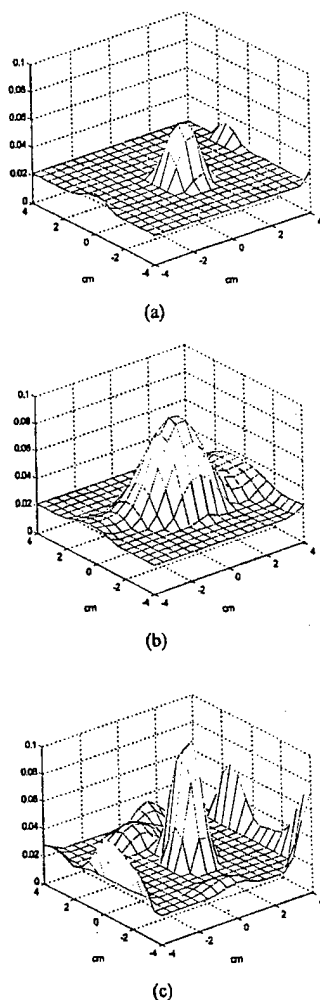


Fig. 11. Experimental images of μ_a reconstructed from a total of $28 \times 13 = 364$ source-detector pairs. The target ($\mu_a = 0.10 \text{ cm}^{-1}$) was located at $(x = 0, y = 0, z = 2.5 \text{ cm})$ inside the Intralipid background. (a) Reconstructed μ_a at target layer 3. The measured $\hat{\mu}_{a(\max)}$ was 0.063 cm^{-1} at 510 iterations, and its location was $(x = 0.0, y = -0.5)$. Edge artifacts were observed and the peak level was -7 dB from the $\hat{\mu}_{a(\max)}$. (b) Reconstructed μ_a at non-target layer 4. The measured $\hat{\mu}_{a(\max)}$ was 0.0871 cm^{-1} at 510 iterations, and its location was $(x = 0, y = 0)$. (c) Reconstructed μ_a at the target layer when only the target depth information provided by ultrasound was used. $\hat{\mu}_{a(\max)} = 0.107 \text{ cm}^{-1}$ at 56 iterations.

aging only, the -6-dB beam width was improved by 24% on average, and the reconstruction speed was approximately 10 times faster; however, the sidelobe was 3 dB worse.

5. Results of a Lower-Contrast Target Case

A. Experimental Results of a Dense Array

To study the effects of target contrast on the quality of the reconstructed image for each array configuration, we conducted a set of experiments with a lower-contrast target ($\mu_a = 0.10 \text{ cm}^{-1}$) embedded in the Intralipid. The center of the target was located at $(x = 0, y = 0, z = 2.5 \text{ cm})$. The centers of the imaging voxels in z were 0.5, 1.5, 2.5, and 3.5 cm for

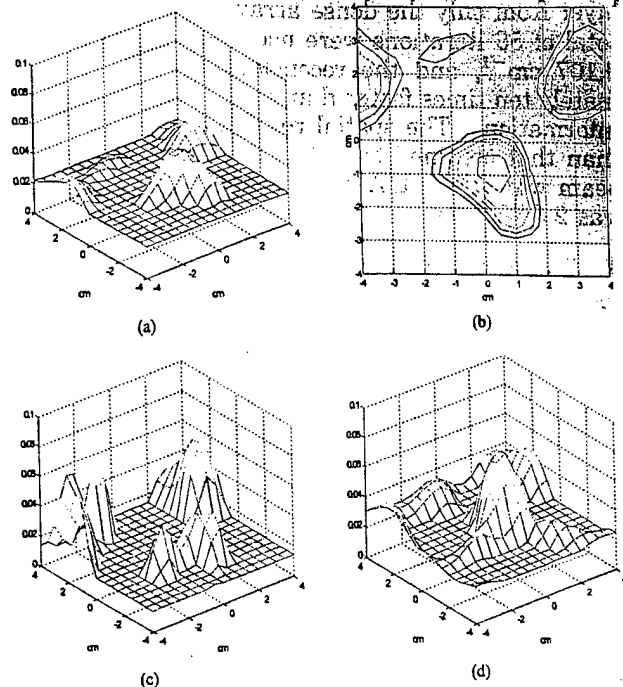


Fig. 12. Experimental images of μ_a at target layer 3 reconstructed from a total of $24 \times 5 = 120$ source-detector pairs. (a) Reconstructed μ_a at target layer 3 with 510 iterations. The measured $\hat{\mu}_{a(\max)}$ was 0.049 cm^{-1} , which was 49% of the true target μ_a , and its location was $(x = 0.5, y = -1.0)$, which was displaced from the true target location by 1.11 cm. Image artifacts were observed, and the peak was -3 dB from the $\hat{\mu}_{a(\max)}$. (b) -6-dB contour plot of (a). (c) Reconstructed μ_a at target layer 3 with 1500 iterations. The peak artifact was 5 dB higher than the image lobe. (d) Reconstructed μ_a at target layer 3 (56 iterations) with only *a priori* target depth information provided by ultrasound. The measured $\hat{\mu}_{a(\max)}$ was 0.074 cm^{-1} , and its location was $(x = 0.5, y = -0.5)$. Image artifacts were observed, and the peak was -5 dB from the $\hat{\mu}_{a(\max)}$.

layers 1, 2, 3, and 4, respectively. Figure 11 shows the images of the lower-contrast target obtained at target layer 3 [Fig. 11(a)] and deeper nontarget layer 4 [Fig. 11(b)]. The images were reconstructed from the measurements made with the dense array. At target layer 3, the measured $\hat{\mu}_{a(\max)}$ was 0.063 cm^{-1} , which was approximately 63% of the target μ_a . The measured spatial location of $\hat{\mu}_{a(\max)}$ was $(x = 0.0, y = -0.5)$, which agreed reasonably well with the true target location. The measured -6-dB beam width was 1.83 cm, which was 144% times broader than the beam width of the high-contrast case. Edge artifacts were observed, and the peak level was -7 dB from the $\hat{\mu}_{a(\max)}$. At nontarget layer 4, the measured $\hat{\mu}_{a(\max)}$ was 0.0871 cm^{-1} , which was even higher than that measured at the target layer. Because the SNR of the data was lower than the high-contrast case, the target depth estimate was poorer. A target of $\hat{\mu}_{a(\max)} = 0.0543 \text{ cm}^{-1}$ located at $(x = 0, y = -0.5)$ was observed at nontarget layer 2, and its mass was much smaller than that obtained at the target layer and nontarget layer 4.

Figure 11(c) is the reconstructed μ_a at the target

layer from only the dense array measurements. A total of 56 iterations were used to obtain $\hat{\mu}_{a(\max)} = 0.107 \text{ cm}^{-1}$, and the reconstruction was approximately ten times faster than that without the depth information. The spatial resolution was 8% better than that obtained from Fig. 11(a), and the -6-dB beam width was 1.67 cm. The contrast resolution was 2 dB worse.

B. Experimental Results of a Sparse Array

The imaging quality of sparse arrays decreased. Figure 12(a) is an image of the same target ($\mu_a = 0.10 \text{ cm}^{-1}$) reconstructed from measurements made with the 24×5 sparse array. The measured $\hat{\mu}_{a(\max)}$ was 0.049 cm^{-1} , which was 49% of the true value. The -6-dB contour plot is shown in Fig. 12(b). The measured spatial location of $\hat{\mu}_{a(\max)}$ was ($x = 0.5, y = -1.0$), which was displaced from the true target location by 1.11 cm in radius. The measured -6-dB beam width was 2.98 cm, which was 163% broader than that measured from the dense array. Sidelobes were abundant, and the peak value was -3 dB below the peak of the image lobe. These sidelobes would produce false targets in the image if no *a priori* information about the target locations were given.

In this case, continuous iteration did not increase the target strength but increased the sidelobe strength. Figure 12(a) was obtained at 510 iterations, whereas Fig. 12(c) was obtained at 1500 iterations. After approximately three times more iterations, the peak of the artifact was 5 dB higher than the peak of the image lobe. The target depth estimated from 3-D images was worse at 1500 iterations than that at the 510 iterations. The measured target strengths at nontarget layer 2 were 0.064 and 0.1661 cm^{-1} at 510 and 1500 iterations, respectively, and the strengths at nontarget layer 4 were 0.0597 and 0.1087 cm^{-1} , respectively. In addition, the background noise fluctuation or standard deviation measured at nontarget layer 1 was increased with the iterations. The mean and the standard deviation at 510 iterations were 0.024 and 0.0041 cm^{-1} , whereas these values at 1500 iterations were 0.0267 and 0.0104 cm^{-1} .

As shown in Fig. 12(d), the reconstructed image improved a lot when the target depth was given. The maximum strength was 0.074 cm^{-1} , and its location was $(0.5, -0.5)$. The -6-dB beam width was 2.63 cm, which was 12% better than that obtained from Fig. 12(a). The sidelobe was -6 dB from the peak, which was improved by 3 dB compared with Fig. 12(a).

C. Experimental Results of Reconstructed $\hat{\mu}_{a(\max)}$ versus Total Number of Source-Detector Pairs

With the iteration number normalized to the dense array case, we measured target strengths at target layer 3 and nontarget layer 4 for all sparse array configurations. Figure 13 shows the experimental data points (circles) of measured $\hat{\mu}_{a(\max)}$ versus the total number of source-detector pairs obtained at target layer 3 [Fig. 13(a)] and nontarget layer 4 [Fig.

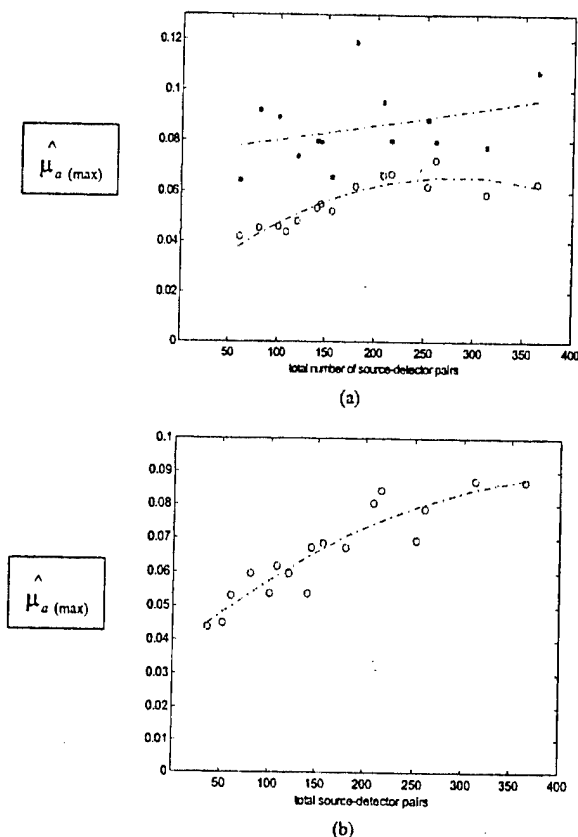


Fig. 13. Low-contrast target case. (a) Reconstructed $\hat{\mu}_{a(\max)}$ versus total source-detector pairs with the target depth available (stars) and the curve-fitting results (upper curve). Reconstructed $\hat{\mu}_{a(\max)}$ versus total source-detector pairs measured at target layer (circles) and the curve-fitting results (lower curve) and (b) at deeper nontarget layer 4.

13(b)]. The two curves were the fitting results of experimental points when we used second-order polynomials. In both layers, the $\hat{\mu}_{a(\max)}$ values were decreased when the total number of source-detector pairs was reduced. The reconstructed target strengths were reduced to less than 60% when the total pairs were less than 156 and 140 for target layer 3 and nontarget layer 4, respectively. The ultrasound-assisted reconstruction results are shown in Fig. 13(a) (stars), and the average reconstructed $\hat{\mu}_{a(\max)}$ for all array configurations was 0.085 cm^{-1} . Compared with the average of 0.055 cm^{-1} obtained from optical imaging only at the target layer, a 30% improvement was achieved.

D. Experimental Results of Imaging Parameters versus Total Number of Source-Detector Pairs

The measured imaging parameters obtained from different array configurations are listed in Table 2. Similar to Table 1, listed are the measured parameters at target layer 3 and nontarget layer 4. The increase in beam width at the target layer was negligible for the arrays with more than 156 source-detector pairs and was more than 50% for the sparse arrays with total pairs less than this number. The sidelobes were progressively worse when the total

Table 2. Imaging Parameters Measured with Different Array Configurations: Lower-Contrast Target Case ($\mu_s = 0.10 \text{ cm}^{-1}$)

Parameter	Total Pairs															
	28 × 13	24 × 13	20 × 13	28 × 9	24 × 9	16 × 13	20 × 9	12 × 13	16 × 9	28 × 5	24 × 5	20 × 5	16 × 5	12 × 5	8 × 5	
Target layer 3 (510 iterations)																
-6-dB beam width (cm)	1.83	1.98	2.02	2.24	1.86	2.09	2.42	2.73	3.07	3.07	2.98	3.57	4.23	3.07		
Peak sidelobe (dB)	-6	-6	-7	-4	-3	-5	-2	-6	-3	-4	-3	-3	-2	-2		
$\hat{\mu}_{s(\max)}$ (cm ⁻¹)	0.06	0.06	0.07	0.06	0.07	0.07	0.06	0.05	0.06	0.05	0.05	0.05	0.05	0.04		
$ \hat{\mu}_{s(\max)} - (0,0) $ (cm)	0.5	0.5	0.7	1.0	0.7	0.7	0.7	0.7	0.7	1.11	1.11	1.0	1.0	1.58		
Nontarget layer 4 (510 iterations)																
-6-dB beam width (cm)	3.36	3.42	3.31	4.81	3.08	3.28	4.69	4.20	5.49	5.57	5.15	6.62	8.49	8.81		
Peak sidelobe (dB)	-8	-9	-8	-6	-7	-7	-5	-5	-5	-5	-5	-5	-5	-5		
$\hat{\mu}_{s(\max)}$ (cm ⁻¹)	0.09	0.09	0.08	0.07	0.08	0.08	0.07	0.07	0.07	0.05	0.06	0.05	0.06	0.05		
$ \hat{\mu}_{s(\max)} - (0,0) $ (cm)	0.0	0.0	0.5	0.7	0.5	0.5	0.5	0.5	0.5	0.5	0.5	0.5	0.5	0.5		
Nontarget layer 2 (510 iterations)																
$\hat{\mu}_{s(\max)}$ (cm ⁻¹)	0.062	0.058	0.054	0.048	0.051	0.049	0.047	0.046	0.047	0.054	0.064	0.060	0.064	0.049		
$ \hat{\mu}_{s(\max)} - (0,0) $ (cm)	0.70	0.70	0.70	0.5	0.70	1.12	0.5	1.12	0.0	0.70	0.0	0.50	0.0	0.70		
Target layer only (56 iterations)																
-6-dB beam width (cm)	1.67	2.43	2.35	1.72	2.10	1.93	1.56	3.12	2.37	2.12	2.63	1.84	1.86	3.30		
Peak sidelobe (dB)	-4	-5	-6	-3	-3	-6	-2	-6	-4	-4	-5	-4	-3	-2		
$\hat{\mu}_{s(\max)}$ (cm ⁻¹)	0.11	0.08	0.08	0.09	0.08	0.10	0.12	0.07	0.08	0.08	0.07	0.09	0.06	0.06		
$ \hat{\mu}_{s(\max)} - (0,0) $ (cm)	0.7	0.0	0.0	0.5	0.0	0.7	0.0	0.7	0.0	0.7	0.7	1.11	0.7	0.5		

Note: Italicized entries are 50% broader than the above entries.

Note: Italicized entries are 50% broader than the dense array beam width.

pairs were reduced. At the target layer, the distance between the $\hat{\mu}_{a(\max)}$ location and the true target location was more than 1 cm for the arrays with total pairs less than 140. Table 2 then lists the measured peak image lobe at nontarget layer 2 and its location. The target appeared at nontarget layer 2 in all array configurations because of the lower SNR of the data. However, the target mass observed at this layer was much smaller than that at layers 3 and 4 in all cases. The last row in Table 2 shows the measured imaging parameters when the target depth was available to optical reconstruction. Compared with parameters obtained from optical imaging only, the -6-dB beam width was improved by 41% on average, and the reconstruction speed was approximately ten times faster; however, the sidelobe was 1 dB worse.

6. Discussion

In addition to the total number of source-detector pairs, the measured imaging parameters are also related to other system parameters, for example, modulation frequency and system noise. The 140-MHz modulation frequency chosen in this study is a typical frequency used by many research groups. Our system noise level, including both coherent and incoherent, is less than 10 mV peak to peak, which is sufficiently low. Therefore the results we obtained are pertinent to 3-D imaging using similar system parameters and reflection geometry.

In this study the target absorption coefficient was reconstructed from measurements. Similar studies can be done for the scattering coefficient as well. To reconstruct the scattering coefficient, we can use the scattering weight matrix derived by O'Leary¹¹ to relate the medium scattering variations with the measurements. Simultaneous reconstruction of both absorption and scattering coefficients in reflection geometry is also possible, provided that the absorption and scattering weight matrices are regulated carefully. Because the eigenvalues of the two matrices are significantly different, good regulation schemes are needed to balance the reconstructed absorption and scattering coefficients at each iteration. This subject is one of our topics for further study.

In this study the ultrasound-assisted optical reconstruction was demonstrated at a particular target layer. Similar studies can be done with multiple targets located at different layers. In the multiple target case, we can attribute measured perturbations to more layers instead of a single layer. However, the improvements in reconstructed optical properties and reconstruction speed may be less than that of the single-layer case.

Ultrasound has good imaging capability, and it can detect small lesions of a few millimeters in size. However, its specificity in cancer detection is not high as a result of overlapping characteristics of benign and malignant lesions. NIR imaging has high specificity in cancer detection; however, it suffers low resolution and lesion location uncertainty because of the diffused nature of the NIR light. The hybrid imaging that combines ultrasound imaging capability and

NIR contrast has a great potential to overcome deficiencies of either method. As we reported in the paper, the target depth information can significantly improve the accuracy of the reconstructed optical absorption coefficient and reconstruction speed. In addition to use of *a priori* target depth information, the target spatial distribution provided by ultrasound can be used in optical reconstruction as well.¹⁵ With the localized spatial and temporal target information, the accuracy of the reconstructed optical properties and the reconstruction speed can be improved further. To demonstrate this, we need an ultrasound imaging transducer located at the middle portion of the probe. We are currently pursuing this study.^{23,24}

In this study the targets of different contrasts were located at the center position. We have also done studies with targets of different contrasts located at off-center positions. For an off-center target case, the effective number of source-detector pairs is less than that of the on-center target case because measurements from certain source-detector pairs do not contain much information about the target. For example, if a target is placed at $(x = 2, y = 2, z = 3.0 \text{ cm})$, the measurements of source-detector pairs at the opposite corner of the probe contribute little to the image reconstruction. In one study, targets of high and low contrast were located at $(x = 2, y = 2, z = 3.0 \text{ cm})$. The reconstructed maximum absorption coefficient at the target layer was related more to the total neighbor source-detector pairs. However, the maximum value at a deeper nontarget layer was related more to the total source-detector pairs and was decreased with the reduction of total pairs. Because the photons originated from distant sources and detected by distant detectors experience longer and more diffused scattering paths, they are likely to interact with the off-center target and contribute to the absorption estimate at the deeper layer. In the same study, the measured sidelobe levels were 4.5 and 2.0 dB poorer on average compared with the on-center high- and low-target cases, respectively. The beam widths were comparable to those measured from on-center cases.

7. Summary

The relationship between the total number of source-detector pairs and the imaging parameters of a reconstructed absorption coefficient was evaluated experimentally. A frequency-domain system of a 140-MHz modulation frequency was used in the experiments. Reconstruction at a selected target depth with *a priori* depth information provided by ultrasound was demonstrated. The results have shown that the reconstructed absorption coefficient and the spatial resolution of the absorption image were decreased when the total number of source-detector pairs was reduced. More than 160 source-detector pairs were needed to reconstruct the absorption coefficient within 60% of the true value and spatial resolution comparable to that obtained with the dense array. The contrast resolution was

poorer in general because of edge artifacts and could be worse if significant larger iteration numbers are used for reconstruction. The error in target depth estimated from 3-D optical images was approximately 1 cm. With the *a priori* target depth information provided by ultrasound, the reconstruction can be done at a selected depth. Because the unknowns were reduced significantly, the reconstruction speed was approximately ten times faster than that without depth information. In addition, the accuracy of the reconstructed absorption coefficient was improved by 15% and 30% on average for high- and low-contrast cases, respectively. Furthermore, the measured -6-dB beam width was improved by 24% and 41% for high- and low-contrast cases, respectively. The sidelobe was 3 and 1 dB poorer for high- and low-contrast cases because the measurement noise was lumped to single-layer reconstruction instead of multiple layers.

In conclusion, ultrasound-assisted 3-D optical imaging has shown promising results to overcome the problems associated with the reconstruction by use of diffusive waves. With the target depth information provided by ultrasound, the reconstructed absorption coefficient was more accurate and the reconstruction speed was much faster.

We acknowledge the funding support of the Connecticut Innovation Program, the U.S. Department of Defense Army Breast Cancer Program (DAMD17-00-1-0217), the Windy Will Cancer Fund, Multi-dimensional Technology Inc., and the Research Foundation of the University of Connecticut.

References

1. S. Fantini, S. Walker, M. Franceschini, M. Kaschke, P. Schlag, and K. Moesta, "Assessment of the size, position, and optical properties of breast tumors *in vivo* by noninvasive optical methods," *Appl. Opt.* **37**, 1982-1989 (1998).
2. S. Zhou, Y. Chen, Q. Nioka, X. Li, L. Pfaff, C. M. Cowan, and B. Chance, "Portable dual-wavelength amplitude cancellation image system for the determination of human breast tumor," in *Optical Tomography and Spectroscopy of Tissue III*, B. Chance, R. Alfano, and B. Tromberg, eds., *Proc. SPIE* **3597**, 571-579 (1999).
3. R. M. Danen, Y. Wang, X. D. Li, W. S. Thayer, and A. G. Yodh, "Regional imager for low resolution functional imaging of the brain with diffusing near-infrared light," *Photochem. Photobiol.* **67**, 33-40 (1998).
4. T. McBride, B. W. Pogue, E. Gerety, S. Poplack, U. Osterberg, B. Pogue, and K. Paulsen, "Spectroscopic diffuse optical tomography for the quantitative assessment of hemoglobin concentration and oxygen saturation in breast tissue," *Appl. Opt.* **38**, 5480-5490 (1999).
5. M. A. Franceschini, K. T. Moesta, S. Fantini, G. Gaida, E. Gratton, H. Jess, M. Seeber, P. M. Schlag, and M. Kaschke, "Frequency-domain techniques enhance optical mammography: initial clinical results," *Proc. Natl. Acad. Sci. USA* **94**, 6468-6473 (1997).
6. J. B. Fishkin, O. Coquoz, E. R. Anderson, M. Brenner, and B. J. Tromberg, "Frequency-domain photon migration measurements of normal and malignant tissue optical properties in human subject," *Appl. Opt.* **36**, 10-20 (1997).
7. T. L. Troy, D. L. Page, and E. M. Sevick-Muraca, "Optical properties of normal and diseased breast tissues: prognosis for optical mammography," *J. Biomed. Opt.* **1**(3), 342-355 (1996).
8. R. J. Grable, D. P. Rohler, and S. Kla, "Optical tomography breast imaging," in *Optical Tomography and Spectroscopy of Tissue: Theory, Instrumentation, Model, and Human Studies II*, B. Chance and R. Alfano, eds., *Proc. SPIE* **2979**, 197-210 (1997).
9. H. Jiang, K. Paulsen, U. Osterberg, B. Pogue, and M. Patterson, "Optical image reconstruction using frequency-domain data: simulations and experiments," *J. Opt. Soc. Am. A* **12**, 253-266 (1995).
10. W. Zhu, Y. Wang, Y. Deng, Y. Yao, and R. Barbour, "A wavelet-based multiresolution regularized least squares reconstruction approach for optical tomography," *IEEE Trans. Med. Imaging* **16**(2), 210-217 (1997).
11. M. A. O'Leary, "Imaging with diffuse photon density waves," Ph.D. dissertation (University of Pennsylvania, Philadelphia, Pa., 1996).
12. X. Li, T. Durduran, A. Yodh, B. Chance, and D. N. Pattanayak, "Diffraction tomography for biomedical imaging with diffuse-photon density waves," *Opt. Lett.* **22**, 573-575 (1997).
13. C. Matson and H. Liu, "Analysis of the forward problem with diffuse photon density waves in turbid media by use of a diffraction tomography model," *J. Opt. Soc. Am. A* **16**, 455-466 (1999).
14. C. Matson and H. Liu, "Backpropagation in turbid media," *J. Opt. Soc. Am. A* **16**, 1254-1265 (1999).
15. Q. Zhu, T. Durnana, M. Holboke, V. Ntziachristos, and A. Yodh, "Imager that combines near-infrared diffusive light and ultrasound," *Opt. Lett.* **24**, 1050-1052 (1999).
16. Q. Zhu, D. Sullivan, B. Chance, and T. Dambro, "Combined ultrasound and near infrared diffusive light imaging," *IEEE Trans. Ultrason. Ferroelectr. Freq. Control* **46**, 665-678 (1999).
17. Q. Zhu, E. Conant, and B. Chance, "Optical imaging as an adjunct to sonograph in differentiating benign from malignant breast lesions," *J. Biomed. Opt.* **5**(2), 229-236 (2000).
18. M. Jholboke, B. J. Tromberg, X. Li, N. Shah, J. Fishkin, D. Kidney, J. Butler, B. Chance, and A. G. Yodh, "Three-dimensional diffuse optical mammography with ultrasound localization in human subject," *J. Biomed. Opt.* **5**(2), 237-247 (2000).
19. D. A. Boas, M. A. O'Leary, B. Chance, and A. G. Arjun, "Scattering of diffuse photon density waves by spherical inhomogeneities within turbid media: analytic solution and applications," *Proc. Natl. Acad. Sci. USA* **91**, 4887-4891 (1994).
20. W. Zhu, Y. Wang, and J. Zhang, "Total least-squares reconstruction with wavelets for optical tomography," *J. Opt. Soc. Am. A* **15**, 2639-2650 (1998).
21. P. C. Li, W. Flax, E. S. Ebbini, and M. O'Donnell, "Blocked element compensation in phased array imaging," *IEEE Trans. Ultrason. Ferroelectr. Freq. Control* **40**, 283-292 (1993).
22. G. H. Golub, "Some modified matrix eigenvalue problems," *SIAM (Soc. Ind. Appl. Math.) Rev.* **15**, 318-334 (1973).
23. D. Piao, X.-H. Ding, P. Guo, and Q. Zhu, "Optimal distribution of near infrared sensors for simultaneous ultrasound and NIR imaging," in *Biomedical Topical Meetings, Postconference Digest*, Vol. 38 of OSA Trends in Optics and Photonics Series (Optical Society of America, Washington, D.C., 2000), pp. 472-474.
24. P. Guo, Q. Zhu, D. Piao, and J. Fikiet, "Combined ultrasound and NIR imager," in *Biomedical Topical Meetings, Postconference Digest*, Vol. 38 of OSA Trends in Optics and Photonics Series (Optical Society of America, Washington, D.C., 2000), pp. 97-99.